MODELING OF TECTONIC PROCESSES ASSOCIATED WITH EARTHQUAKES

Thesis by

Pierre Henri Jungels

In Partial Fulfillment of the Requirements
for the Degree of
Doctor of Philosophy

California Institute of Technology
Pasadena, California

1973

(Submitted January 12, 1973)

ACKNOWLEDGMENTS

The results presented in Chapters I and II of this thesis will also appear as Jungels and Frazier (1972), and it should be mentioned that a great part of the remainder of this work should appear with the same dual authorship.

I benefited greatly from my relationship with Dr. G. Frazier from both his constant enthusiasm and his deep understanding of the physics of materials. Dr. C. Archambeau supervised our work from the onset and his interest in the preliminary results contributed greatly to their improvements. His critical review of this thesis is deeply appreciated.

The professors and students from the Seismological Laboratory provided an environment in which ideas could be constantly tested and improved. My colleagues R. Alewine, T. Hanks and J. Whitcomb and Professors D. Anderson, C. Allen and H. Dix particularly helped me during some portions of this work. Their contributions are gratefully acknowledged.

I am grateful to Mrs. Sally Henyey for typing this thesis and to Mr. Laszlo Lenches for drafting its figures, both in record times.

This work was supported by U. S. Geological Survey Contract No. 14-08-0001-12714. While at Caltech, the author was a Fulbright scholar.

ABSTRACT

A finite element variational method is described and applied to the analysis of zero frequency seismic data. This technique presents a suitable tool for the analysis of permanent displacements, tilts and strains caused by seismic events, since it can model variable fault offsets in heterogeneous media.

The accuracy of the technique is demonstrated by detailed static field computations for vertical and dipping dislocations acting in plane strain, corresponding to an infinite-length fault in a homogeneous half space, by comparison with closed form analytic solutions. A parametric study of material inhomogeneities and variable fault offsets reveals that order of magnitude changes in the solutions can occur for both near and far field displacements and strains.

The technique was applied to the San Fernando earthquake using a two-dimensional (plane strain) model. The best solution was obtained by separating the fault into two distinct parts, both having offsets near the surface a factor of five larger than the average slip. Both stress drop and displacements vary by more than an order of magnitude along the fault plane, the maximum occurring at 1 km depth. Several solutions are investigated for the hypocentral region, one of them giving as much as 5 m offset.

The Alaskan earthquake of 1964 is also studied in plane strain, and the observed vertical movements are inverted numerically to yield a "best fit" offset on the fault surface. This solution gives good results for the observed horizontal movement. It is characterized by large variations of the slip with a maximum of 33 m below Montague Island.

Then, a relationship is derived, giving energy released as a function of prestress, fault area, change in the local gravitational potential energy and fault offset, neglecting nonlinear behavior outside the fault zone. The finite element method is shown to allow direct calculation of the terms of the resulting equation from static consideration of failure in a prestress medium.

This is applied to the last solution for the San Fernando earthquake, the best fit offset of the Alaska earthquake and a simple model of the Montana earthquake, 1959. In all three cases, the results indicate that a spatially variable prestress field gives the best representation of the tectonic processes involved. The force of gravity is found to be a significant factor in the energy balance of each event, increasing the estimate of prestress for the thrust faults and the apparent stress drop for the Montana normal fault.

For the San Fernando earthquake, the prestress field in the hypocentral region is shown to exceed critical stress levels corresponding to granite strength as measured in the laboratory, while the average stress drop for the entire fault is below 200 bars. This is a possible answer to the apparent discrepancy between laboratory and average field measurements.

The Wilmington oil field subsidence is modeled by using a finite element code which solves numerically Biot's consolidation theory. The best fit is obtained for a very small interaction constant. The models result in significant stress concentrations which could have triggered

the small magnitude events known as the Long Beach subsidence earthquakes.

TABLE OF CONTENTS

Page

I. TWO-DIMENSIONAL FINITE ELEMENT METHOD APPLIED TO DISLOCATION

II. TWO-DIMENSIONAL MODELS OF THE 1971 SAN FERNANDO AND 1964 ALASKA EARTHQUAKES

III. THEORY OF ENERGY RELEASED IN SHALLOW EARTHQUAKES AND ITS NUMERICAL APPLICATION

IV. CALCULATION OF PRESTRESS, STRESS DROP AND ENERGY RELEASED FOR THREE EARTHQUAKES

V. TECTONIC EFFECTS OF FLUID-ROCK INTERACTION

INTRODUCTION

In the past decade, the fracture and flow of rocks has been given renewed attention by geologists and geophysicists, with a strong emphasis on more quantitative observations. Studies of tectonic processes associated with the earthquake phenomenon have progressed through research advances in three major interconnected fields: theoretical source mechanism investigations, seismological observations and analysis covering the entire frequency spectrum and laboratory measurements of fracture and flow of rocks.

Because of computational restrictions with respect to closed form solutions, theoretical geophysics often deals with highly idealized models. As a result, even though it provides exact solutions of the problem treated, it does not represent the physical situation completely. For instance, the "dislocation" theory (Steketee, 1958; Maryama, 1964) because of the assumptions of isotropy and homogeneity results in a problem description which averages the field variable over large areas of the "fault". By the same token, although it provides us with an increased understanding of broad features of failure in situ, observational seismology deals only with average source parameters. This is due to the fact that the seismic radiation which carries information about the failure characteristics is usually analyzed in terms of either point source theory or dynamic dislocation theory. In both cases, the source parameters determined from spectral analysis represent only values averaged over the source region. It must be pointed out, however, that when near field observation is available, the averaging can be refined to cover portions of the fault area, for instance, the hypocentral region (Hanks, 1972).

In any event, this thesis will show that the apparent agreement between source parameters determined from static dislocation theory and from body wave spectra (e.g., Hanks and Wyss, 1972) is not very meaningful in terms of failure mechanism. Indeed, we will show that in the case of the San Fernando earthquake, the strength of the rock in the hypocentral region is in the range of that measured in laboratory experiments. This is in sharp contrast with the value of the average strength of the crust most widely quoted in the literature (Chinnery, 1964).

This study, then, is a contribution to the understanding of tectonic processes relevant to earthquakes, where the source parameters (prestress, stress drop, fault offset, etc.) are considered with their variations over the fault surface. This is done by using the finite element numerical technique. Described extensively in the engineering literature (e.g., Przemienicki, 1968; Zienkiewicz, 1971) and increasingly used by geophysicists, this technique is ideally suited for solving tectonophysics problems. The main advantage of this particular tool is that it permits the solution of elaticity problems characterized by nonlinearities, anisotropy, heterogeneities and arbitrary external or internal boundaries.

Chapter I of this thesis describes a special purpose finite element scheme, especially suited to modeling "dislocations" in a heterogeneous geological environment. The results compare favorably to the closed form solution of static dislocation theory for an infinite half space. Thus, simple perturbations of the half space, such as lateral inhomogeneities or variations of fault offset with fault width can be analyzed in terms of their influence on free surface observations.

Chapter II applies this technique to the inversion of free surface permanent displacement caused by the San Fernando and the Alaskan earthquakes. The results indicate that for both events the "best fit" to the data is obtained for a slip vector that varies extensively over the fault plane.

Chapter III shows how the concept of stress relaxation (Archambeau, 1968) can be utilized to obtain a formulation linking the static change of strain energy inside a small volume around the earthquake fault to the seismic energy which "leaks" out of that volume. It is then shown how the finite element models can directly compute all the static terms involved in that formulation.

Chapter IV applies this concept to the two earthquakes treated in Chapter II. While using the fault offsets computed previously, we introduce various amounts of prestress in the models and show how this can lead to a self-consistent failure mechanism. The results indicate that large variations of prestress and stress changes are necessary to explain the observations. The Montana earthquake of 1959 is treated in a simple model designed to show a situation where the surface observations indicate a predominance of subsidence.

Chapter V deals with a special type of earthquake failure where the prestress field responsible for the events is caused by man's activity. The subsidence of the Wilmington oil field is analyzed in the framework of Biot's consolidation theory and modeled by a dynamic axisymmetric finite element code. The results indicate that fluid withdrawal from an underground reservoir can generate large non-hydrostatic stresses. These stresses are sufficient to explain by themselves the Long Beach "subsidence" earthquakes.

I. TWO-DIMENSIONAL FINITE ELEMENT METHOD APPLIED TO "DISLOCATION" MODELS

Introduction

Following the occurrence of an earthquake, it is always difficult to ascertain the circumstances, processes, and consequences of the rupture. It is frequently even difficult to estimate the extent of the rupture and the amount of relative offset at various points along the break. Since most, if not all, of the fault break takes place at depth, we must have the capability to deduce fault behavior from surface observations if we are to gain a clear understanding of what takes place in a given earthquake event. In this chapter we are concerned with the capability of analyzing permanent deformations, i.e., zero frequency data, such as changes in geodetic controls and permanent changes in strain and tilt.

Faults typically occur in complex geologic formations, since they either mark the boundary between two moving plates or a weak zone in a regional block. Conventional analytic treatments, developed using Green's function techniques, have very limited flexibility for representing variations in conditions along the length of the fault and variations in structural layering in the near field. Certain numerical techniques can be employed to overcome these restrictions. We chose to apply what we think is probably the best suited numerical technique for modeling an earthquake: the finite element method. This method is conveniently formulated for processing by a digital computer, and it appears that analyses based on the finite element method need be limited only by the accuracy of the problem description.

The finite element method appeared in the engineering literature during the mid-fifties (Argyris, 1954; Turner et al., 1956), although its concepts are found earlier in mathematical physics (Courant, 1943). It has now become a very important analysis tool for engineers. However, the method is just beginning to have its impact in geophysical applications where irregular geometry, heterogeneities, and nonlinearities are commonplace. Because of the limited usage of the finite element method in the geophysical literature, we present a brief, but general, development of the "displacement method" for treating elastic solids. We also describe how a discontinuity in the displacement field is treated using the finite element method. The accuracy of the numerical scheme for simulating faulted material is demonstrated by comparing computed results with solutions based on dislocation theory for an infinitely long fault acting in plane strain in a homogeneous half space. The relative displacement offset is then prescribed point by point along the fault plane to examine the influence of variations in slip on the surface displacements. Simple structural boundaries are also treated to examine how heterogeneities influence the surface behavior.

Finite Element Method

The finite element method is a technique for representing a continuum by a discrete system. As is done with finite difference methods, a boundary value problem is reduced to a large number of simultaneous equations, which are processed by a high speed digital computer. The solution to these equations provides an estimate of the continuum behavior, the accuracy of which is only limited by the number of equations that are used to simulate the continuum. Time-dependent phenomena simply lead to the repeated application of the set of simultaneous equations.

Although this approach to continuum processes can be quite tedious in that hundreds or even thousands of simultaneous equations are often needed for suitable accuracy, the method is an extremely powerful analytical tool in that essentially all aspects of the governing physics can be simulated: irregular geometry, heterogeneous and anisotropic material properties, nonlinear constitutive properties, and even complex rupture processes.

The method is, however, limited in some respects. For example, spatial variations that are very small compared to the regional extent that is being modeled are difficult to simulate accurately. This limitation restricts the direct application of the finite element method for analyzing details of a stress concentration. Also, in treating propagating stress waves, the numerical method is best suited for treating low frequency waves with ten or more elements per wave length.

The finite element method approach can be utilized by means of three different approximate methods: (1) the displacement method, (2) the force method, and (3) the mixed method. In the displacement method an approximate representation is used for the displacement field, and total potential energy is minimized in order to put the displacement field in equilibrium, in an approximate sense. In the force method an approximate representation is used for the stress field and complementary energy is minimized in order to make the resulting strain field integrable (satisfy compatibility equations), in an approximate sense. Various mixed methods are used that result in some degree of approximation to both the equilibrium equations and the compatibility equations. Only the displacement method is developed here.

The displacement field $u_i(\underset{\sim}{x}, t)$ is represented as a linear combination of normalized spline functions (interpolation functions)

$$\begin{aligned} u_i(\underset{\sim}{x}, t) &= \sum_n U_{in}(t)\, \Phi_n(\underset{\sim}{x}) \\ &= \left[\Phi(\underset{\sim}{x})\right] \left\{U_i(t)\right\} \end{aligned} \tag{1.1}$$

where the symbols $[\;]$ and $\{\;\}$ denote a row matrix and a column matrix, respectively. The n^{th} spline function $\Phi_n(\underset{\sim}{x})$ is zero everywhere except for the region within the aggregate of elements joining at node n (see Fig. 1). At node n the spline function is normalized to unity

$$\Phi_n(x_n) = 1.0 \tag{1.2}$$

so that the generalized coordinates $\{U_i(t)\}$ become nodal displacements

$$U_{in}(t) = U_i(x_n, t) \tag{1.3}$$

For general nonconservative systems, the displacement field expressed by Eq. (1.1) is required, at each instant in time, to satisfy the expression for zero rate of virtual work

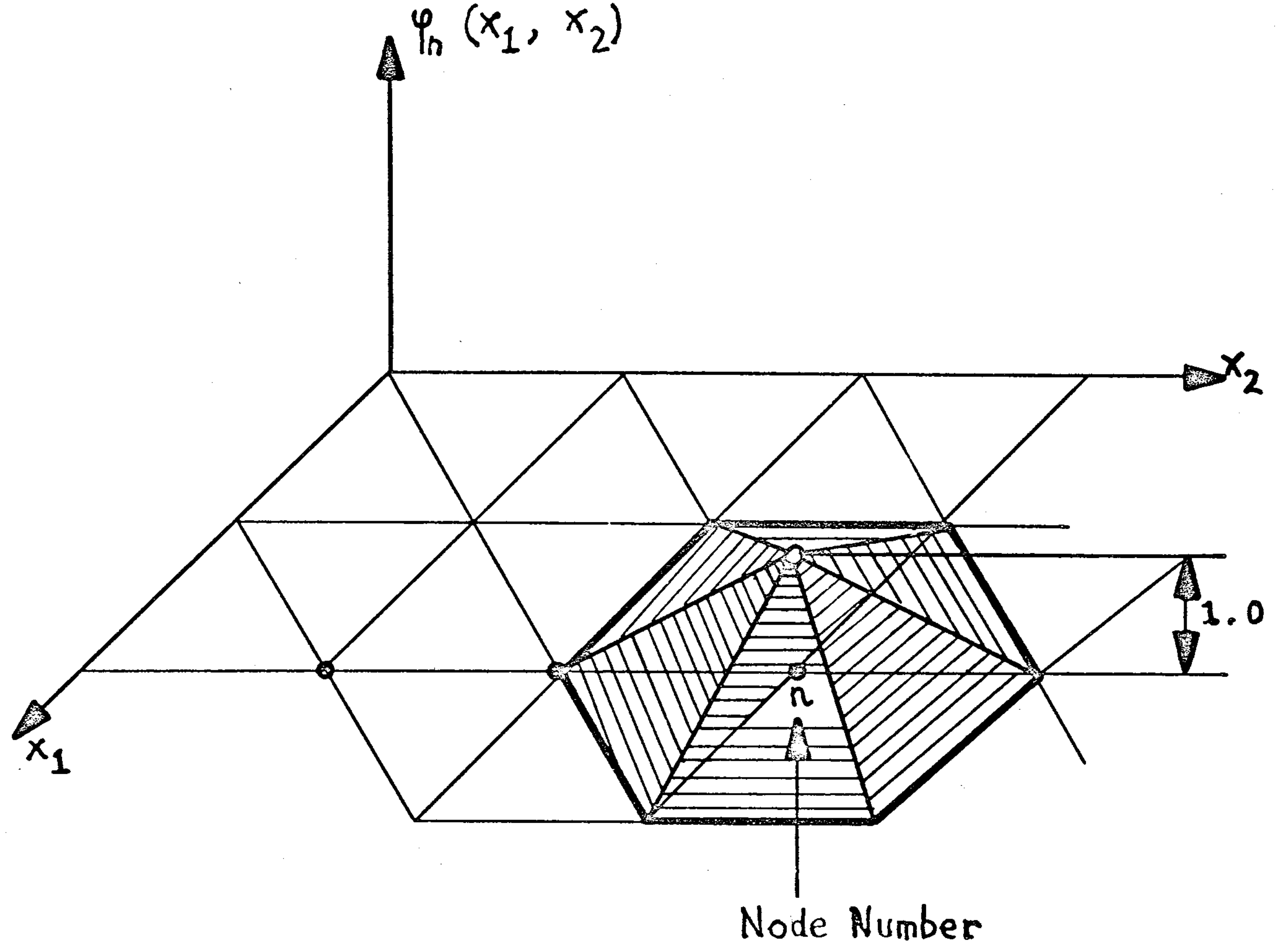

Figure 1. Piecewise linear representation of displacement in a 2-D space $U_i(x_1, x_2, t) = \Sigma_n U_{in}(t)\, \Phi_n(x_1, x_2)$.

$$\int_V (\rho \frac{dv_i}{dt} \delta v_i + \sigma_{ij} \frac{\partial}{\partial x_j} \delta v_i - \overline{f}_i \delta v_i) \, dV - \int_{S\sigma} \overline{\tau}_i \, \delta v_i \, dS = 0$$

in which

u_i is the particle displacement

v_i is the particle velocity

δv_i is the virtual particle velocity (continuous in V and zero on S_u)

$\frac{dv_i}{dt} = \frac{\partial v_i}{\partial t} + v_j \frac{\partial v_i}{\partial x_j}$ is the particle acceleration

σ_{ij} is the symmetric stress tensor which is related to strain through constitutive laws

$\overline{\tau}_i = n_j \sigma_{ij}$ is the traction specified along S_σ

ρ is the mass density

$\overline{f}_i$ is the body force

V is the region enclosed by $S_u + S_\sigma$

S_u is that portion of the boundary on which the time history of displacement, $u_i(t)$, is specified

S_σ is that portion of the boundary on which the time history of surface traction, $\overline{\tau}_i(t)$, is specified.

If we restrict ourselves to linear elasticity, the virtual work expression

$$\int_V \left(\rho \ddot{u}_i \, \delta u_i + E_{ijkl} \frac{\partial u_i}{\partial x_l} \frac{\partial}{\partial x_k} \delta u_i - \overline{f}_i \, \delta u_i \right) dV$$
$$- \int_{S_\sigma} \overline{\tau}_i \, \delta u_i \, dS = 0 \qquad (1.4)$$

is used to govern the approximate solution where $\ddot{u}_i = \partial^2 u_i / \partial^2 t$. In this expression stress and strain have been related by the generalized Hooke's law

$$\sigma_{ik} = E_{ikjl}\,\epsilon_{jl}$$
$$= E_{ikjl}\,\frac{\partial u_j}{\partial x_l}$$

since $E_{ikjl} = E_{iklj}$ (1.5)

The virtual displacement field δu_i is expressed in terms of virtual displacements of the node points by Eq. (1.1)

$$\delta u_i \cong \frac{\partial u_i}{\partial U_{jn}}\,\delta U_{jn} = \Phi_n\,\delta U_{in} = [\Phi\,(\underset{\sim}{x})\,]\,\{\delta U_i(t)\} \qquad (1.6)$$

Similarly, the spline function approximation to the displacement field, Eq. (1.1), is substituted for each term involving displacement in the virtual work expression and the column vectors of nodal displacements are factored out of the various integral operators to yield

$$\left\{\delta U_i(t)\right\}^T\left([M]\,\{\ddot{U}_i(t)\} + [K_{ij}]\,\{U_j(t)\} - \{\overline{P}_i(t)\}\right) = 0 \qquad (1.7)$$

where
$$[M] = \int_V [\Phi\,(\underset{\sim}{x})\,]^T\,\rho\,[\Phi\,(\underset{\sim}{x})]\,dV$$
$$[K_{ij}] = \int_V [\frac{\partial\Phi}{\partial x_k}\,(\underset{\sim}{x})\,]^T\,E_{ikjl}\,[\frac{\partial\Phi}{\partial x_l}\,(\underset{\sim}{x})\,]\,dV \qquad (1.8)$$
$$\overline{P}_i(t) = \int_V [\Phi(\underset{\sim}{x})\,]^T\,\overline{f}_i\,dV + \int_{S_\sigma} [\Phi\,(\underset{\sim}{x})\,]^T\,\overline{\tau}_i\,dS$$

Since the virtual displacements can be taken one node at a time, the discretized version of the virtual work expression becomes a time-dependent set of simultaneous equations

$$\left[M\right]\left\{\ddot{U}_i(t)\right\} + \left[K_{ij}\right]\left\{U_j(t)\right\} = \left\{\overline{P}_i(t)\right\} \qquad (1.9)$$

Because of the nature of the spline functions, the various integrals are carried out element by element. In fact, for the more common element types (triangle and quadrilateral in 2-D, tetrahedron and hexahedron in 3-D), the $\left[M\right]$ and $\left[K_{ij}\right]$ integrals have been evaluated for a typical element geometry assuming ρ and E_{ikjl} constant, see, for example, Zienkiewicz (1967) or Przemienieki (1968)). These element integrals provide the basis for finite element computer codes that serve to assemble the element properties and process the resulting set of simultaneous equations. Use of the derived properties of isolated elements endows the finite element codes with great versatility in the treatment of irregular geometric shapes with mixed boundary conditions and with inhomogeneous material properties.

The development carried out above is mathematically similar to, and follows along the lines of, the ordinary Rayleigh-Ritz procedure. Actually the finite element displacement method was originally developed from physical arguments. In this latter approach, approximate nodal force-displacement relationships are developed for a typical element using an energy criterion. These isolated elements are then assembled by equating the displacements common to each node. The resulting set of simultaneous equations expressed above is then obtained by setting the sum of all of the forces acting at each node point equal to the product of nodal acceleration times the mass associated with the node point. The resulting "stiffness" terms $\left[K_{ij}\right]$ are identical with the corresponding terms derived above; however, slight differences can arise in the "mass" terms $\left[M\right]$ and the "load" terms $\left\{\overline{P}_i(t)\right\}$ because of the manner in which distributed loads and inertial forces are concentrated at the node points.

We will describe how the finite element method can be used to simulate a dislocation in a continuum. We consider an isolated fault surface Σ across which the displacement field is discontinuous, i.e.

$$U_i^{(+)}(\underset{\sim}{x}, t) - U_i^{(-)}(\underset{\sim}{x}, t) = \Delta U_i(\underset{\sim}{x}, t)$$

$$\text{for } \underset{\sim}{x} \longrightarrow \Sigma \tag{1.10}$$

where the superscripted (+) and (-) denote limiting values of the displacement as x approaches Σ from opposite sides of the fault surface. The region occupied by the elements adjacent to Σ on the (+) side is denoted $V^{(+)}$, while the region occupied by those adjacent elements on the (-) side of Σ are denoted $V^{(-)}$. The node points along Σ are bifurcated so that

$$\left\{U_{in}^{(+)}(t)\right\} - \left\{U_{in}^{(-)}(t)\right\} = \left\{ \Delta U_{in}(t)\right\}$$

for $\underset{\sim}{x}_n$ on Σ , or, in general, we write

$$\left\{U_i^{(+)}(t)\right\} - \left\{ U_i^{(-)}(t)\right\} = \left\{ \Delta U_i(t)\right\} \tag{1.11}$$

where $\Delta U_{in}(t) = 0$ for $\underset{\sim}{x}_n$ not on Σ .

For the case where $\left\{ \Delta U_i(t) \right\}$ is specified, the virtual displacements in Eq. (1.4) simply become

$$\left\{\delta U_i(\underset{\sim}{x}, t)\right\} = \left[\Phi(\underset{\sim}{x})\right] \left\{ U_i^{(+)}(t)\right\} = \left[\Phi(\underset{\sim}{x})\right] \left\{U_i^{(-)}(t) \right\} \tag{1.12}$$

since $\left\{\delta \Delta U_i(t) \right\} = 0$. The discrete form of the virtual work expression is altered only slightly due to presence of the dislocation, so that in place of Eq. (1.9) we get

$$\left[M\right]\left\{\ddot{U}_i^{(+)}(t) \right\} + \left[K_{ij}\right]\left\{U_j^{(+)}(t)\right\} = \left\{ \bar{P}_i^{(+)}(t) \right\} \tag{1.13}$$

where $\left\{U_i^{(+)}(t)\right\}$ is given by Eq. (1.11) and

$$\left\{\overline{P}^{(+)}(t)\right\} = \left\{\overline{P}(t)\right\} + \int_{V^{(-)}} \left[\Phi(\underset{\sim}{x})\right]^T \rho \left[\Phi(\underset{\sim}{x})\right] dV \left\{\Delta \ddot{U}_i(t)\right\} + \int_{V^{(-)}} \left[\frac{\partial \Phi}{\partial x_k}(\underset{\sim}{x})\right]^T E_{ikjl} \left[\frac{\partial \Phi}{\partial x_l}(\underset{\sim}{x})\right] dV \left\{\Delta U_i(t)\right\} \quad (1.14)$$

We note that there is an approximation inherent in this development as well as in conventional dislocation theory regarding the manner in which continuity of tractions is achieved across the dislocations. Traction continuity is maintained between adjacent (+) and (-) points which are not aligned across Σ in the dislocated state. In the above finite element formulation, force equilibrium is maintained between complementary halves of each bifurcated node along Σ even though the nodes are separated by $\Delta U_{in}(t)$. This approximation could be eliminated in the numerical treatment; however, the added complexity is not needed to simulate earthquake phenomena where the fault displacement is very small compared to the size of the elements.

In looking ahead to future numerical simulations of an earthquake event, we note that traction conditions on Σ can more closely simulate an earthquake rupture process in a prestressed medium than specifying $\Delta U_i(t)$ on Σ. This case is handled by simply introducing traction boundary conditions along the rupture zone. For example, the slip-stick rupture process could be simulated numerically by adjusting $S_\sigma = \Sigma(t)$ of Eq. (1.8) as the rupture progresses. Sliding friction simply indicates nonzero $\overline{\tau}_i$ along $S_\sigma = \Sigma$.

For the purpose of this thesis, we restrict ourselves to time-independent modeling of heterogeneous dislocation phenomena. The character of the dislocation is specified by $\left\{\Delta U_i\right\}$ which is converted into a load vector (concentrated forces applied at the node points) by Eq. (1.14) with $\left\{\Delta\ddot{U}_i\right\} = 0$. The nodal displacements $\left\{U_i^{(+)}\right\}$ are obtained by solving Eq. (1.13) with $\left\{\ddot{U}_i\right\} = 0$. The complementary set of nodal displacements $\left\{U_i^{(-)}\right\}$, which differ from $\left\{U_i^{(+)}\right\}$ only in the region $V^{(-)}$ adjacent to the fault, are given by Eq. (1.11). Stresses are obtained from the nodal displacements by substituting Eq. (1.1) into Eq. (1.5) so that

$$\sigma_{ik}^{(+)}(\underset{\sim}{x}) = E_{ikjl}\left[\frac{\partial\Phi}{\partial x_l}\right]\left\{U_j^{(+)}\right\} \qquad (1.15)$$

for $\underset{\sim}{x}$ in $V^{(+)}$, and

$$\sigma_{ik}^{(-)}(\underset{\sim}{x}) = E_{ikjl}\left[\frac{\partial\Phi}{\partial x_l}(\underset{\sim}{x})\right]\left\{U_j^{(-)}\right\} \qquad (1.16)$$

for $\underset{\sim}{x}$ in $V^{(-)}$.

This "dislocation" approach may result in net increase of strain energy of the system (see Chapter III of this thesis) because it is insensitive to the prestress field. The fault offset is imposed on the nodes that define the fault surface instead of the more natural approach of letting the offset be determined by the forcing function: the distribution of the prestress.

A "relaxation" of stress can be used as an alternative. This is done using static linear elasticity theory by comparing two equilibrium situations. The first is calculated for a set of displacement boundary conditions, which, imposed upon the original model define the prestress field. The second static equilibrium is computed for the same boundary conditions imposed this time on a finite element grid where a row of elements defining the fault gouge have been assigned the elastic constants of a near fluid. The resulting stresses define the final stress field, and the difference between the two models defines the relative displacement and stress change.

By varying the amount of "relaxation" defined as the change in shear modulus of the "fault gouge", one can reproduce the relative displacement distribution that would result from an equivalent "dislocation". Because of the finite thickness of the elements "relaxed", care must be taken to avoid dilation of the fault gouge. This is controlled by Hooke's law

$$\tau_{ij} = E_{ijkl}\epsilon_{kl} \tag{1.17}$$

which can be written in plane strain as

$$\begin{Bmatrix} \tau_{xx} \\ \tau_{yy} \\ \tau_{xy} \end{Bmatrix} = \begin{bmatrix} d_{11} & d_{12} & d_{13} \\ d_{12} & d_{22} & d_{23} \\ d_{12} & d_{33} & d_{33} \end{bmatrix} \begin{Bmatrix} \epsilon_{xx} \\ \epsilon_{yy} \\ \epsilon_{xy} \end{Bmatrix} \tag{1.18}$$

where the d_{ij} are the 6 elastic coefficients characterizing the anisotropy. If we want the two sides of the fault to slide parallel to the fault plane, however, we can simplify the above formula by using an orthotropic material. Here E_1, ν_1 characterize the Young's modulus parallel to the fault plane, say the x axis, and E_2, ν_2 apply to the y direction, perpendicular to the fault plane. Then (Zienkiewicz, 1972)

$$\begin{Bmatrix} \tau_{xx} \\ \tau_{yy} \\ \tau_{xy} \end{Bmatrix} = \frac{E_2}{(1+\nu_1)(1-\nu_1-2n\nu_2^2)} \begin{bmatrix} n(1-n\nu_2^2) & n\nu_2(1+\nu_1) & 0 \\ n\nu_2(1+\nu_1) & (1-\nu_1^2) & 0 \\ 0 & 0 & m(1+\nu_1)(1-\nu_1-2n\nu_2^2) \end{bmatrix}$$

$$\times \begin{Bmatrix} \epsilon_{xx} \\ \epsilon_{yy} \\ \epsilon_{xy} \end{Bmatrix} \qquad (1.19)$$

(E_1, E_2, ν_1, ν_2, are the Young's moduli and Poisson's ratios) where $n = E_1/E_2$ and $m = \mu_2/E_2$. These coefficients can be chosen such that partial shear stress drop is achieved on the fault surface while maintaining a constant stress normal to the fault. Another technique consists of dropping the shear modulus while maintaining the bulk modulus unchanged. Then, a linear relationship exists between the shear modulus and the thickness of the "gouge". If the amount of shear stress drop parallel to the fault is kept constant, the thickness of the gouge is inversely proportional to the change in shear modulus μ. This will be used in chapter IV of this thesis.

Idealized Fault in a Homogeneous Half Space

Historically, (for static problems) geophysicists have treated faults as a plane surface with a uniform discontinuity in the displacement field tangential to the idealized fault plane. The discontinuity in the displacement field, referred to as a "dislocation", is injected into an elastic continuum by a linear process of superimposing concentrations of force along both faces of the fault plane. The elastic compliance of the continuum to the singular load system is obtained by conventional Green's function techniques; however, the resulting integral expressions that are generated are very difficult and tedious to evaluate. Solutions for a vertical plane of dislocation in a half space of homogeneous Poisson's solid have been evaluated by Steketee (1958a, b) and

Maruyama (1963, 1964). More recently, Savage and Hastie (1966) and Mansinha and Smylie (1971) gave closed form solutions for the more general case of a dipping fault plane. Variations in the earth's structure with depth were introduced (McGinley, 1969) by the superposition of several half-space solutions offset to represent a layered media. The spherical geometry of the earth was introduced by Ben Menahem et al. (1969, 1970) and Singh and Ben Menahem (1969) in order to more closely model the influences of earthquakes at teleseismic distances.

One of the purposes of this study was to determine the accuracy of the finite element method for simulating a dislocation. Unfortunately, getting a closed form solution for a dipping dislocation in a 3-dimensional half space is nontrivial, even with Maruyama's (1964) Green's functions as a starting point. However, it is relatively easy to get the displacements due to an infinite length dislocation in a homogeneous half space and then to compare it with the 2-dimensional finite element solution acting in plane strain.

In particular, the displacements and stress components at a point $Q(x_1, x_2, x_3)$ of a half space due to an arbitrary dislocation are

$$u_m(Q) = \iint_\Sigma u_k(P) W^m_{kl} \nu_l(P)\, d\Sigma \tag{1.20}$$

$$\tau_{mn}(Q) = \iint_\Sigma u_k(P) H^{mn}_{kl} \nu_l(P)\, d\Sigma \tag{1.21}$$

where the integrations are taken over the coordinates of $P(\xi_1, \xi_2, \xi_3)$ on the dislocation surface Σ, where a discontinuity $\Delta u_k(P)$ occurs. W^m_{kl} and H^{mn}_{kl} are the Green's function solutions corresponding to the superposition of strain nuclei at the point $P(\xi_1, \xi_2, \xi_3)$ and at

$P'(\xi_1, \xi_2, -\xi_3)$ (its image across the free surface), plus the Boussinesq problem of vertical loads on the free surface which are needed to satisfy the surface boundary conditions. Using Maruyama's (1964) expressions for the Green's function, we carry out the integration of Eq. (1.20) for a dislocation surface of infinite length (i.e., we integrate over $\Sigma \in [d, D] \times [+\infty, -\infty]$, where d and D are the vertical depths to the shallowest and deepest points on the fault respectively). The results for a vertical fault in dip slip, expressed along the free surface ($x_3 = 0$), are:

Horizontal displacement

$$U_h = \frac{\Delta u_3}{\pi} \left\{ \frac{x_1^2}{x_1^2+d^2} - \frac{x_1^2}{x_1^2+D^2} \right\} \tag{1.22}$$

Vertical displacement

$$U_v = \frac{\Delta u_3}{\pi} \left\{ \operatorname{atan} \frac{D}{x_1} - \operatorname{atan} \frac{d}{x_1} - \frac{x_1 D}{x_1^2+D^2} + \frac{x_1 d}{x_1^2+d^2} \right\} \tag{1.23}$$

For a 45° dip slip fault and d = 0, we have

$$U = -\frac{\Delta u\sqrt{2}}{8\pi} \left\{ \frac{2(2D-x_1)^2 + 4x_1(2D-x_1) + 6x_1^2}{(2D-x_1)^2 + x_1^2} + 4\tan^{-1}\left(\frac{2D-x_1}{x_1}\right) + 2 - 4\tan^{-1}(-1) \right\} \tag{1.24}$$

The finite element procedure described in the previous section was used to model a vertical and 45° plane dislocation acting in plane strain in order to examine the accuracy of the numerical method. A fine mesh of triangular elements is used in the proximity of the dislocation to achieve good accuracy, illustrated in Figure 2. At this point, it bears pointing out that the assemblage of triangles in no way represents an actual cutting out of a half circle into physically separated triangles connected at their corners. Compatibility of displacements guarantees that the junction of elements on their sides is a virtual line rather than an internal discrete boundary. The infinite extent of the half space is approximated by a semicircle, 30 fault dimensions in radius. The continuum exterior to the semicircular assemblage of elements provides some resistance to displacements along the semicircular finite element boundary. The resistance of the exterior continuum is greater than that which would be provided by traction-free boundary conditions on the semicircular finite element boundary, but less than that which would be provided by fixing the finite element boundary displacements to zero along the semicircle. In order to evaluate the effect of truncating the continuum at 30 fault dimensions, we computed results using both the zero traction and the zero displacement boundary conditions. It was found that the results (displacement, strain, and stress) of the two numerical calculations differed by less than 1% within 20 fault dimensions of the numerically induced dislocation.

Figure 3 shows the computed displacements at the free surface for a vertical fault compared to the solution expressed by Eqs. (1.22) and (1.23) for $d = 0$, $D = 16.5$ km, $u_3 =$ constant $\overline{u}$. The finite element displacement field obtained with the same parameters, compared within about 1% accuracy out to 15 fault widths away from the dislocation.

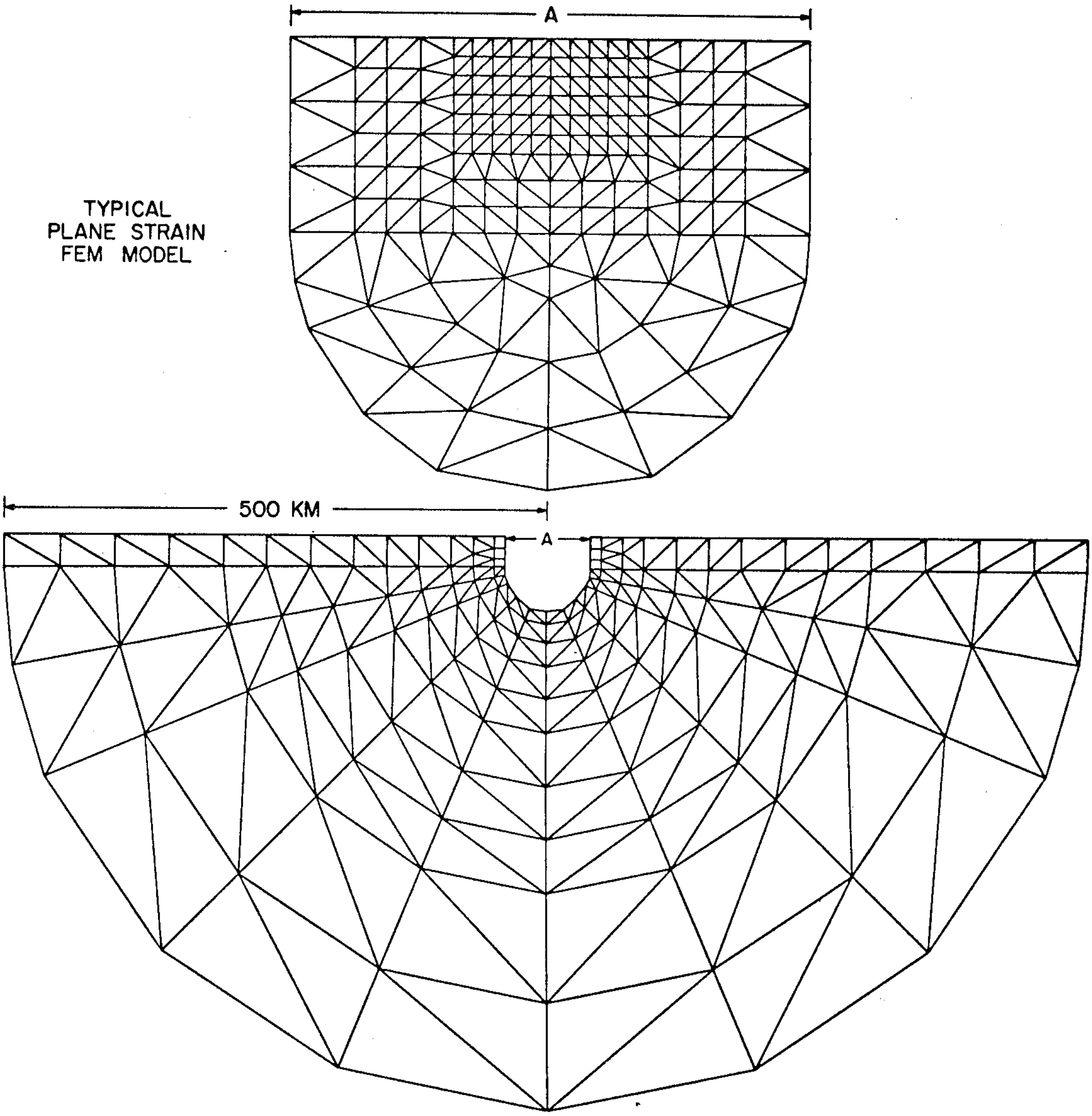

Figure 2. Typical finite elements grid used in this study. The dimensions are of a half circle with 500 km radius.

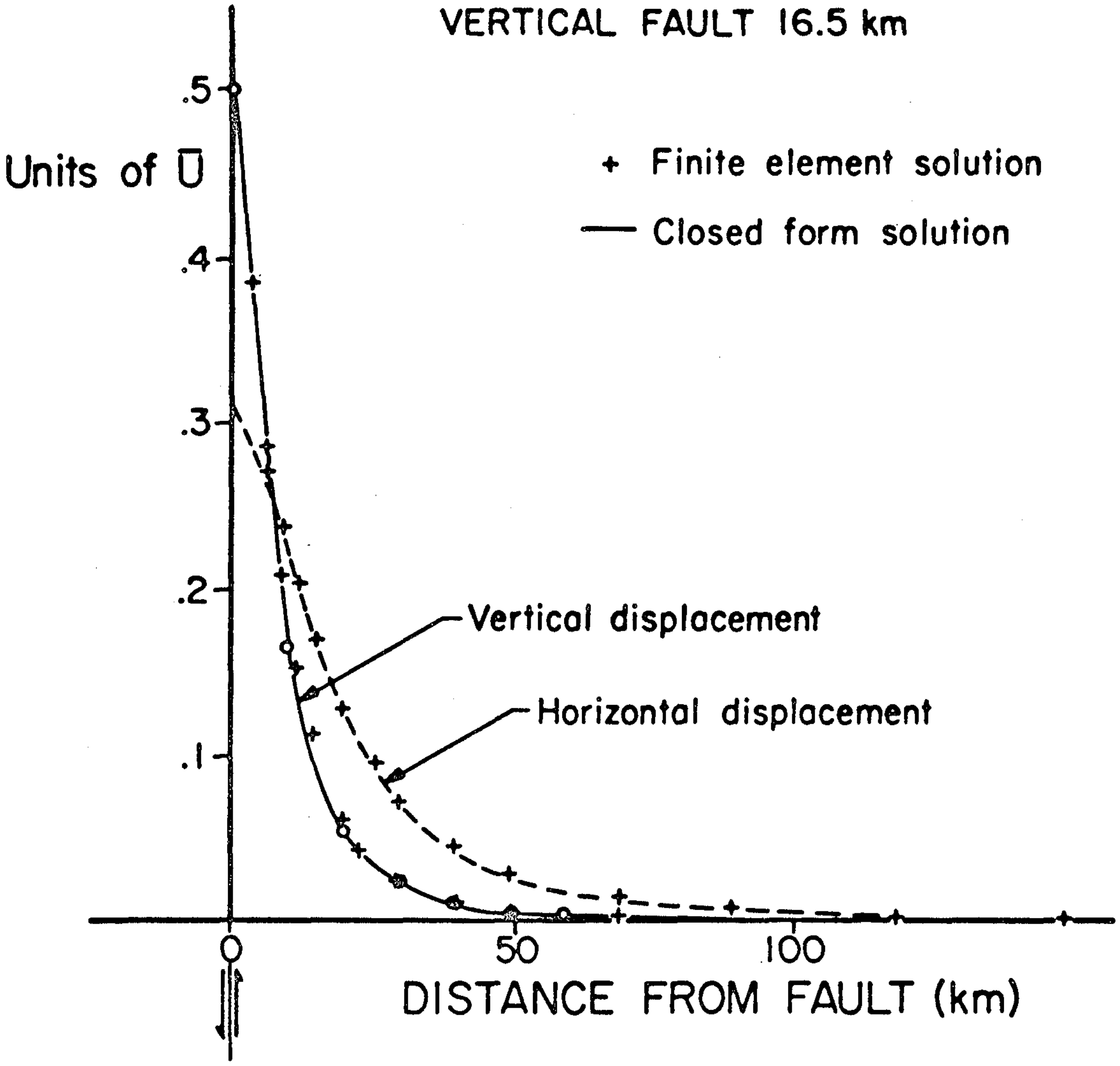

Figure 3. Horizontal and vertical displacements at the free surface for an infinite length fault. Vertical dip slip. The other side is symmetrical.

Figure 4 shows a similar comparison between a plot of Eq. (1.24) with the finite element solution using the parameters above. On Figure 4 we also show the vertical displacement of the free surface for a dislocation which dies out linearly, from $\overline{u}$ at the surface to zero at the hypocenter. This is discussed in the next section, but at this point we note that this particular variation changes the sign of the tilt along a considerable length of the free surface.

A number of other solutions were calculated using variations of these parameters. In all cases the finite element code gave surface displacements in agreement with those obtained from the closed form solutions to a high level of accuracy.

Influence of Fault Complexities

We now wish to proceed from a simple homogeneous half space with constant dislocations to more complex models. As was noted in the introduction, the major problem with earthquake fault modeling is with inhomogeneities in the medium or on the fault plane itself. Since our numerical code allows for variations in structure, elastic properties and dislocation distribution, we made a systematic parameter study in order to determine their relative influence upon the solution behavior.

Figure 5 shows the influence of variations of the relative displacement along the fault width. For the sake of discussion we choose to show the extremes among all the variations of fault behavior that we have studied. In all cases, the fault, infinite in length, is a thrust fault dipping at 45°, with a focus at 10 km depth. Comparison is made

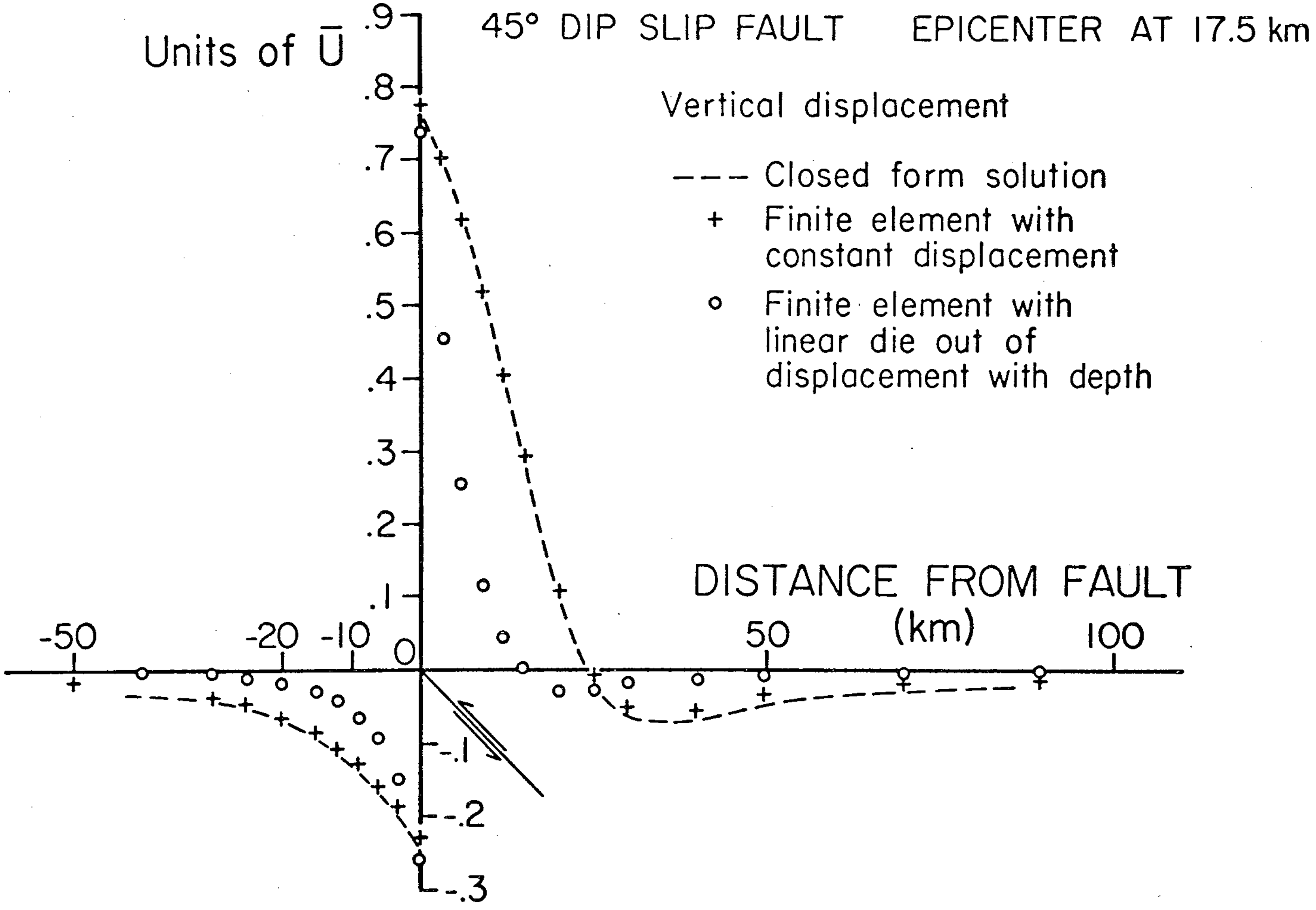

Figure 4. Vertical displacement at the free surface for a 45° dip slip fault. Numerical solution for a linear die out of the offset with depth shows a reversed sign of the tilt from 20 to 40 km to the right of the fault. $U = \sqrt{2} \times U$.

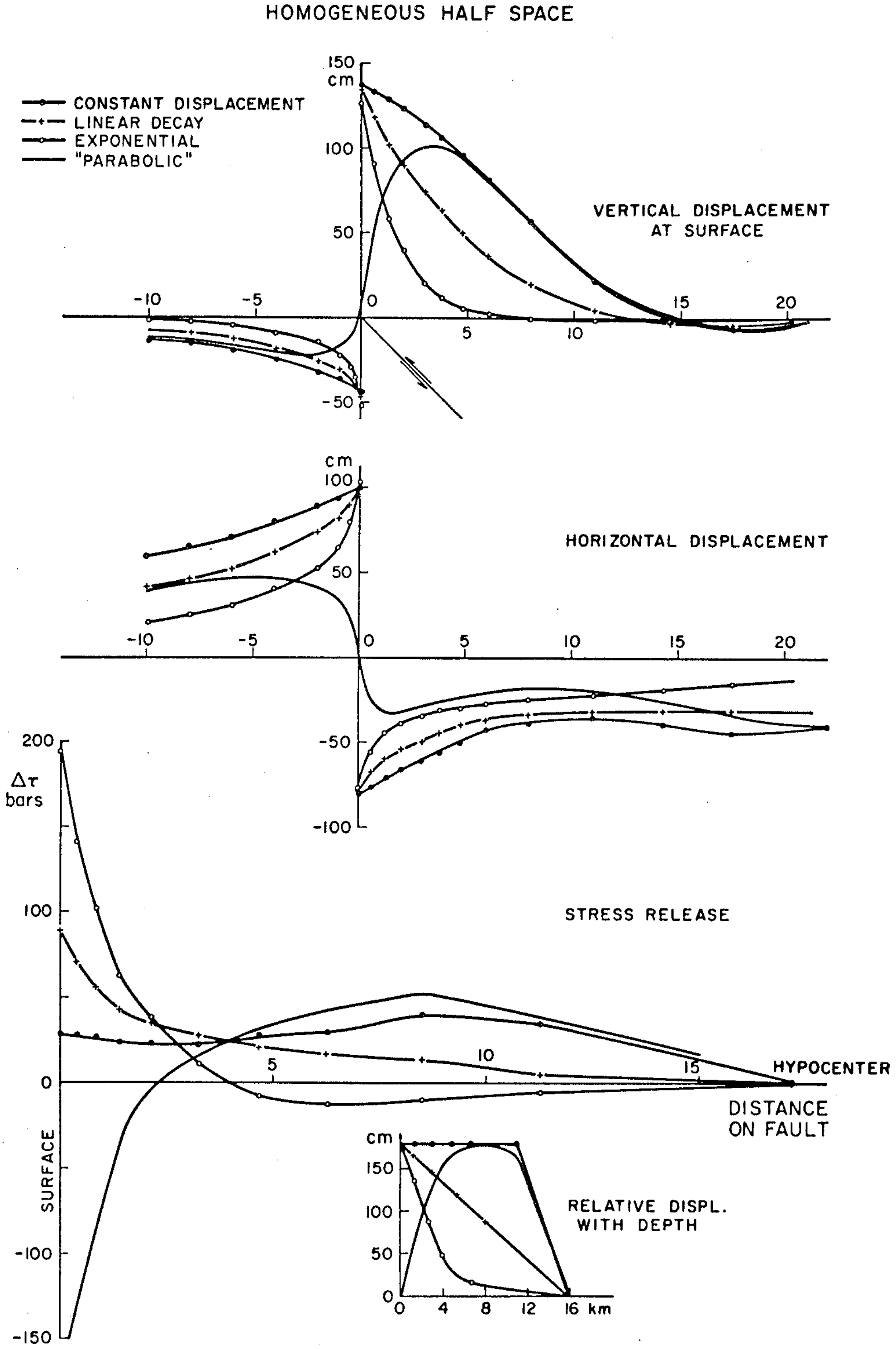

Figure 5. Influence of variable offset upon the surface movements. Negative horizontal displacement is to the left. Stress drops are approximate.

between quasi constant dislocation, linear decay, rapid exponential decay and quasi parabolic dislocation displacement, as shown at the bottom of the figure.

The vertical displacements at the free surface clearly reflect the behavior of the dislocation. This implies that, if good observations are available, it should be possible to discriminate between the various extremes of fault movement at depth. Estimates of average slip along the fault could then be made with reasonable accuracy.

The horizontal displacements on the other hand do not reflect the nature of the subsurface faulting so clearly except in the case of a "parabolic" dislocation. The horizontal displacement it causes is the only one exhibiting a relative shortening on either side of the fault.

The plots of stress release along the fault surface show some very interesting features. Because of the linear assumptions inside each element, these stresses are an underestimate of the true stress drop on the fault surface. While the constant dislocation model causes a relatively constant stress release with an average stress drop of 30 bars, the model with linear decay shows a stress release which is insignificant at depth and grows to 90 bars at the free surface. This situation is accentuated in the case of the exponential decay of the dislocation, where the fault surface appears to be loaded at depth while releasing abnormally high stress at the surface. The parabolic dislocation on the other hand causes a high stress release at depth while loading the surface.

It should be remembered at this point that all of these models are for a homogeneous Poisson's solid. Clearly, in a real situation the shear modulus of the rock will increase with depth, if only because of the overburden. Therefore, the stress drop will be increased at depth and decreased near the surface.

Figure 6 shows the influence of some simple structural units on the solution. The elastic constants used in the model are listed in Table 1 and the geometry of the models is shown at the bottom of the figure without vertical exaggeration. The order of magnitude contrast between the alluvial valley and the homogeneous half space is the outstanding factor here. In the model of a layered half space, extremes are chosen for the shear modulus of the upper mantle and the low velocity zone in order to bound their effect.

The influence of these inhomogeneities upon vertical displacements is very limited except for alluvial model #1, where the surface rises by some 20 cm before reaching the fault on the left side. On the other hand, the horizontal displacements react strongly to the presence of the soft valleys mainly because they offer less resistance to the moment that exists at the tip of the fault.

The stress drop along the fault is reduced by a factor of 5 when the fault goes through the soft formation. This seems to imply that in a situation like that of alluvial valley #2 in order to maintain a constant stress drop along the fault, the dislocation would have to increase very significantly as it approaches the surface where geological units with low shear modulus exist.

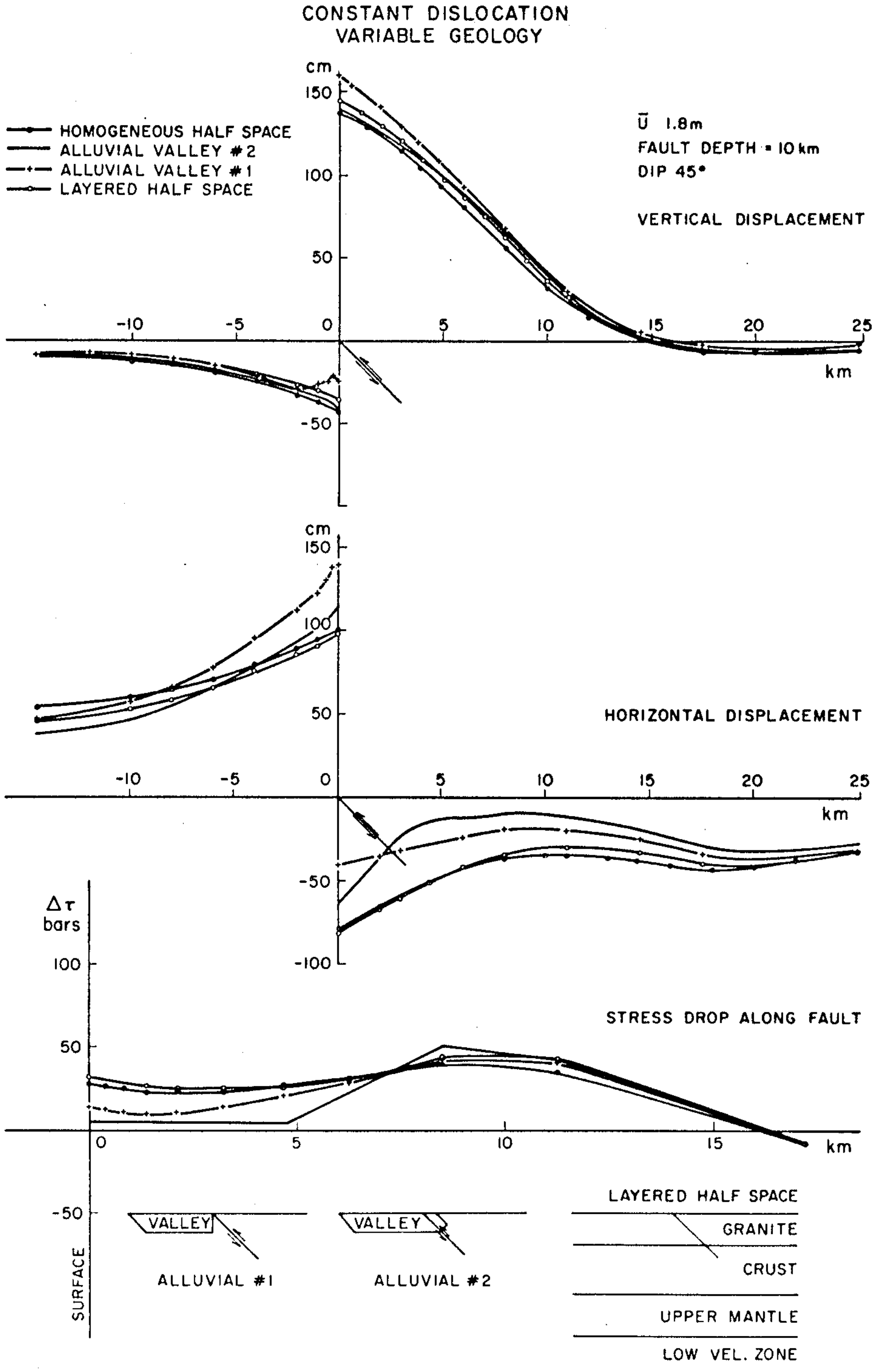

Figure 6. Influence of simple geology upon the solution of a 45° dip slip fault with a constant offset.

TABLE 1

Parameters

Formation	(g/cc)	V_s	V_p	G or μ dyne/cm	λ	ν or σ	Reference
San Fernando Valley	2.1	1.2	2.5	$.3\text{x}10^{11}$	$.710\text{x}10^{11}$	.35	Estimate
Saugus	2.5	2.5	3.8	$1.5\text{x}10^{11}$	$1.2\ \ \text{x}10^{11}$	.222	Estimate
San Gabriel Mt.	2.71	3.4	5.8	$3.13\text{x}10^{11}$	$2.85\text{x}10^{11}$	.238	Wood-Richter (1933)
Mohave Desert	2.8	2.8	5.1	$2.19\text{x}10^{11}$	$2.89\text{x}10^{11}$	.284	Estimate
Santa Monica Mt.	2.6	3.2	5.5	$2.66\text{x}10^{11}$	$2.54\text{x}10^{11}$	.244	Estimate
Crust	3.0	3.4	6.06	$3.46\text{x}10^{11}$	$4.\ \ \text{x}10^{11}$	.27	Gutenberg (1944)
Upper Mantle	3.3	4.56	8.04	$6.14\text{x}10^{11}$	$6.75\text{x}10^{11}$	.261	CIT (Anderson)
Low Velocity Zone	3.3	4.21	7.37	$5.6\text{x}10^{11}$	$6.13\text{x}10^{11}$	.261	CIT IIA (1967)

The horizontal strain caused at large distance by these various dislocations are listed in Table 2. Distances of 120 km and 150 km were chosen as examples. Boundary effects are seen at larger distances in the numerical results.

The main conclusion from this table is that order of magnitude errors can occur if earthquake strains are simulated by a constant dislocation in a homogeneous half space rather than the more realistic situation of a variable dislocation controlled by geology and prestress. This is very important if one wants to interpret strain offsets at teleseismic stations. Of course, our model is 2-dimensional and at distances greater than the actual fault length, end effects would be felt.

This simple parametric study demonstrates, however, that if the local geology is well known and precise zero frequency data are available, the finite element method can be employed for a detailed analysis of an actual earthquake event and fault displacement, stress drop, moment and the source dimensions can also be determined, as we demonstrate in the following chapter on applications.

Table 2

Horizontal strain caused by a 45° dip slip fault as described in Figures 4 and 5. Scale factor 10^{-7}.

Model	Distance from fault:	120 km	-120 km	150 km	-150 km
Constant Dislocation					
Homogeneous half space		6.55	5.8	5.	3.8
Layered half space		3.56	3.2	2.8	2.1
Valley #1		5.4	4.5	4.2	3.
Valley #2		4.9	4.1	3.8	2.7
Homogeneous Half Space					
Constant dislocation		6.55	5.8	5.	3.8
Linear decay		3.9	3.6	3.	2.3
Exponential decay		1.6	1.5	1.2	1.
Parabolic dislocation		5.3	4.6	4.	3.

II. TWO-DIMENSIONAL MODELS OF THE 1971 SAN FERNANDO AND 1964 ALASKA EARTHQUAKES

Introduction

We have demonstrated the validity of the finite element technique for numerically modeling "dislocations" in a complex geological model. The method will be applied to two earthquakes characterized by a relatively large amount of reliable zero frequency observations in an attempt to invert these data to obtain the displacement offsets that occurred on the fault surfaces.

The San Fernando earthquake was chosen because of the extensive post-earthquake geodetic survey performed by several investigators. Because the pre-earthquake survey dates back an average of 5 years before 1971, it was felt that net changes would be polluted by little if any secular movement, thus guaranteeing unusual accuracy in the net vertical movement measured. The Alaska earthquake, aside from the intrinsic interest in it, was chosen because its length, estimated to be as much as 600 km, makes it a perfect candidate for plane strain modeling.

Plane strain modeling of the San Fernando earthquake, however, gives us a less accurate approximation. The total fault length of this fault is equal to its fault width, and as is shown below this would allow an accurate plane strain model of the middle of the fault. But, on the basis of the observations, we divided the fault length into two segments, which are characterized by differences in their geological setting and significant variations in their free surface behavior. This leads us to model in plane strain two segments of fault with a fault length smaller than their width. This should result in an underestimate of the fault's offsets at depth. However, since the two cross sections studied are only 3 km apart, they are not independent from one another, and their interaction can be estimated to improve each inversion. Thus, the overall accuracy of the results is felt to be sufficient to justify the use of two-dimensional modeling.

The next section presents a short discussion of the validity of two-dimensional elasticity applied to three-dimensional problems.

1. Plane Strain Assumptions

Either plane strain or plane stress can be used here since, in principle, they are interchangeable. Any plane stress problem can be solved as a plane strain problem by replacing the true value of the Poisson's ratio ν, by an apparent value $\nu/(1-\nu)$.

However, in plane strain one assumes that

(1) $\partial u_i/\partial z = \text{const.}$, i.e., a uniform state of strain exists in the third dimension

(2) no body forces exist in the third dimension

(3) no surface tractions exist in the third dimension on the boundaries.

These requirements satisfy all of the equations of elasticity (motion, compatibility and constitutive equations). Thus, provided that the problem at hand can be posed in terms of plane strain, the solution will be exact.

In plane stress, however, the first requirement of the above is changed to requiring no stress in the third direction, i.e.

$$\tau_{zz} = \tau_{xz} = \tau_{yz} = 0$$

As a result, by contrast with plane strain, there is here an approximation involved because the above condition does not satisfy all of the compatibility equations.

All of the subsequent models will then be treated in plane strain, and the third component of stress is

$$\tau_{zz} = \nu(\tau_{xx} + \tau_{yy})$$

and the components of displacement will only be functions of x and y, not of z, i.e.

$$u = u(x, y)$$
$$v = v(x, y)$$

For models of earthquakes, this means that our solutions are exact if and only if

(a) The only body forces to consider are either vertical (force of gravity) or in the xy plane (there exist tectonic forces only parallel to the cross section under consideration),

(b) No components of tractions exist in the z direction on the outer or inner boundaries. Clearly this is the condition most influenced by the fault ends effects. However, Figure 7 shows the free surface vertical displacements caused by a fault dipping at 45° for a cross section at the middle of the fault. One part of the figure is for a fault with hypocenter at 8 km which breaks the surface and the other part is

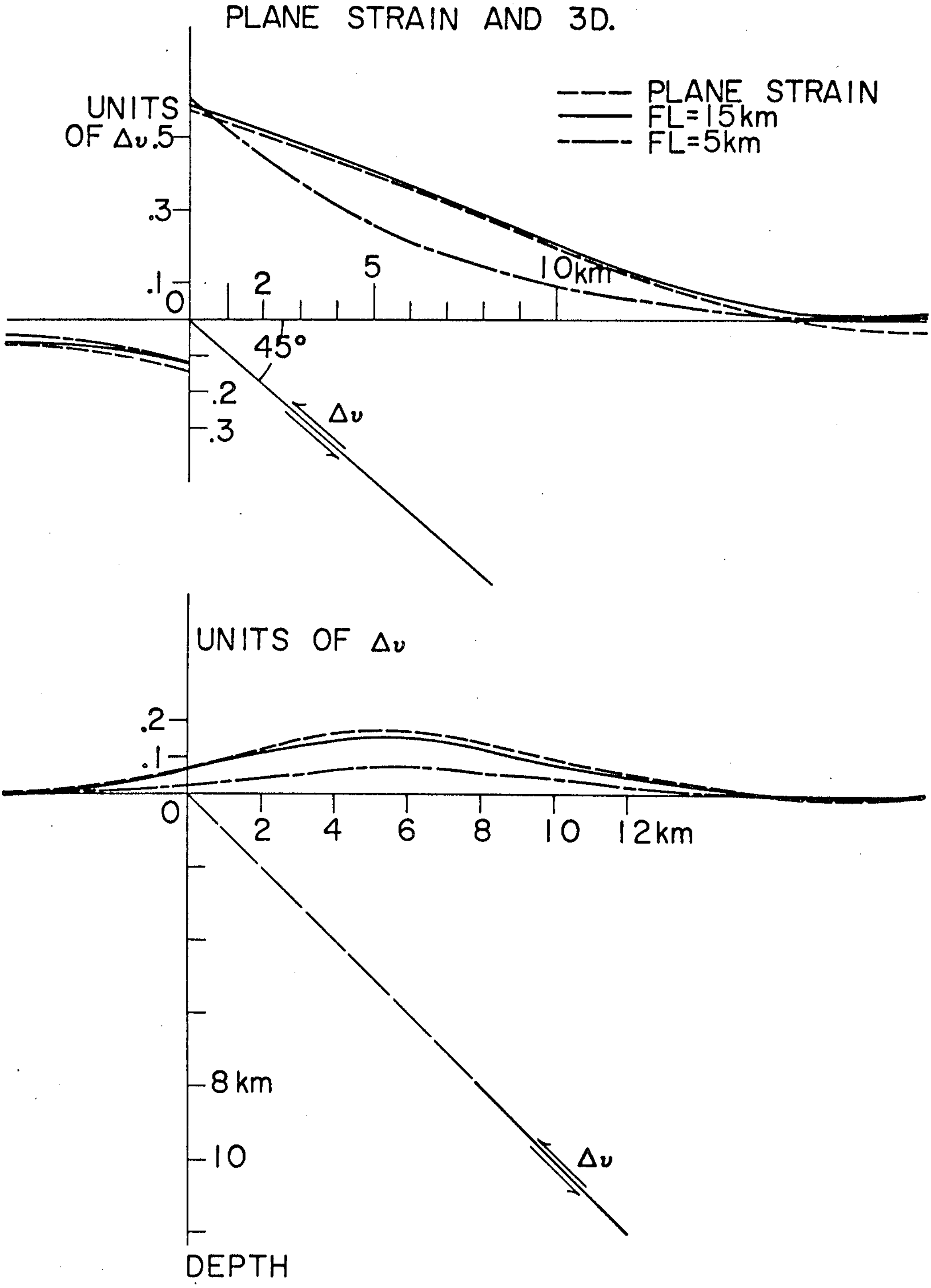

Figure 7. Analysis of the fault length (FL) influence upon the vertical movement of the free surface.

for a fault with hypocenter at 12 km and stopping at 8 km depth. As can be seen, for fault length equal or superior to the fault width, the resulting free surface displacement is essentially the same as that caused by an infinitely long fault, equivalent to plane strain. For a fault length much smaller than the width, the vertical offset is reduced significantly from that obtained by plane strain modeling. As a result, it can be stated that if the fault is square or close to it, the plane strain model is a very accurate representation of the middle of the fault. If the fault length is much smaller than the fault width, the plane strain inversion of vertical offset data will lead to a underestimate of fault slip at depth.

(c) No warping of the plane is permitted in the z direction. By placing the cross section in the middle of the fault, one guarantees that the displacements in the plane (x, y) considered are not functions of the third coordinate. The displacement plots of Press (1965) for strike slip and dip slip faults clearly show that no vertical movement exists on the middle section of a strike slip fault.

The San Fernando Earthquake

Observations and models

The San Fernando earthquake occurred on February 9, 1971, and the associated permanent displacements were extensively recorded. In addition, estimates of other event characteristics, including magnitude, moment, focal mechanism and tectonic interpretations can be obtained from the combined work of a number of investigations (e.g., Canitez and Toksöz, 1972; Savage et al., 1972; Whitcomb, 1971; Allen, Hanks, and Whitcomb, 1972; Wyss and Hanks, 1972). As a result, the San Fernando earthquake is an ideal event for finite element simulation, our hope being, of course, that this technique will give us a fit to all the zero frequency data as well as tell us something about the subsurface environment in which the failure occurred.

Figure 8 shows a contour map of the change in vertical geodetic control in the region affected by the event. The data used in this figure are a combination of data from Savage, Burford, and Kinoshita (1972), Alewine (1972), Kamb et al. (1971) as well as data from the U. S. Geological Survey staff report (1971). The general pattern is a very abrupt upwarping of the surface associated with two major fault breaks: the Sylmar fault to the west and the Tujunga fault to the east.

The short Sylmar fault outcrops in the alluvial deposits and curves southward in its westernmost portion and becomes more left lateral as opposed to thrusting. The contours indicate that the vertical displacements begin to taper off immediately north of the fault scarp without significant warping.

The longer Tujunga segment underlines the boundary between alluvial and more indurated upper Tertiary sediments. In this area, there is a sharp increase of vertical displacements north of the fault scarp. As a result the maximum uplift is found some 1.2 km north of the eastern segment of the fault and immediately behind the western segment. It is up to 2.30 m to the east compared to 1.50 m to the west, and the en-echelon arrangement of the faults is not maintained in the vertical uplifts.

In our model we limit ourselves to plane strain, attempting to fit two distinct cross sections (AA' and BB' of Fig. 9). While the fault is not infinite in length and our two-dimensional models neglect the end effects as well as the left lateral component of displacement, we feel that these effects would not modify the vertical uplift significantly since the cross sections are in the middle of both fault segments.

Cross sections chosen as representative, along with the geology that we included in our numerical solutions, are shown in Figure 9.

Along the section AA', through the middle of the Sylmar fault segment, the surface observations indicate an uplift increasing to 35 cm at the southern fault wall, with an additional offset of 1.1 m at the fault break. North of the scarp the displacement grows to a maximum of 1.5 m at a distance of 300 m from the fault and then decreases exponentially to 30 cm, 4 km to the north. The data near the epicenter are most likely influenced by secular uplift of the San Gabriel mountains, and it is probable that some of the other data contain a proportion of this secular variation (in this regard, see Savage et al., 1972).

The geology in the Sylmar area is sketched on the cross section. We have chosen a boundary between the basement and the Saugus formation which implies a history of overthrusting of the San Gabriel block in the southwest direction (L. T. Silver, personal communication). The Saugus formation (Pliocene to Miocene sediment deposits) is a faulted, tipped syncline (Palmer and Henyey, 1971), and for simplicity we chose the boundary to be vertical along the contact with the younger San Fernando Valley sediments. The basement underlying the San Fernando

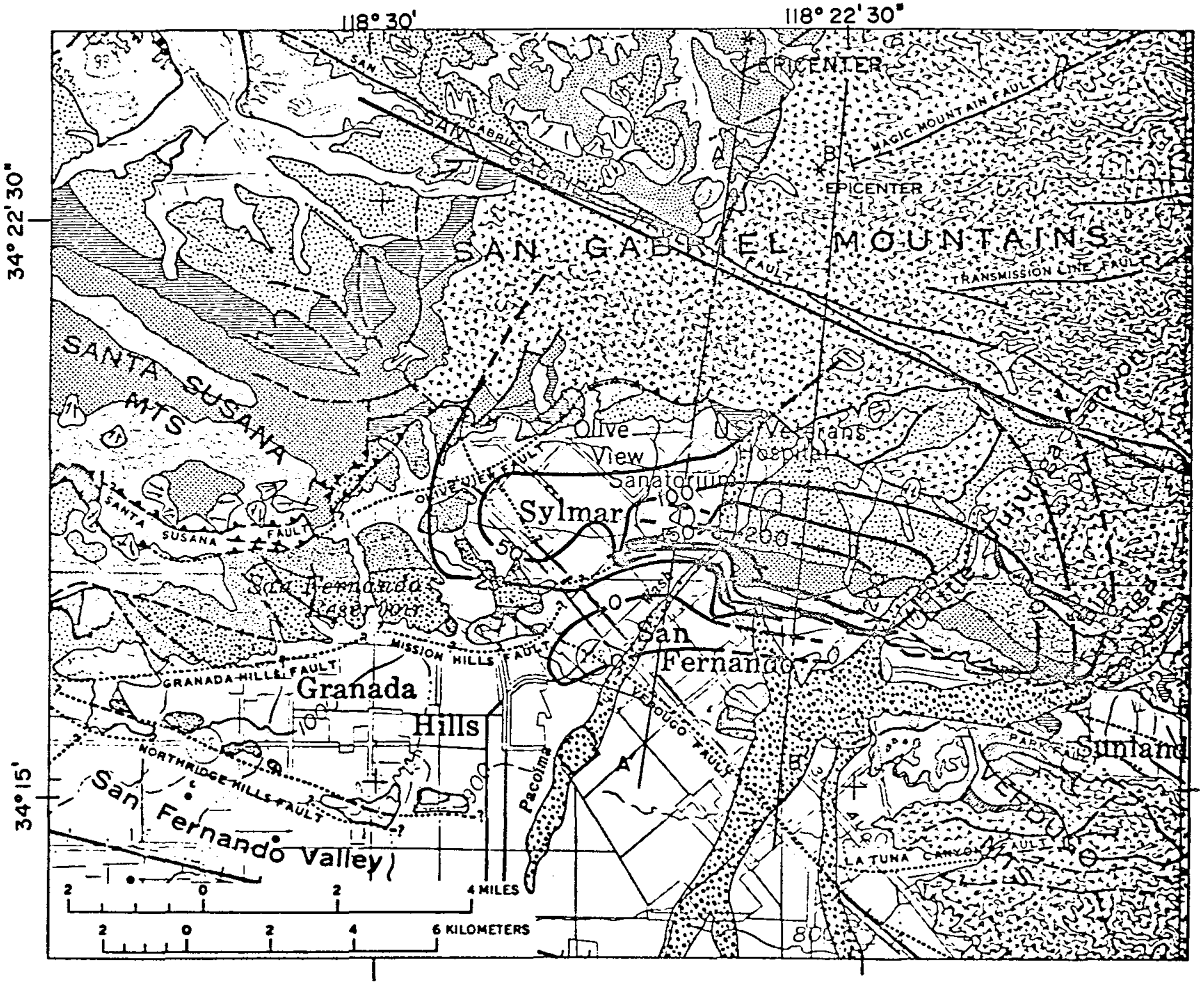

Figure 8. Contours of change in vertical controls caused by the San Fernando earthquake. Geological map from Wentworth and Yerkes, 1971.

Valley is taken to be at a depth of approximately 4 km, based on maximum sediment thickness cited by Wentworth and Yerkes (1971).

Section BB' is 2.5 km east of AA' and is very different in its geological setting. We also observe quite different displacements. No displacements larger than 10 cm are observed to the south. North of the scarp a sharp rise of the surface is recorded with a maximum of 2.30 m, with an exponential decrease northward similar to the one of section AA'.

Important differences in the local geology are observed in this area. In particular, 3 km to the south of the fault, outcrops of Mint Canyon and Topanga formations as well as volcanic rocks and basement complex are observed, probably representing a prolongation of the Verdugo Mountains. We represent these variations in our model by bringing up the basement complex in a crude syncline fashion. Lower Tertiary sediments are represented in the same way by the Saugus formation outcropping some 2 km to the south of the Tujunga fault scarp. This leaves a small valley of San Fernando alluvial deposits occupying the center of the "Saugus syncline". The elastic properties of the geological units are listed in Table 1. They are intended to give the best average velocities for the ensemble of formations included in these units. The values chosen for the San Fernando alluvial deposits immediately adjacent to the fault in section AA' are deliberately taken to be low so as to approximate the properties of loose gravel, sand and silt. All of the models used include crust and upper mantle layering as previously described.

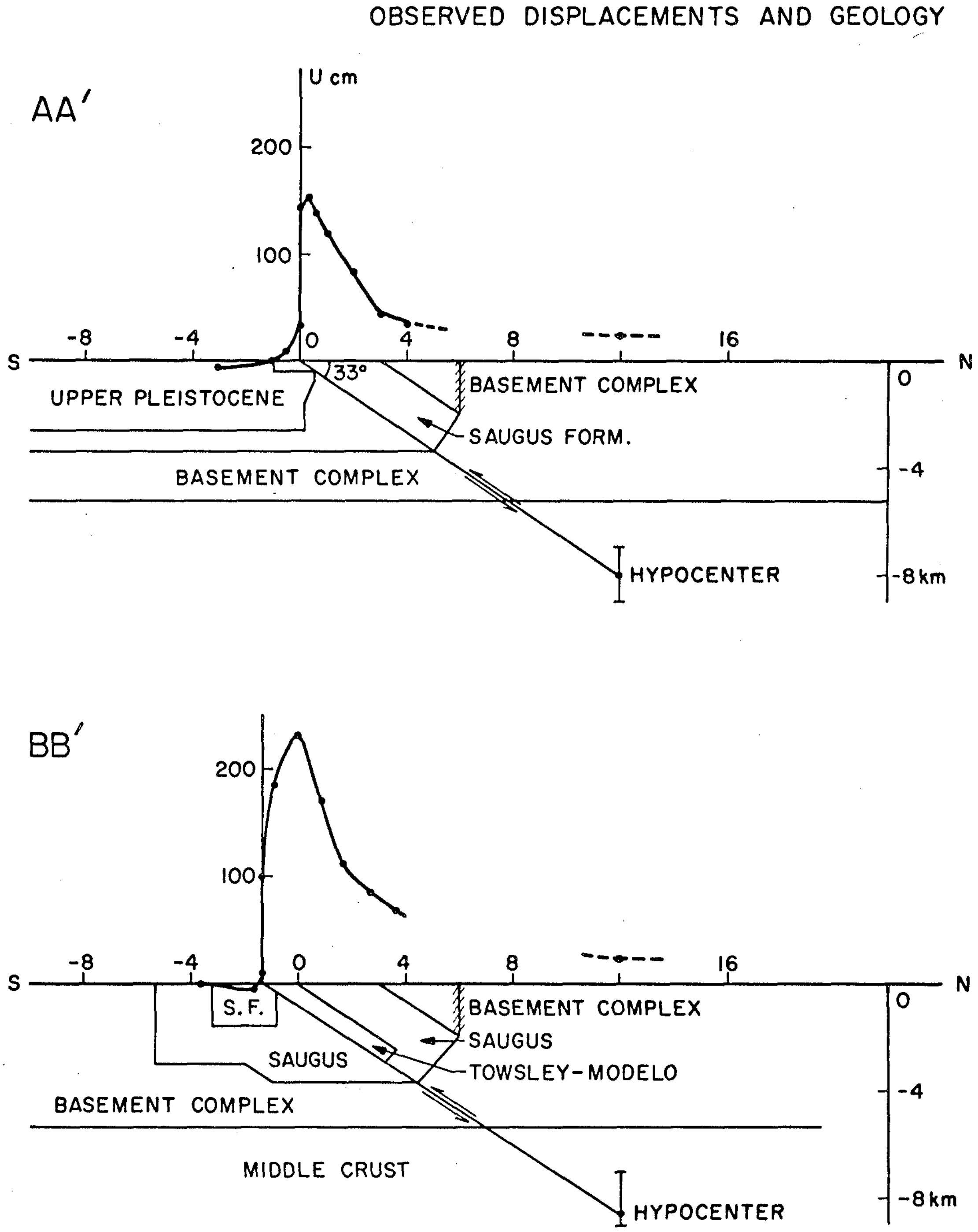

Figure 9. Observed displacements and assumed simplified geology for section AA' and BB'. The elastic properties of the units are in Table 1.

Finite element solutions

Figure 10 shows the results for section AA'. The best solution in terms of vertical displacements on the south side was obtained with a fault dip of 33° with an epicenter 12 km north of the scarp and with a hypocenter at 8.0 km depth. This fits the best fault plane solutions obtained by Allen, Hanks, and Whitcomb (1972). We consider the fit to be acceptable in spite of the fact that we do not closely fit the 24 cm uplift observed above the epicenter. However, we believe that this data point is contaminated by a large component of secular strain, and consequently have allowed the solution to yield smaller vertical offsets at this point.

The horizontal displacements are plotted in Figure 10, the negative values indicating movement toward the south. These values are difficult to compare to surveyed data published by Savage _et al_. (1972) because the data have not yet been reduced from changes in surveyed line length values to absolute displacements.

Figure 11 shows the comparison of observations with our best finite element solution for section BB'. Here again the fit for vertical displacements is excellent except for the observation near the epicenter. The fault used for the solution dips 33° to the north which gives a hypocenter 13.3 km north of the fault scarp with a depth of 8.5 km. On the plot of horizontal displacements we indicate the projected position of two stations used by Savage _et al_. (1972) in their line length change study. Stations PL1 and Mesa are 5442.8 m apart and showed a shortening of 1.23 m between 1935 and 1971. In our solution, we find a lengthening

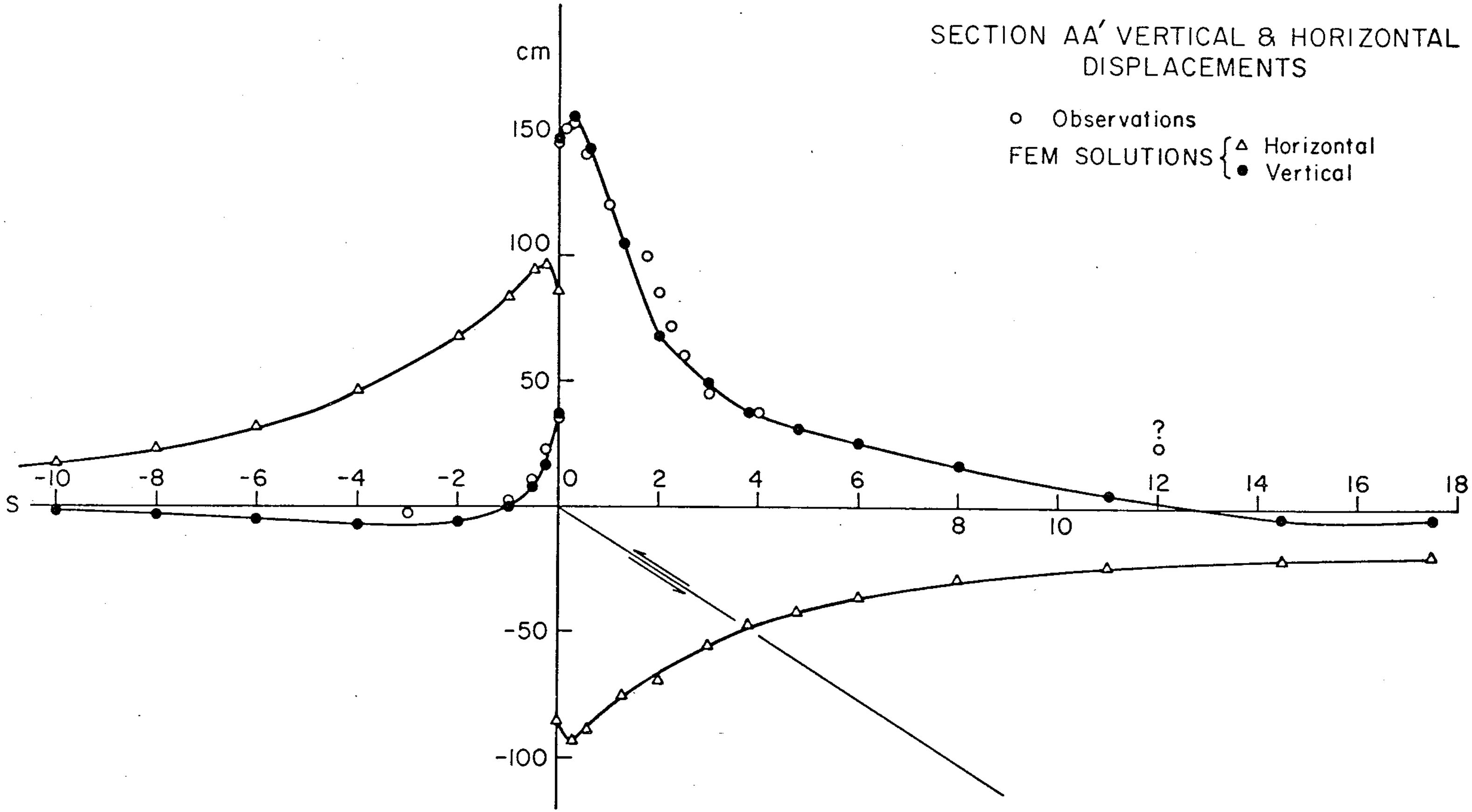

Figure 10. Positive displacement indicates uplift and movement to the right. Fault dips at 33.3°.

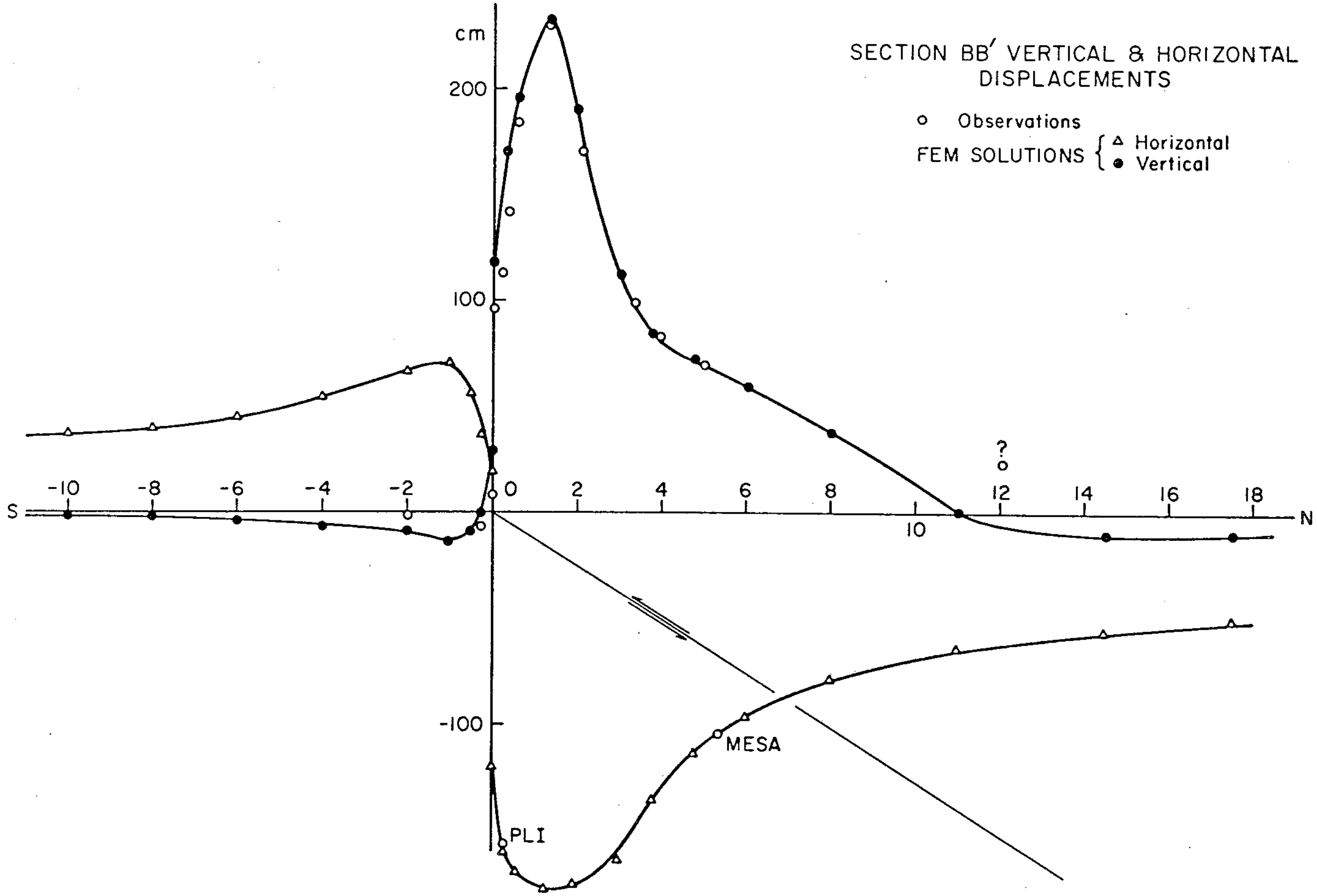

Figure 11. This figure has a zero abscissa actually 1.3 km to the left of the one in Fig. 10. Mesa and PL1 are stations used by Savage et al. (1972).

of approximately 50 cm. Section BB' is almost parallel and 1 km to the east of the line PL1-Mesa, and we do not expect that a left lateral component or secular strain variation could explain a discrepancy of 1.75 m. This discrepancy can be avoided by using a multiple fault system as we will show.

Figure 12 gives a comparison of the relative displacements applied to the fault surface for the solutions shown in the previous figures. The connection between the portions of the fault plane represented by sections AA' and BB' is a complication of the simple picture presented here. Clearly, since the sections are only 3 km apart, large differences in the fault offset in these two portions raise questions as to the accuracy of our plane strain models. This will be investigated in the conclusions of this thesis. In both cases in order to fit the vertical displacements we need a "dislocation" which grows linearly from the focus to a uniform value near the average, followed by an exponential growth to a relative displacement four times larger than the average value over the fault. A rapid decay from the maximum offset is then required to give the observed fault scarp offset.

A possible explanation for this behavior is that the dislocation grows when it encounters a softer material like the Saugus formation and begins to decay before reaching the surface because of plastic deformation in the surface material.

The maximum value of the relative displacement in our best solution for BB' is quite large. Furthermore, its rapid variation implies strains in the neighborhood of 4×10^{-3}, which could cause

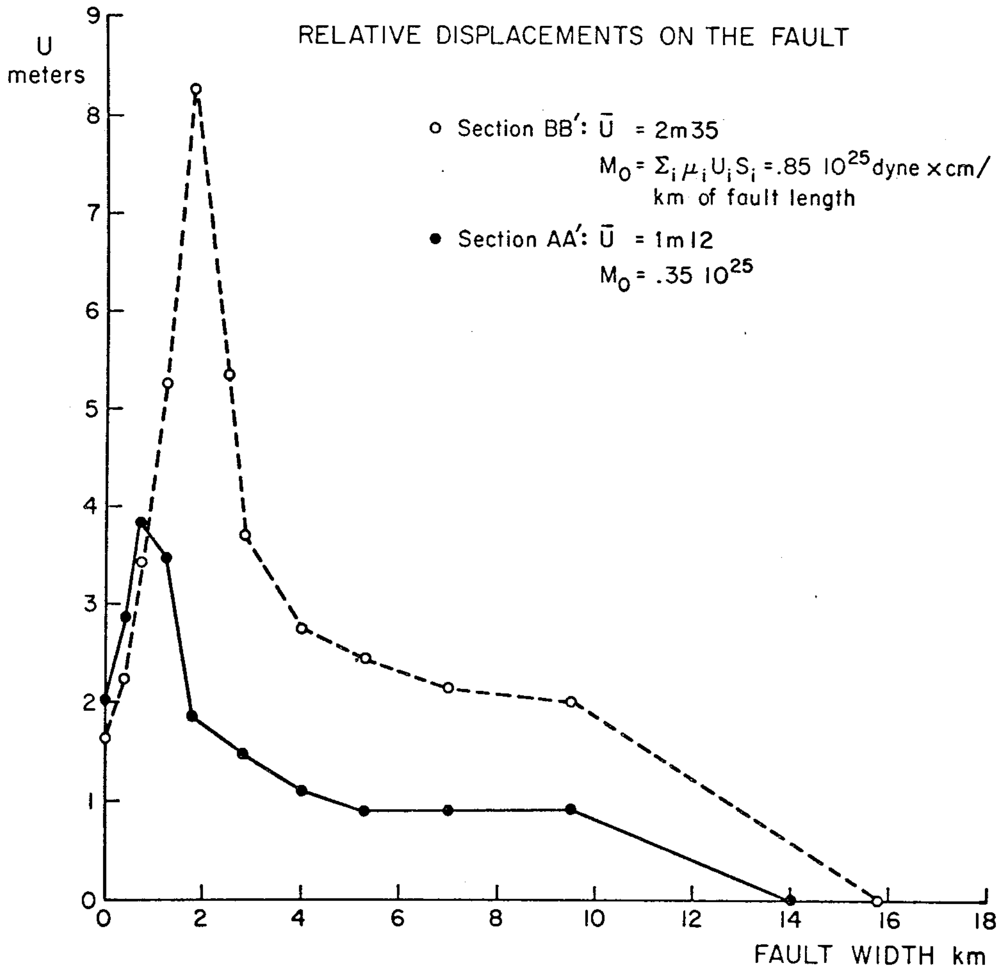

Figure 12. Relative displacements giving the "best fit" for both cross sections. For true comparison BB' should be shifted 1.8 km to the left.

further fracture or creep phenomenon.

Figure 13 shows the stress drop along the fault surface for both cross sections. For both cases the stress drop remains close to the average over the whole fault. The small decrease in the stress drop upon entering the Saugus formation may be due to the sharp boundary between the basement and younger sediments. We consider this to be tenuous since we do not have sufficiently detailed structural data to resolve such behavior. Once inside the softer "Saugus syncline" the stress drop increases rapidly to a maximum of 250 bars for section BB' and 120 bars for section AA'. These high stresses and strains near the surface are very surprising since no aftershocks were observed in the vicinity of the fault scarp. To the best of our knowledge this situation was never reported for past earthquakes and it suggests several possibilities:

(a) An exceptionally high strain energy was actually stored in the Saugus formation where the fault displacements were large because of its geological setting. This hypothesis will be investigated in later studies.

(b) The "Saugus" and the upper layer of materials did not behave elastically during the earthquake and our calculations of stress drop could be misleading. A possible indication of nonelastic behavior is found in Savage et al. (1972) who report 40 cm of afterslip in the days following the main shock. However, this single point measurement is open to question.

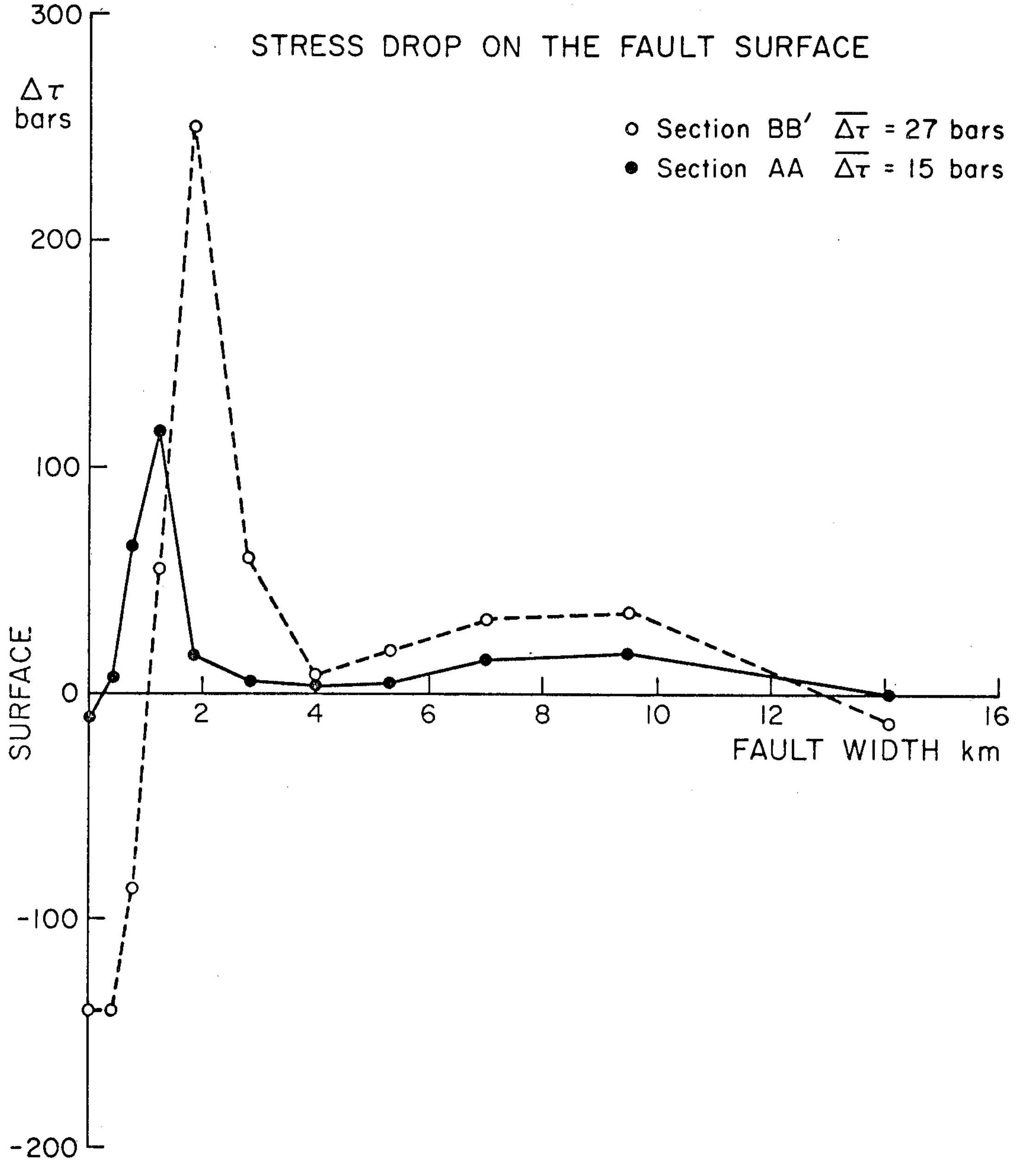

Figure 13. Shear stress drop parallel to the fault surface. The shear stress is averaged on a small region around the fault plane and is an underestimate.

(c) Our model of the earthquake is not sufficiently detailed since it uses one single fault, while field evidence suggests the existence of several breaks near the surface which could extend to significant depths. These secondary faults would give rise to surface displacements which would be misinterpreted in our simpler model so as to lead to a high stress drop.

We can, in fact, consider a multiple fault model based on the available evidence. From the work of Bonilla et al. (1971), we find that near our section BB', in addition to the major Tujunga fault scarp, two small faults with significant vertical offset are found in Lopez Canyon. One is 500 m to the north and dips 65° (Kamb et al., 1971) and the other outcrops 900 m to the north of the main break and dips approximately 60°N. In view of these observations we modeled a three-fault system, and the results are shown in Figure 14.

We used a major fault, marked (1), similar to the single fault used in previous models with a dip of 33°N and an epicenter 13.3 km to the north, the hypocenter at a depth of 8.5 km. Two small faults branch out from the major one as indicated (marked (2) and (3)). In order to fit the observed vertical displacements we had to apply relative offsets dying out linearly towards the surface on the three faults. The strains in the upper 2 km of the crust are not significantly changed in this model since the sum of the relative displacements on all three faults are very similar to the best solution with one fault only.

Two improvements are achieved, however. The horizontal displacement obtained here gives a shortening of 70 cm for the line

THREE FAULTS SYSTEM

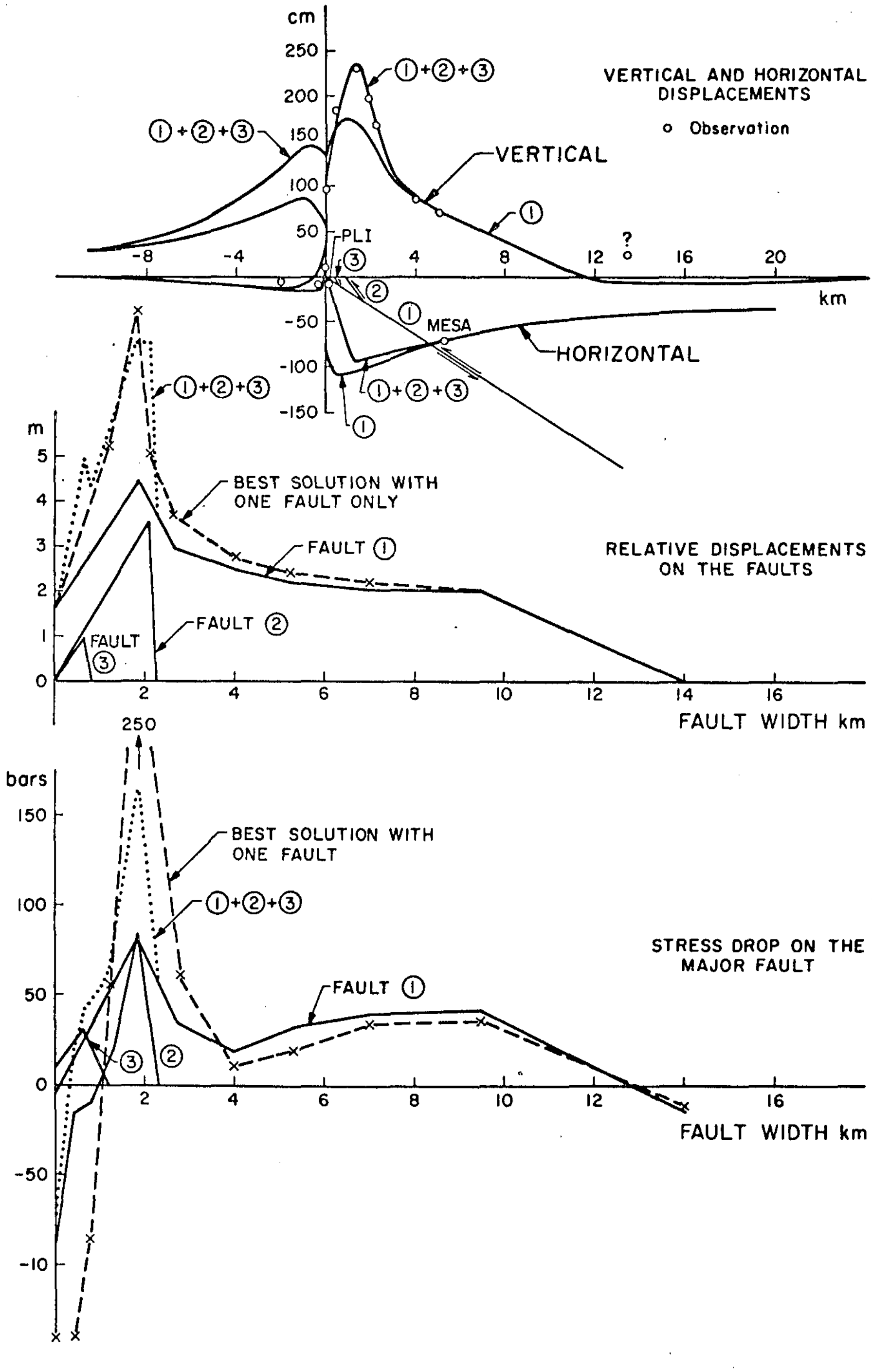

Figure 14. Comparison of displacements on the free surface, offset along the faults and shear stress drop for a single fault and a multiple fault system.

PL1-Mesa instead of a 50 cm lengthening obtained for the single fault model. The other advantage of this model is seen in the stress drop along the fault. In this case, the maximum shear stress drop at 1 km depth is reduced by 30% and the surface loading has almost disappeared. Thus, the preferred conclusion is that in the portion of the fault modeled by section BB', the earthquake is better represented by a major fault surface fingering out into multiple smaller breaks as it approaches the free surface.

How many of these small faults branch off the main plane and how much offset or stress drop can be accounted for by this explanation cannot be asserted without more data than are available to us. We note, however, that the multiple fault hypothesis is an alternative explanation to the plastic deformation suggested above. However, as the number of such small secondary faults becomes large, the distinction between the two is not great.

Source parameters

Based upon the results of this study, it is found that the San Fernando earthquake is best represented by different fault segments. The Sylmar segment has an average length of 4 km (based on the contours of Fig. 7), a width of 14 km and an average offset of 1.12 m. The Tujunga segment has an average length of 6 km, a width of 15.8 km and an average offset of 2.35 m.

The seismic moment is usually defined as

$$M_o = \mu U A \qquad \text{(Brune, 1968)} \qquad (2.1)$$

where U is the average displacement on the fault. In this case, since we have variable shear modulus and slip along the fault, we use

$$M_o = \int_{\text{length}} \int_{\text{hypocenter}}^{\text{surface}} \mu(x)U(x)\, dx\, dy \qquad (2.2)$$

This gives, for every kilometer of fault length

0.35×10^{25} dyne cm for section AA'

and

0.85×10^{25} dyne cm for section BB'

Or, for the entire fault system as defined above

$$M_o = 6.2 \times 10^{25} \text{ dyne cm.}$$

This estimate, based on two-dimensional models, is in agreement with the moment obtained by Wyss and Hanks (1972) from body wave data.

The average shear stress drop was found to be 15 and 27 bars for AA' and BB', respectively. These values are similar to those reported by Wyss and Hanks (1972) on the basis of P and S wave spectra, but the meaning of an average stress drop is unclear in an earthquake where prestress and stress drop may vary by an order of magnitude along the fault. Chapter IV will expand on this subject in a more quantitative way.

Alternative solutions

In our "principal" solution, we chose to have the fault slip increase at a relatively slow rate from the focus up to a depth of 8 km.

This was caused by our decision not to fit the uplift data near the epicenter on the premise that it may reflect secular uplift of the San Gabriel mountains or secondary movement of the San Gabriel fault. It should be noted, however, that the lack of sufficient vertical elevation data in the area immediately north of the epicenter places only weak constraints on fault displacements in the hypocentral region. In fact, because we do not know enough about the subsurface geology and the prestress distribution, the numerical technique does not provide unique solutions at hypocentral depth.

Figure 15 shows several alternative solutions which all fit the epicentral data, while still giving a reasonable fit to the other post-earthquake changes in elevation. These solutions represent a more rapid growth of the fault offset up to a value of 2 m at 10 km depth. As expected, the shear stress drop at the focus strongly reflects how fast the offset grows, and because of the increased moment twisting the end of the fault, the change in principal stress is even more pronounced. Hanks (1972), on the basis of the large rapid changes in ground displacement at Pacoima Dam occurring approximately 2.5 seconds after the Pacoima Dam accelerograph was triggered, suggested that fault displacements in the hypocentral region may have been quite large, perhaps as large as 5 m. While this estimate is subject to some uncertainty, his conclusion that failure initiated in a high strength region and was locally accompanied by large offset and stress drop is worth investigating.

In principle, all the data available could accommodate rather large displacements, up to 5 m, near the hypocenter, providing the

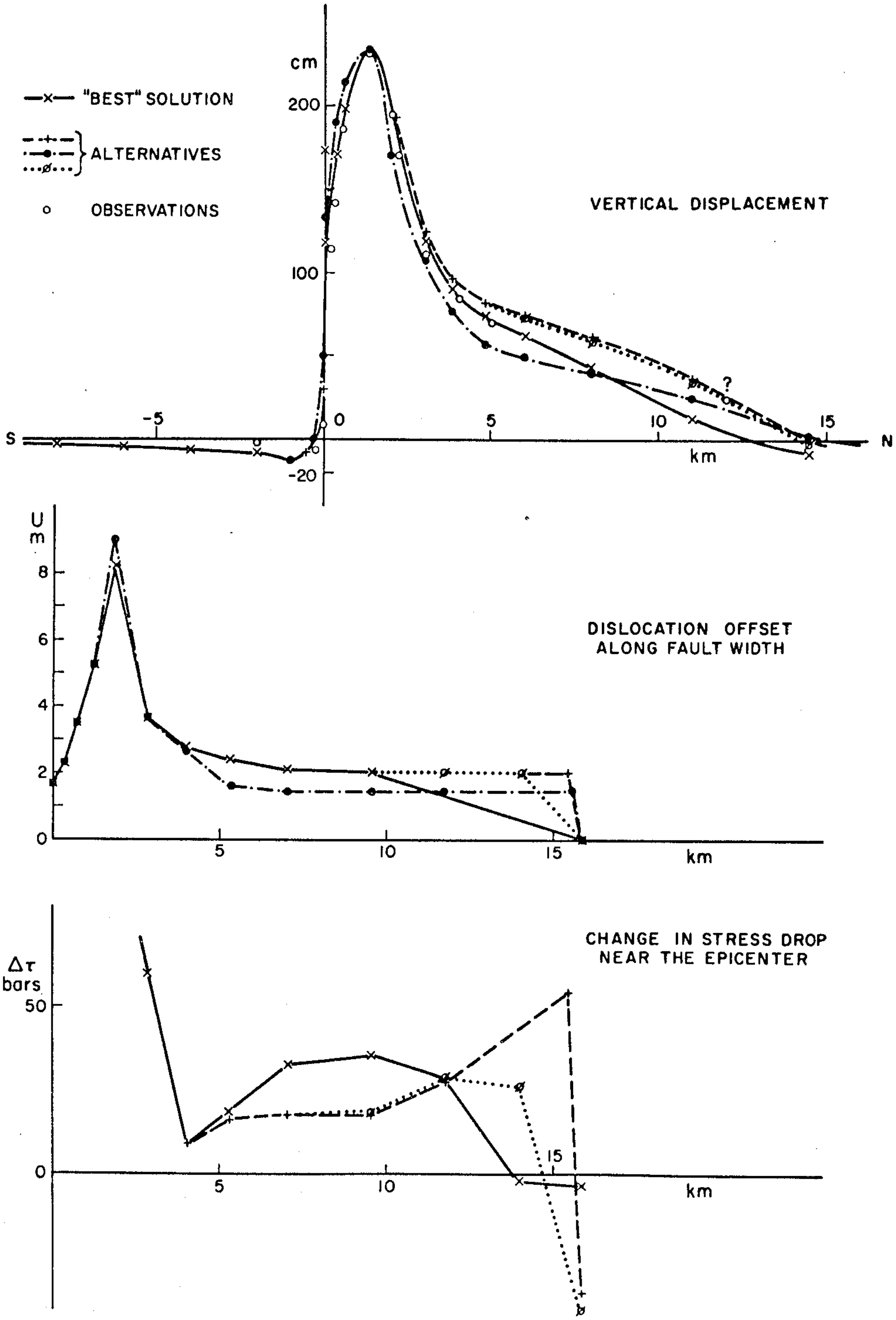

Figure 15. Some alternative "best fit" solutions with more rapid growth of the static offset at the hypocenter. (Section BB')

fault offset is not more than 1 m at 6 km depth and then follows the pattern of our principal solution toward the free surface. The reason for this is seen in Figure 16 where we plotted the vertical uplift caused by dislocations which are initiated at several hypocenter depths with offsets increasing up to a maximum of 5 m before dying out at 6.3 km depth. They represent faults beginning with dips of 33°, 45° and 60°, respectively, giving hypocenters at 8.4, 9.7 and 12.4 km, respectively.

Combining solution (3) of Figure 16 with the results from our principal solution for the upper 6 km of the fault, we obtain the fault geometry, vertical uplift and relative displacements shown in Figure 17. This solution satisfies the estimates of hypocentral displacements of Hanks (1972) as well as the observed static uplift at the free surface.

This unusual solution implies that large strains and stresses were stored in the hypocentral region since the amount of slip and its distribution over the fault surface is controlled for the most part by the prestress environment in which the failure took place. Localized stress concentrations could be caused by past earthquakes or creep at depths greater than the hypocenter or by the presence of a high strength material of small size. Because the fault displacement reduces as the rupture progresses toward the free surface, this implies that the prestress at 6 km depth was well below failure. Such large strain variations can only be the result of local geology. This aspect of slip growth and its implications upon prestress and energy released will be discussed in greater detail in Chapter IV, where this particular solution will be studied at great length.

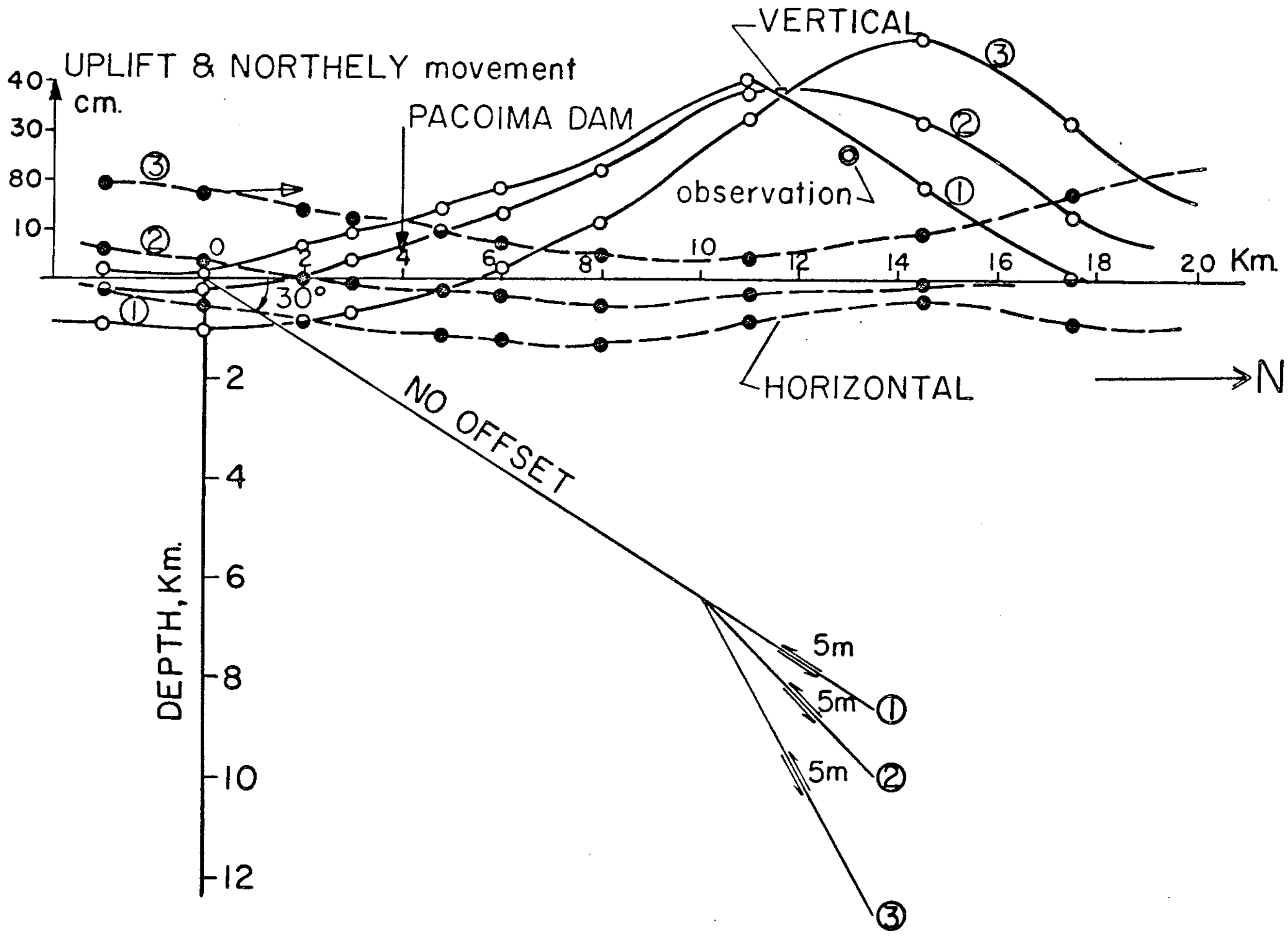

Figure 16. Influence of a large hypocentral offset, with three possible dips of the "fault plane solution".

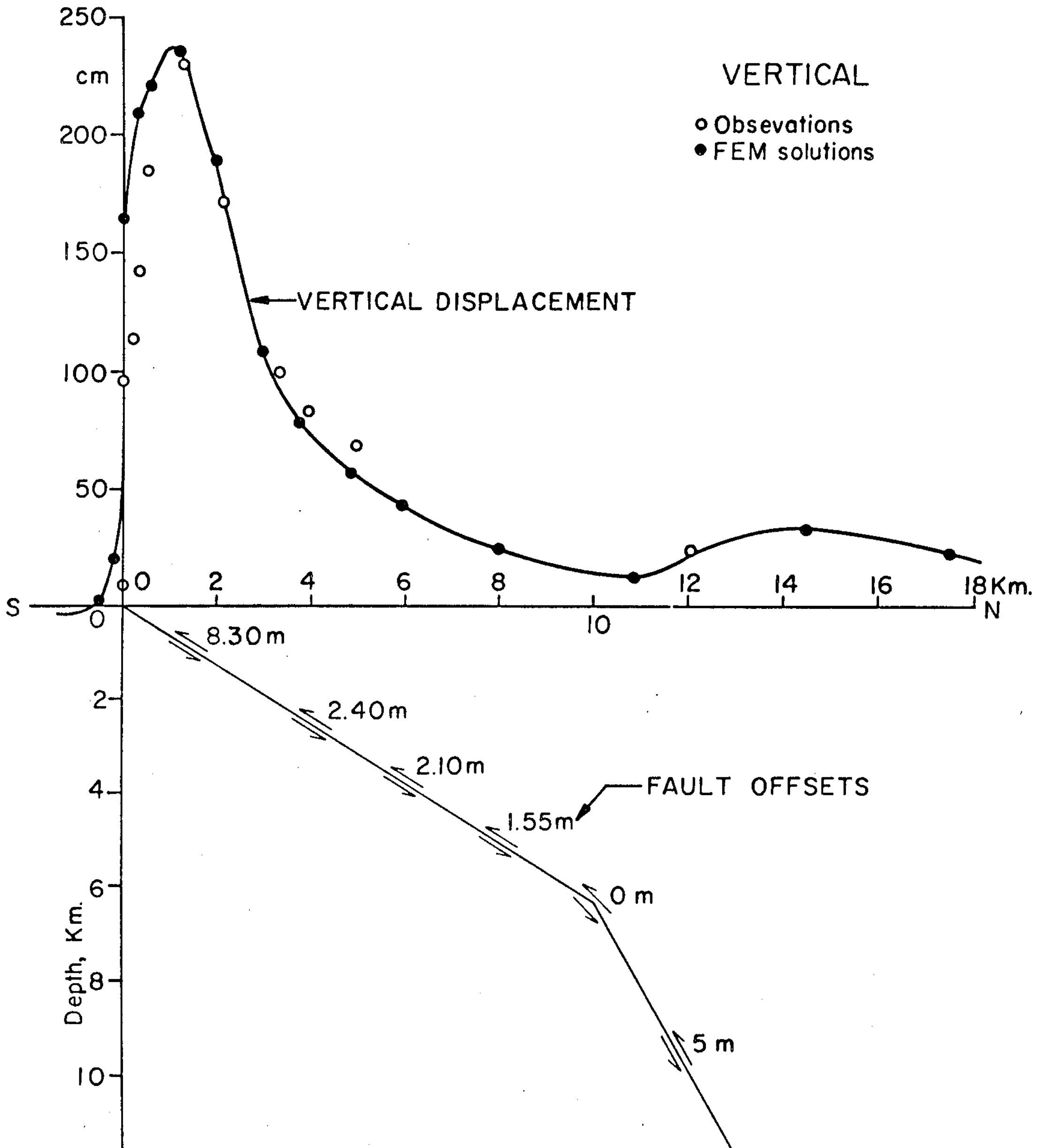

Figure 17. Solution combining a large offset near the hypocenter and the offset of the first solution for BB' near the surface. This will be used for the energy-prestress calculations.

3. The Alaska Earthquake (1964)

The Alaska earthquake of 27 March 1964 was accompanied by vertical tectonic deformation covering an observed area between 170.000 and 200.000 square kilometers (Plafker, 1965). Even though this area is divided about equally between uplift and subsidence, the average amount of uplift is about 6 feet as compared to an average subsidence of less than 2.5 feet (Plafker, 1970). This indicates a very significant increase of local gravitational potential energy caused by this event. Rough estimates by Plafker (1970) give a net increase of 2×10^{26} ergs, or two orders of magnitude greater than the seismic energy radiated ($E_{GR} = 11.4 + 1.5\ M_S \simeq 2 \times 10^{24}$ ergs).

Studies of the focal mechanism of the main shock and its aftershock sequence (Stauder and Bollinger, 1966) indicate that the fault which is 600 km in length and at least 200 km in width is a thrust dipping to the northwest with a dip of only 10 degrees. We will study one cross section of this large fault. We choose section BB' of Plafker (1965, 1970, 1972). This cross section runs southeast-northwest through the southwest tip of Montague Island.

A large left lateral component of displacement was not apparent between the Kodiak Island group and the mainland or in the surface faults on Montague Island (Plafker, 1972). This clearly indicates that for at least 500 km of its length, the Alaska thrust fault is purely dip slip. This allows plane strain modeling with a maximum of confidence in the solutions.

Savage and Hastie (1966) and Stauder and Bollinger (1966) have used the "dislocation" theory described in Chapter II to compare theoretical profiles with the observations. Of necessity idealized to permit a mathematical analysis, their combined models imply a major thrust fault dipping at an angle of 10° with a slip varying from 3 to 18 m. A secondary thrust fault is included (the Patton Bay fault) with a 2.7 m average offset.

The crustal model used is shown in Figure 18. This model is from Plafker (1972), and the elastic properties assigned to the units shown are based on P-wave velocity measurements from Shor (1962) and Hales and Asada (1966). Their velocities are essentially those of typical crustal and upper mantle materials. The observations of vertical displacement (with their uncertainty) along profile BB' are gathered from Plafker (1970). The finite element grid used is 800 km in length and 300 km thick. The grid is shown in Figure 18 as a background to the structure.

In this particular application, in order to obtain a fault offset function consistent with the observed uplift data, we used a stochastic inversion technique.

The inverse problem of determining a relative offset at depth from a set of relative displacements data has been described by Alewine and Jordan (1972). Their numerical technique is a special application of the optimal solution to the linear inverse problem in geophysics (Jordan and Franklin, 1971; Jordan and Minster, 1971). The theory of well-posed stochastics extended to ill-posed linear problems, the

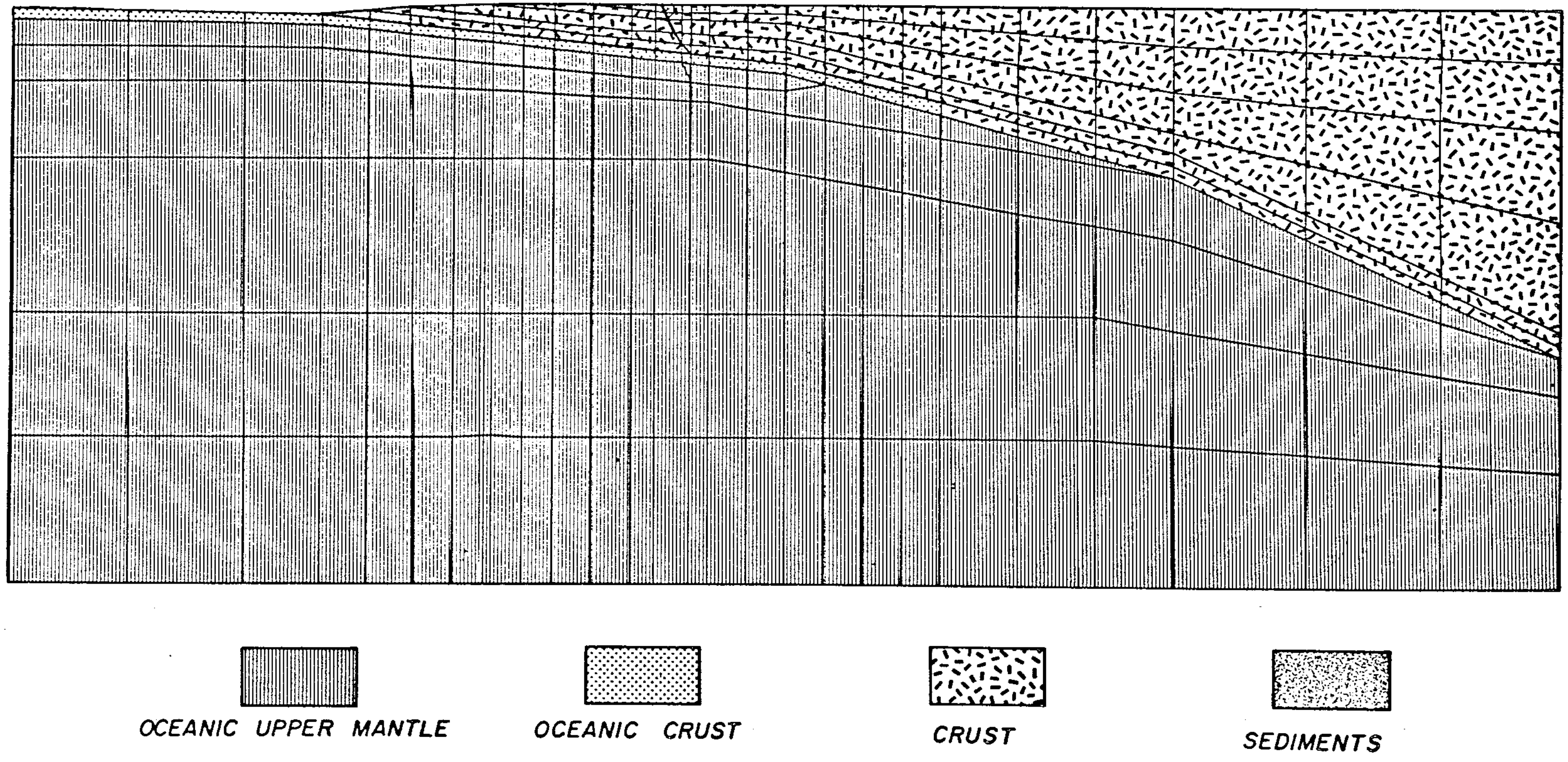

Figure 18. Finite element grid and structural model used for the Alaskan study. The elastic constants used are averaged values similar to those listed in Table 1.

resolving power of finite sets of data and the effective resolution of data sets corrupted by noise has been presented in several recent papers (e.g., Backus and Gilbert, 1970). Thus, we will limit our presentation of the inversion theory in this thesis to a general discussion of the results that can be expected from its application.

In principle, the problem as posed is undetermined. The geology and the tectonic structure of Alaska are not known with accuracy at depth, and as we showed in Chapter I, changes in the geometry of the structural units used in the model result in differences in the inferred fault offsets. In addition, the data (observed surface displacements) are not linearly independent in general, and this adds to the non-uniqueness problem. Lastly, the data are contaminated by noise (uncertainties in the relative measurements), and this has to be taken into account in the resolvability of the solution. However, there exists some valid information concerning the physics of the phenomenon. If one assumes that the crustal model shown on Figure 18, however simplified, is the correct, unique model possible, and if one assumes further that the data are consistent, then one can find a good fit.

These assumptions act as a linear filter which constrain the solution to self-consistency. With these premises, the basic approach is essentially a simple iteration method. From the finite element method, we compute the relative vertical displacement at the free surface caused by a unit offset imposed on each of the nodes which define the fault plane. A linear combination of these computed "unit" uplifts and subsidences gives the total free surface displacements caused by the same combination of unit offsets on the fault. The trial solution is thus a linear summation of unit nodal slips. This trial solution is iterated until the difference between calculated and observed uplifts tends to a lower bound. Since the lower bound is a direct function of the amount of contamination in the data and of their consistency, the final solution is known only up to an arbitrary vector in the null space (Jordan and Minster, 1971). The final solution is, however, the best fit to the data available in the framework of the tectonic model chosen.

The calculated fault offset

Figure 19 shows the observed vertical offset along the surface of the cross section. The error bars are assumed to be ±25 cm from Plafker (1970). The rapid growth of the uplift near Montague Island can be attributed to the Patton Bay fault. The subsidence inland and the general uplift from the shore towards the ocean can be attributed to the megathrust. The best solution for the offset of the megathrust is shown at the bottom of the figure. It follows the pattern of the solution presented by Stauder and Bollinger (1966), but it differs from theirs in some major details.

Our maximum offset is 33 m , and the solution requires an offset of nearly 17 m below Middleton Island. The computed vertical surface motion is plotted with the observations, and we believe the fit to be self-consistent. In order to fit the sharp uplift observed at Montague Island, the offset on the Patton Bay fault is an average of 4 m with a maximum of 7 m at mid depth. The local minimum in the

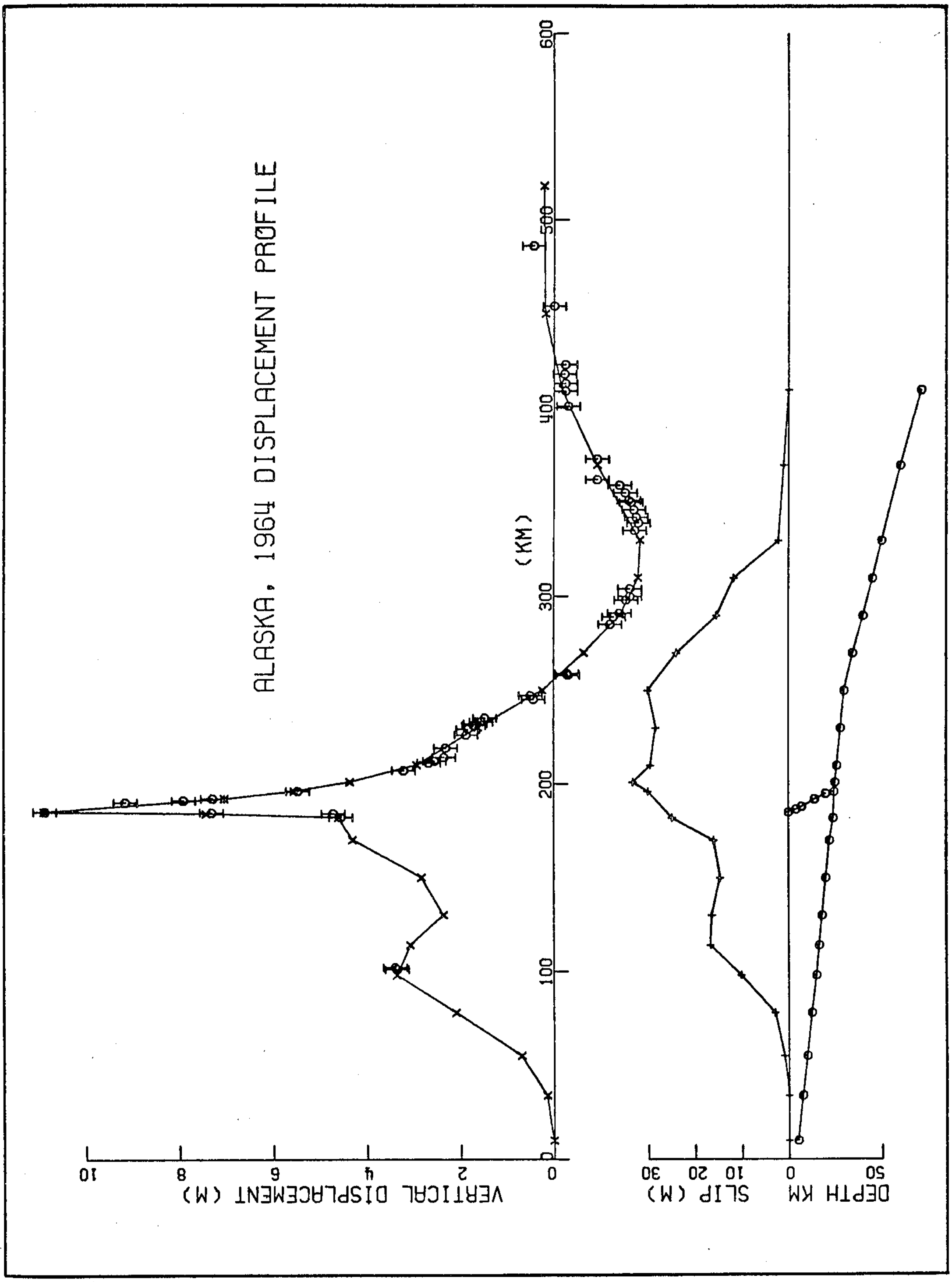

Figure 19. Observed and calculated surface movement for the Alaska earthquake. The "best fit" solution is shown in the lower portion of the figure.

calculated uplift between the two islands is obviously not unique since no data exist in that region. This is discussed later in the section on resolvability.

Figure 20 shows a comparison between the observed and the computed horizontal surface motion. Although these data were not included in the inversion, the fit is remarkable. For the sake of comparison, we adjusted the calculated horizontal surface motions to the zero isobase of the observations (Station Fishhook and Station Klawasi, Plafker (1970)). The calculated motion of the intersection of this isobase with our cross section is actually 4 m. The data that differ the most from the calculated motion are the most uncertain (Plafker, 1970).

We can thus feel confident that the fault offset function resulting from the inversion is the best fit to both the vertical and horizontal surface motion data.

Figure 21 shows a contour plot of horizontal (x direction) and vertical (y direction) relative displacements throughout the cross section studied. It shows that because of the free surface, most of the displacement field is partitioned to the left and above the fault plane. The presence of the Patton Bay fault is clearly visible on the vertical displacement plot. The interpretation is that for this earthquake, the Alaskan continent overrode the Pacific Plate.

Resolvability

Since the data contain some noise, there exist model perturbations of our "best fit" model which still fit the observed surface movements to

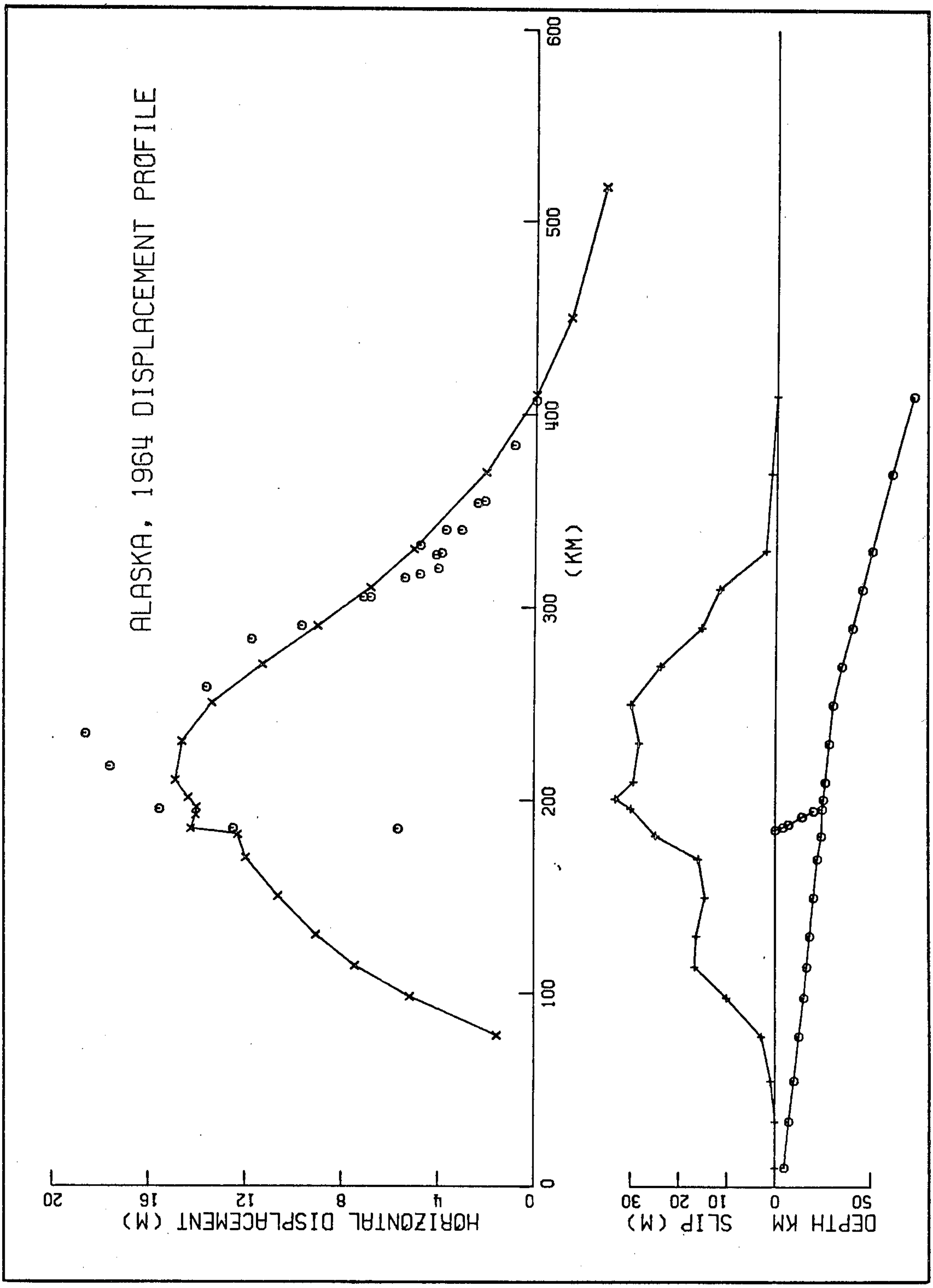

Figure 20. Observed and calculated horizontal movements for the Alaska earthquake, 1964.

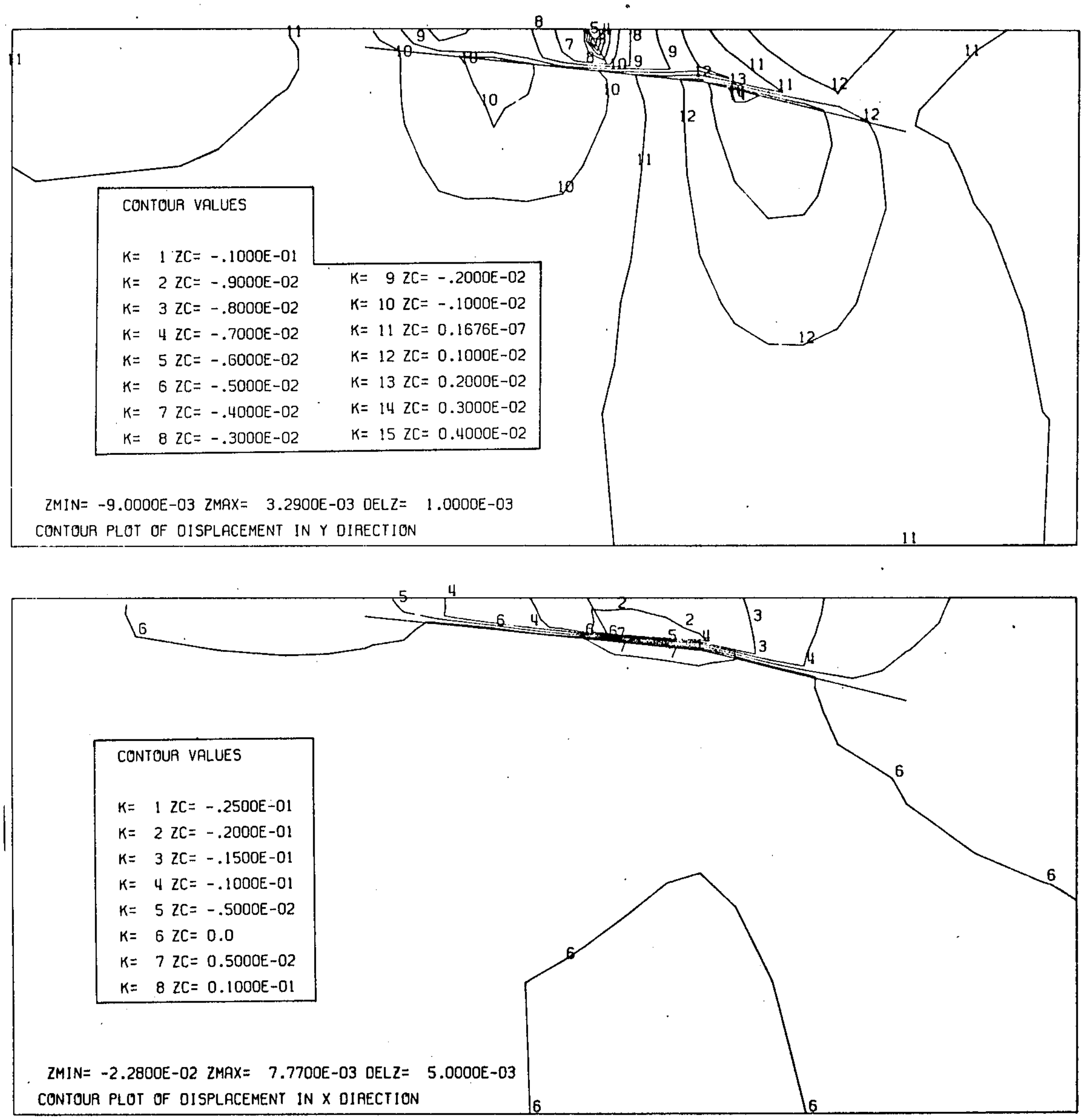

CONTOUR VALUES

K= 1 ZC= -.1000E-01
K= 2 ZC= -.9000E-02
K= 3 ZC= -.8000E-02
K= 4 ZC= -.7000E-02
K= 5 ZC= -.6000E-02
K= 6 ZC= -.5000E-02
K= 7 ZC= -.4000E-02
K= 8 ZC= -.3000E-02
K= 9 ZC= -.2000E-02
K= 10 ZC= -.1000E-02
K= 11 ZC= 0.1676E-07
K= 12 ZC= 0.1000E-02
K= 13 ZC= 0.2000E-02
K= 14 ZC= 0.3000E-02
K= 15 ZC= 0.4000E-02

ZMIN= -9.0000E-03 ZMAX= 3.2900E-03 DELZ= 1.0000E-03
CONTOUR PLOT OF DISPLACEMENT IN Y DIRECTION

CONTOUR VALUES

K= 1 ZC= -.2500E-01
K= 2 ZC= -.2000E-01
K= 3 ZC= -.1500E-01
K= 4 ZC= -.1000E-01
K= 5 ZC= -.5000E-02
K= 6 ZC= 0.0
K= 7 ZC= 0.5000E-02
K= 8 ZC= 0.1000E-01

ZMIN= -2.2800E-02 ZMAX= 7.7700E-03 DELZ= 5.0000E-03
CONTOUR PLOT OF DISPLACEMENT IN X DIRECTION

Figure 21. Contour plots of relative displacements of the "best fit" solution through the cross section. Contour values have units of kilometer.

some close degree of confidence. If we can estimate the errors in the data, then it is possible to relate them to errors in the solution.

Such a relation between the data space and the model space exists in the form of a variance operator which has been described in detail by Jordan (1972). It is to be noted that this operator V is independent of the final "best fit" solution. Jordan showed that, as a result, one can perturb a model by an amount $\underline{\delta m}$ and still fit the data to within some confidence limit, say 95%, provided that

$$\underline{\delta m}\ V^t\ \underline{\delta m}\ > K^2(c)$$

where K(c) is the factor associated with the confidence coefficient (here for 95%, K(c) = 1.96).

In this study, we chose a particular perturbation to our best fit model, a perturbation which we considered to be physically interesting, and checked this perturbation for the 95% resolvability criterion. If the perturbation was resolvable to a confidence interval greater than 95%, it was reduced in size until the resolvability was within that range.

The results are shown in Figure 22 where the final perturbations are shown as stippled areas. They represent for each case the maximum amount of slip that could be added at that particular node and still give a fit to the data with a resolvability within the 95% confidence level. This means that any solution between our "best fit" and its maximum permitted perturbation would satisfy the data used in the inversion.

As is seen from the figure, the growth of the fault offset from the hypocenter to the maximum of 30 m is very resolvable. This is

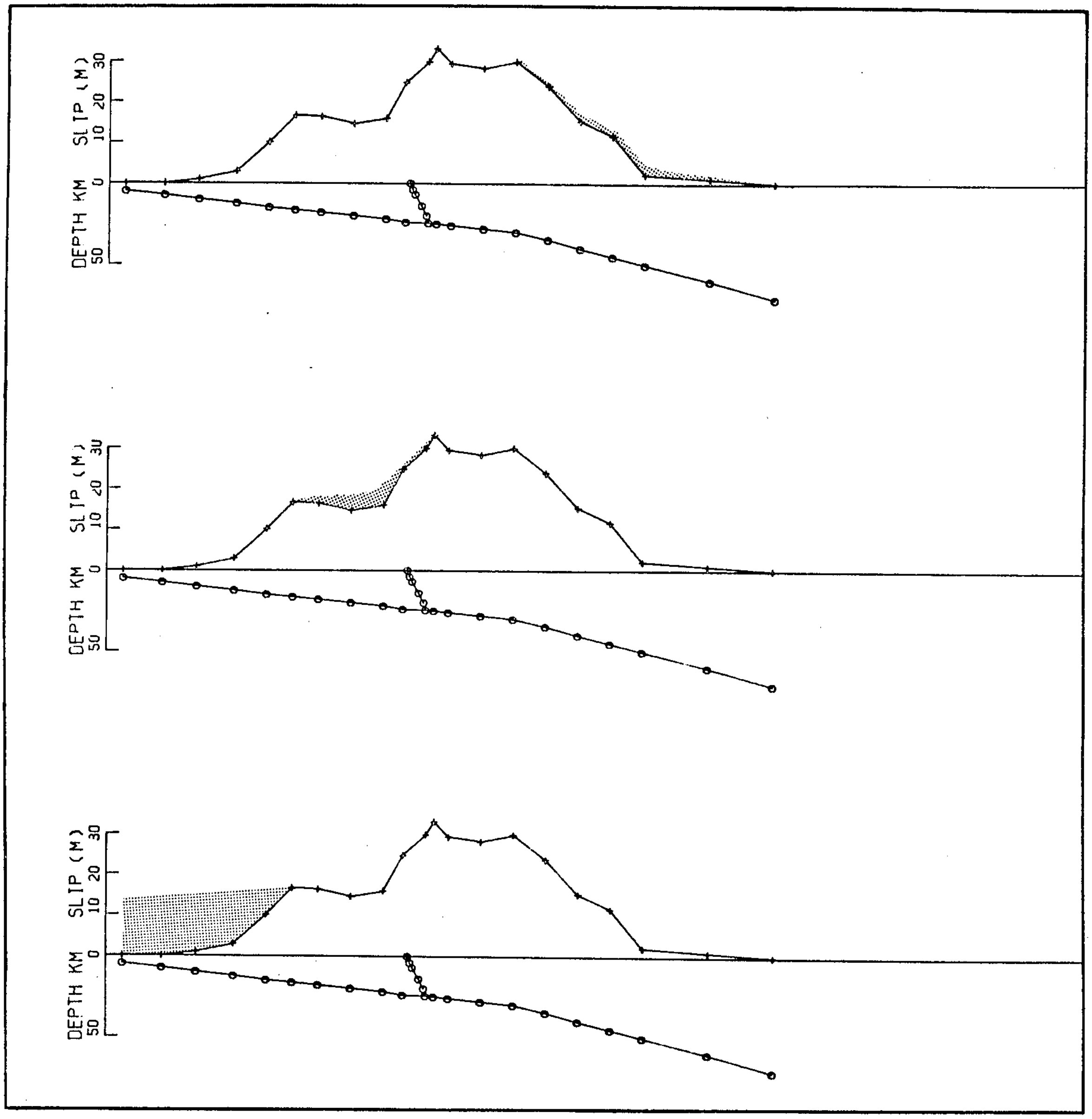

Figure 22. Resolvability of the best fit solution. The perturbation shown in shaded areas still fits the data within a 95% confidence.

due mainly to the fact that there is a dense network of data points just above these nodes. The local minimum in the offset southwest of Montague Island is less resolvable. The slip in that portion of the fault could be increased by as much as 4 m and the calculated surface displacements would still be within the error bars of the observations. The behavior of the fault near its surface expression is almost totally unresolvable by the data used. This upper portion of the megathrust was below the ocean floor and the only observation available to us for that region was from Middleton Island.

Conclusions

The results presented here represent the best possible solution for the Alaska earthquake static relative displacements. The fault offsets are at least 50% greater than those calculated by past researchers and their variation along the fault surface are proportionally as important as those reported for the San Fernando earthquake.

If we compute the average moment of the megathrust, we get

$$\begin{aligned} M_o &= \mu UA \\ &= 3.1\text{x}10^{11} \text{ x } 6\text{x}10^{7} \text{x } 2.6\text{x}10^{7} \text{x } 18.5\text{x}10^{2} \\ &= .9\text{x}10^{30} \text{ dyne cm.} \end{aligned}$$

From long period surface waves, Kanamori (1970) gives

$$M_L = .75\text{x}10^{30} \text{dyne cm}$$

In view of the large differences in the time scale and the method, the agreement is very good. The stress drop and strain energy released for this event will be presented in Chapter IV.

III. THEORY OF ENERGY RELEASED IN SHALLOW EARTHQUAKES AND ITS NUMERICAL APPLICATION

Introduction

In recent years, the techniques of elastostatics have been applied with various degrees of success to earthquake modeling. By comparing the medium in its final state with the state that existed prior to failure, one need not consider details of the transient effects associated with the initiation and propagation of the crack when dealing with the energetics of the phenomenon.

By simple considerations of static elasticity, one can study failure as a limit situation which compares states of prestress with various failure criteria. This allows comparisons between laboratory experiments and realistic geological environments in terms of qualitative stress levels relevant to the fracture hypothesis of earthquakes (Mogi, 1972).

The "dislocation" theory which computes stress change and relative displacement fields caused by a "fault offset" in an infinite half space is another static approach (Maruyama, 1964; Steketee, 1958). This approach has had some degree of success in determining average stress drop from fault offsets obtained from the limited observed permanent deformation (when available). This theory has, so far, been successful only in determining special prestress field or energy balance because it either starts from an unstressed medium into which a fault offset is forced or because it assumes that the final state is characterized by complete stress relaxation on the fault surface (Smith and van de Lindt, 1969). More general dislocation theory was developed to deal with partial stress drop (e.g., Savage and Wood, 1971). Particular energy formulations have been developed for specialized cases of stress dislocations with partial stress drops (Burridge and Knopoff, 1966).

From these developments and others, empirical and special purpose theoretical formulae have been derived, relating earthquake parameters such as fault area, fault offset, energy released and stress drop. These results appear to compare with those obtained from seismology, but this apparent agreement may be deceptive since both techniques involve order of magnitude uncertainties. Brune (1970) and Hanks and Wyss (1972) discuss source parameters such as moment and stress drop from analysis of frequency spectra in terms of empirical formulae linking the source to the far field observations. Thus, both static dislocation theory and spectral analysis of seismic waves deal exclusively with average features of the fault.

These oversimplified approaches may be misleading if the results they give are used to analyze the failure of the hypocentral region, in terms of strength of materials obtained in laboratory experiments. In particular, we have shown, in Chapter II of this thesis, that order of magnitude variations of stress drop and offset along the fault plane give the best fit to the data for the San Fernando and Alaska earthquakes. As we will show in Chapter IV, these variations lead to a very different view of the earthquake mechanism than the one inferred from teleseismic observations (e.g., Hanks and Wyss, 1972). Clearly, then, a theory which takes these spatial variations of stress into account is needed in order to refine our understanding of such important processes as failure initiation, stress readjustment and energy balance.

The "stress relaxation" theory of Archambeau, (1964, 1968, 1970) which describes the change in the stress field due to the creation of the rupture zone within it, can be used to compare final and initial static states. This leads to a general formulation of energy release valid for arbitrary fault parameters in a geologic environment. These static formulae can be numerically simulated using the finite element method, which in this study has been limited to two-dimensional plane strain. This method, when applied to failure in a complex prestress situation allows direct calculations of the change in strain energy, stress drop and gravitational potential.

Energy Formulation

Most of the basic ideas involved in the following theoretical development have been discussed previously in Press and Archambeau (1962), Archambeau (1968, 1972) and Archambeau and Sammis (1970). Since their formulation was specialized to the analysis of nuclear explosions, we will briefly review their calculations, with some important differences, best suited for our present purpose.

We will restrict ourselves to the field of linear elasticity since it is appropriate to assume that the nonlinear processes involved in the failure are restricted to a small volume "inside" the fault plane. They can be seen to contribute to the energy involved in the failure process (e.g., heat losses) and not to the tectonic energy radiated which is our concern here.

Following Archambeau (1972), we assume the medium to be initially stressed and in static equilibrium. Let a zero subscript denote this equilibrium field inside an arbitrary prestressed medium of volume V with fixed boundaries S (= $S_u + S_\tau$). With $\vec{f}$ denoting all the static forces in the medium, we have

$$\frac{\partial \sigma_{ij}^{(0)}}{\partial x_j} + f_i = 0 \tag{3.1}$$

with boundary conditions

$$\left[\sigma_{ij}^{(0)} n_j\right] = 0 \text{ on } S_\tau$$

$$\left[u_i^{(0)}\right] = 0 \text{ on } S_u$$

Let a (1) superscript denote the equilibrium field after the introduction of a new boundary within the medium. In this development the new boundary is the surface enclosing the fracture zone created by the earthquake (volume V_o, surface ∂V_o enclosing the fracture).

The final stress state is $\sigma_{ij}^{(1)}$ and is to first order

$$\frac{\partial \sigma_{ij}^{(1)}}{\partial x_j} + f_i = 0 \tag{3.2}$$

with the boundary conditions

$$\left[\sigma_{ij}^{(1)} n_j\right] = 0 \text{ on } S_\tau \text{ and } \partial V_o$$

$$\left[u_i^{(1)}\right] = 0 \text{ on } S_u$$

In view of the identical form of (3.1) and (3.2), we can substract them and obtain an equation involving the stress change caused by the failure

$$\delta \tau_{ij} = \sigma_{ij}^{(0)} - \sigma_{ij}^{(1)} \tag{3.3}$$

and we get, to first order

$$\frac{\partial}{\partial x_j} (\delta \tau_{ij}) = 0 \tag{3.4}$$

In addition at large distances from ∂V_o the stress change vanishes (Archambeau, 1972).

The strain energy density is $1/2\, \sigma_{ij}^{(0)} \epsilon_{ij}^{(0)}$ initially and in the final equilibrium state it is $1/2\, \sigma_{ij}^{(1)} \epsilon_{ij}^{(1)}$ where $\epsilon_{ij}^{(0)}$ and $\epsilon_{ij}^{(1)}$ are the strains associated with each equilibrium state. Thus the change in the strain energy of the medium is

$$\delta W = \frac{1}{2} \int_V \left\{ \sigma_{ij}^{(0)} \epsilon_{ij}^{(0)} - \sigma_{ij}^{(1)} \epsilon_{ij}^{(1)} \right\} dV \tag{3.5}$$

where $V = V_o + V_1$. Let V_k with $k = 0,1$ represent V_o and V_1. Then

$$\delta W = \delta W_1 + \delta W_0 \tag{3.6}$$

and we have

$$\delta W_1 = \frac{1}{2} \int_{V_1} \left(\sigma_{ij}^{(0)} - \sigma_{ij}^{(1)} \right) \left(\epsilon_{ij}^{(0)} - \epsilon_{ij}^{(1)} \right) dV$$

$$- \int_{V_1} \left\{ \sigma_{ij}^{(1)} \epsilon_{ij}^{(1)} - \frac{\sigma_{ij}^{(1)} \epsilon_{ij}^{(0)}}{2} - \frac{\sigma_{ij}^{(0)} \epsilon_{ij}^{(1)}}{2} \right\} dV \tag{3.7}$$

But in the volume V_1, the stress strain constitutive relationship has not changed between the two equilibrium states. Then

$$\sigma_{ij}^{(0)} \epsilon_{ij}^{(1)} = E_{ijkl}\, \epsilon_{ij}^{(0)} \epsilon_{ij}^{(1)} = \epsilon_{ij}^{(0)} \sigma_{ij}^{(1)} \tag{3.8}$$

Hence

$$\delta W_1 = \frac{1}{2} \int_{V_1} \delta \tau_{ij} \, \delta \epsilon_{ij} dV + \int_{V_1} \sigma_{ij}^{(1)} \, \delta \epsilon_{ij} dV \qquad (3.9)$$

or

$$\delta W_1 = \int_{V_1} \sigma_{ij}^{(0)} \, \delta \epsilon_{ij} \, dV - \frac{1}{2} \int_{V_1} \delta \, \tau_{ij} \, \delta \epsilon_{ij} \, dV \qquad (3.10)$$

Now, since $\epsilon_{ij} = \frac{\partial ui}{\partial x_j}$

and

$$\sigma_{ij} \, \epsilon_{ij} = \frac{\partial}{\partial x_j} (\sigma_{ij} u_i) - \frac{\partial \sigma ij}{\partial x_j} u_i$$

we have after applying Gauss's theorem to Eq. (3.10)

$$\delta W_1 = \oint_{S+\partial V_o} \langle \sigma_{ij} \rangle \delta u_i n_j \, ds - \int_{V_1} \frac{\partial \langle \sigma ij \rangle}{\partial \, x_j} \delta u_i \, dV \qquad (3.11)$$

where

$$\langle \sigma_{ij} \rangle = \frac{\sigma_{ij}^{(0)} + \sigma_{ij}^{(1)}}{2} = \sigma_{ij}^{(0)} - \frac{\delta \tau ij}{2}$$

From Eqs. (3.1) and (3.2), we have

$$\frac{\partial \langle \sigma ij \rangle}{\partial x_j} = -f_i \qquad (3.12)$$

Now, we can assume in this particular development that the failure along the fault plane is such that ∂V_o is constituted of two surfaces Σ of equal area. Σ^+ defines the surface on one side of the fault where $\delta u_i = \delta u_i^+$ and Σ^- the other side of the fault where $\delta u_i = \delta u_i^-$. To first order, $\Sigma^+ = \Sigma^- =$ fault area $= 1/2 \, \partial V_o$. Define Δu_i as the fault offset. With $\Delta u_i = \delta u_i^+ - \delta u_i^-$, we get

$$\delta W_1 = \oint_S \langle \sigma_{ij} \rangle \delta u_i n_j \, ds + \int_\Sigma \langle \sigma_{ij} \rangle \Delta u_i n_j \, ds + \int_{V_1} f_i \delta u_i \, dV \tag{3.13}$$

The second strain energy change term δW_o can be neglected here, on the ground that the volume of material inside the fault plane is infinitely small and any energy contained in δW_o will be taken up in the irreversible processes of failure. It will not contribute to the radiated elastic energy.

The total strain energy change is then given by Eq. (3.13) and $\delta W \simeq \delta W_1$. In Eq. (3.13), the first term vanishes if the integration is carried over the volume of the earth, that is, if we take S to be a free surface in which case $\langle \sigma_{ij} \rangle n_j = 0$ on S.

If, however, we choose to analyze the energy balance of some arbitrary finite region around the source as the limits of V_1, we can follow Archambeau (1972) and replace the volume outside V_1 by surface tractions, such that

$$\langle \sigma_{ij} \rangle n_j = f_i^{(t)} \quad \text{on S}$$

or if S is far enough from Σ

$$\sigma_{ij}^{(0)} n_j = \sigma_{ij}^{(1)} n_j = f_i^{(t)} \quad \text{on S}$$

Thus these tractions can be regarded as the origin of prestress inside the medium. Hence the integral over S becomes

$$\oint_S \langle \sigma_{ij} \rangle \delta u_i n_j \, ds = \int_S f_i^{(t)} \, \delta u_i \, dS$$

Now define a force F_i to be the sum of the body forces and the forces of tectonic origin by

$$F_i = f_i + f_i^{(t)} \delta(\underline{r} - \underline{r}_s)$$

where r_s is a vector to the surface S and $\delta(\underline{r} - \underline{r}_s)$ is a Dirac delta function, then we have

$$\delta W = \int_{\Sigma} < \sigma_{ij} > \Delta u_i n_j \, ds + \int_{V_1} F_i \, \delta u_i \, dV \tag{3.14}$$

F_i is then the sum of body and "tectonic" forces. The only body force of importance in the earth's crust is gravity, and the "tectonic" forces have only a second order effect on δW if the boundary is far enough from the source.

This is easily proved by looking at the displacement field that results from the Green's function solution of dislocation theory. Press and Archambeau (1962) showed that the relative displacement field behaves with distance from the fault like

$$\delta u_i \sim (1/_r \beta) \qquad \text{with } \beta \geq 2$$

In the numerical models that we will treat, the boundaries were placed far enough from the source so that the solution did not change whether we used a zero displacement, no traction or mixed boundary condition.

In this framework, then, the last term of (3.14) can be considered as the change of gravitational potential energy inside V_1 and the surface integral. Stacey (1968) showed that on a global scale, static considerations lead to a balancing of gravitational potential energy, on the ground that the center of mass of the earth cannot be moved by an earthquake. Although this is open to considerable debate, we are concerned here with the energy balance in the immediate vicinity of an earthquake. Readjustments of gravitational potential on a worldwide basis have no bearing on the local situation. This stems from the time scale involved in the processes. Ben Menahem and Israel (1970) postulate that mass readjustments occur on a time scale of several days through free oscillations. Thus, the local change of gravitational potential energy computed in the last term of Eq. (3.14) has to be considered in calculations of radiated seismic energy. Let Eq. (3.14) be rewritten as

$$\delta W = \int_{\Sigma} \sigma_{ij}^{(0)} \Delta u_i n_j \, ds - \frac{1}{2}\int_{\Sigma} \Delta \sigma_{ij} \, \Delta u_i n_j \, ds + \int_V F_i \delta u_i \, dV \qquad (3.15)$$

where $\Delta \sigma_{ij} = \sigma_{ij}^{(0)} - \sigma_{ij}^{(1)}$ on Σ

This equation, although involving static variables, can be interpreted as the energy released in the radiation field. Since the region outside the fracture zone is elastic, the only means of balancing the strain energy change inside of V_1 is through dynamic redistribution of the energy throughout the medium. As a result of these considerations, Eq. (3.15) represents the upper bound of the radiated energy. Thus

$$\frac{E_R}{\eta} = \delta W = \int_{\Sigma} \sigma_{ij}^{(0)} \, \Delta u_i n_j \, ds - \frac{1}{2}\int_{\Sigma} \Delta \sigma_{ij} \, \Delta u_i n_j \, ds + \int_V F_i \delta u_i \, dV$$

where η is the seismic efficiency factor, function of interaction between the seismic waves and the rupture zone.

Let an amplitude factor of prestress be defined as

$$\langle \sigma^{(0)} \rangle = \left[\frac{1}{V} \left(\int_V \sigma_{ij}^{(0)} \sigma_{ij}^{(0)} \, dV \right) \right]^{1/2} \qquad (3.16)$$

and an amplitude of offset of the fault defined as

$$\langle U \rangle = \left[\frac{1}{\int_\Sigma d\Sigma} \left(\int_\Sigma \Delta u_i \, \Delta u_i \, d\Sigma \right) \right]^{1/2} \tag{3.17}$$

Then, the spatial distribution of the prestress field can be expressed by a product of the amplitude factor and a prestress field of unit amplitude $S_{ij}^{(0)}$ function of the geology, so that

$$\sigma_{ij}^{(0)} = \langle \sigma^{(0)} \rangle S_{ij}^{(0)} \tag{3.18}$$

Similarly, fault induced stress changes and relative displacement fields can be expressed in terms of products of the fault offset amplitude factor and fields of unit amplitude

$$\begin{aligned} \Delta \sigma_{ij} &= \langle U \rangle \left\{ \frac{1}{2} \mu_{ij} \left[\frac{\partial}{\partial x_j} \frac{u_i}{\langle U \rangle} + \frac{\partial}{\partial x_i} \frac{u_j}{\langle U \rangle} \right] \right\} \quad \text{on } \Sigma \\ &= \langle U \rangle \Delta A_{ij} \\ \delta u_i &= \langle U \rangle \delta B_i \\ \Delta u_i &= \langle U \rangle \Delta C_i \end{aligned}$$

Then, the energy change can be written as

$$\begin{aligned} \delta W = {} & \langle \sigma^{(0)} \rangle \langle U \rangle \int_\Sigma S_{ij}^{(0)} \Delta C_i n_j \, d\Sigma \\ & - \frac{1}{2} \langle U \rangle^2 \int_\Sigma \Delta A_{ij} \Delta C_i \, n_j \, d\Sigma + \langle U \rangle \int_V F_i \delta B_i \, dV \end{aligned} \tag{3.19}$$

If a particular model (i.e., fixed geology and fault area) is accepted and a particular solution is obtained, then each of the fields of unit amplitude are fixed. As a result, Eq. (3.19) can be seen as a quadratic function of the average fault offset amplitude $\langle U \rangle$ or as a linear function of the prestress amplitude $\langle \sigma^{(0)} \rangle$. This leads to a rather simple technique to obtain bounds on the prestress amplitude. A first step consists of inverting the free surface displacements in order to obtain the distribution of fault offset with depth. This allows direct computation of the surface and volume integrals of ΔA_{ij}, ΔC_i, $\delta B_i, \in \Sigma$ or V. Then by varying the amplitude of the prestress field, we can map the linear variation of δW as a function of $\langle \sigma^{(0)} \rangle$. $S_{ij}^{(0)}$ is determined by the model chosen. Comparison of δW with the seismic energy radiated leads to estimates of $\langle \sigma^{(0)} \rangle$ as a function of the seismic efficiency. In the next chapter we will show how to use this technique for several earthquakes.

Note that if the averaging assumptions discussed in the introduction are applied here, together with the neglect of body forces, we get

$$\begin{aligned} E &= \langle \sigma^{(0)} \rangle \langle U \rangle A - 1/2 \Delta\sigma \langle u \rangle A \\ &= \langle \sigma \rangle \langle u \rangle A \end{aligned}$$

where A is the fault area. This is the expression used by Brune and co-workers (Brune, 1968). Note also that Archambeau's (1968) formula

$$E_R = \frac{\eta}{2} \int_{V_1} \Delta \tau_{ij} \Delta \epsilon_{ij} \, dV \tag{3.20}$$

is a special case of Eq. (3.16) for which body forces are assumed to have higher order effects and $\Delta \tau_{ij} = \sigma_{ij}^{(0)} \in \Sigma$, i.e., complete stress release on the fault surface.

Numerical Finite Element Approach

The applicability of finite element techniques in geological applications has been demonstrated in Chapter II. The numerical programs developed can be used to model "dislocations" in a heterogeneous medium. The force of gravity can be introduced in all the computer calculations by assigning a weight density for each of the materials used in the problem description. These appear in the equations of motion or equilibrium as body forces. Similarly, the boundary conditions

$$\sigma_{ij}n_j = 0 \qquad \text{on } S_\tau$$

and (3.21)

$$\delta u_i = 0 \qquad \text{on } S_u$$

are introduced by locking the nodes on the outer boundary (S_u) and by leaving free that portion of the boundary which describes the surface of the earth (or by introducing mixed boundary conditions). Since we are interested here in the change of potential energy caused by the introduction of an earthquake fault (or failure zone), two static models are computed.

A first computation is made with the medium in its initial state. We impose a prestress field composed of the nonhydrostatic component of body forces, specified displacements at the boundaries and past earthquakes (or creep at depth) representing past stress history of the geological environment. The strain energy and the gravitational potential energy are computed as

$$W^{(0)} = \frac{1}{2}\sum_e \sigma_{ij}^{(0)e}\,\epsilon_{ij}^{(0)e}\,V^e \qquad (3.22)$$

$$P^{(0)} = \sum_e F_i^e u_i^{(0)e}\,V^e\;.$$

A second static equilibrium calculation is made on the final state represented by the same specified boundary displacements into which a rupture is introduced. This is done either by dislocation of a row of nodes as described in Chapter I or by relaxing a row of elements (i.e., giving them elastic properties characterized by a low modulus of shear and a Poisson's ratio approaching 0.5, either uniformly in the element or heterogeneously with a set of elastic coefficients). This gives

$$W^{(1)} = \frac{1}{2}\sum_e \sigma_{ij}^{(1)e} \, \epsilon_{ij}^{(1)e} \, V^e$$

$$P^{(1)} = \frac{1}{2}\sum_e F_i^e \, u_i^{(1)e} \, V^e \tag{3.23}$$

The difference between the two states gives

$$\delta W = W^{(0)} - W^{(1)} = \int_\Sigma \langle \sigma_{ij} \rangle \Delta u_i n_j \, d\Sigma + \delta P$$

where δW is the upper bound on radiated energy and $\delta W - \delta P$ gives a direct estimate of energy released by the fault.

For the purpose of simplicity, we studied systematically a fault of infinite length, imbedded in a full space composed of a homogeneous Poisson's solid ($\nu = 0.25$, $\mu = 3 \times 10^{11}$ dyne cm). The finite element grid used is a square grid with sides equivalent to ten fault lengths. This was judged to allow the use as boundary condition of

$$\delta u_i = 0 \qquad \text{on } S_u$$

so that locking the nodes on the sides would not affect the solution adversely. The medium is prestressed in pure shear by specifying displacements on the boundaries. Figure 23 shows a contour plot of shear stress change generated by complete stress relaxation in a 200 bar prestress.

This is a mirror image of similar plots given by Chinnery (1963) or Smith and van de Lindt (1969). The same thing can be obtained by

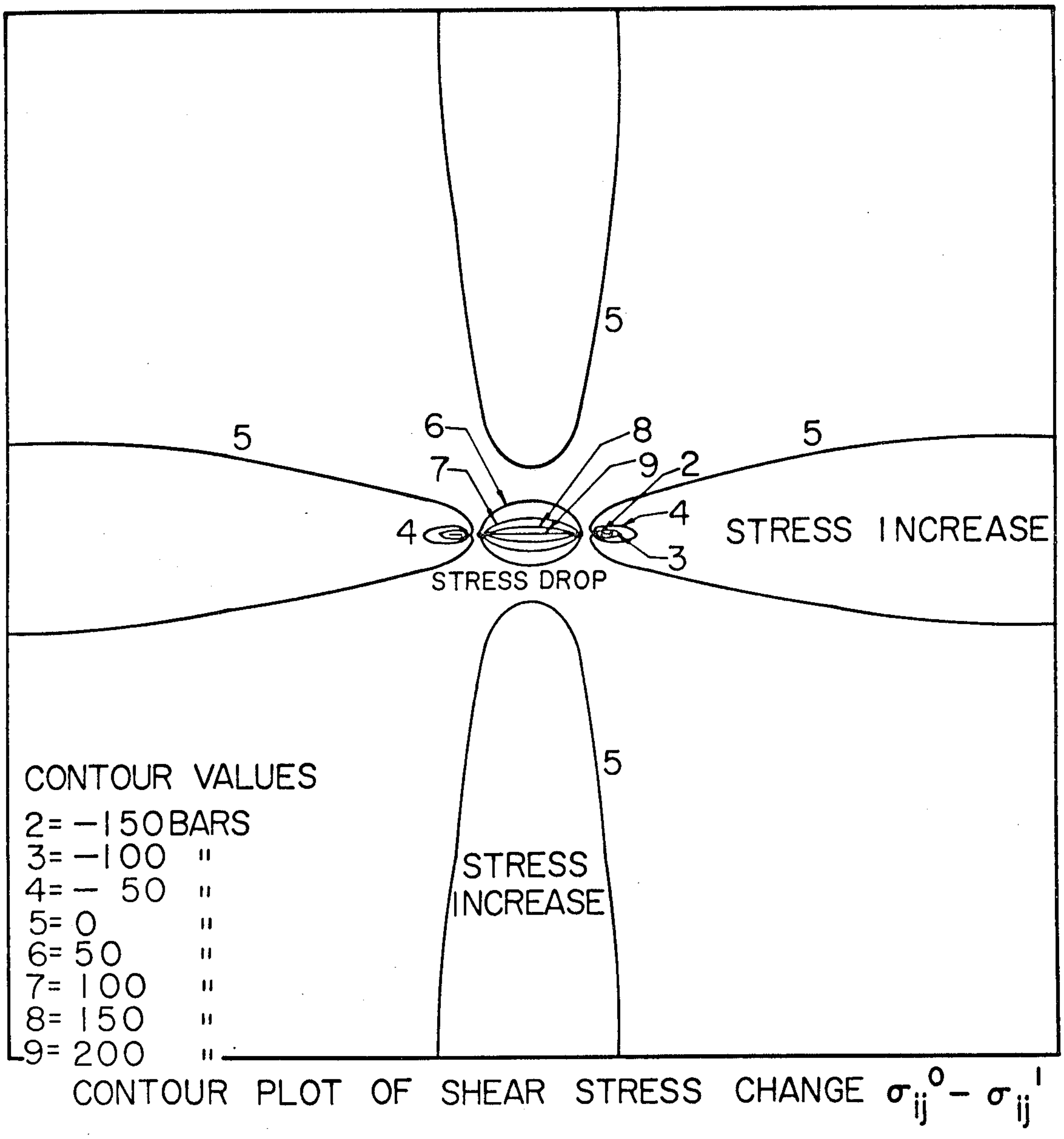

Figure 23. Stress change for complete stress drop on the fault. Prestress is 200 bars pure shear.

dislocation provided the fault offset has the quasi parabolic shape needed to maintain constant stress drop on the fault place. In both cases, this generated a strain energy density change or maximum radiated energy of 0.75×10^{21} ergs per km of fault length. Or if the fault behaves in such a way that the stress drop is every where constant and equal to 200 bars, this gives

$E_R = \eta \times 0.75 \times 10^{21}$ ergs per km^2 of fault area. Brune's formula

$$E_R = \eta < \sigma ><u> A$$

would give the same value for an average relative displacement on the fault surface of 7.5 m. By varying the amount by which the shear modulus is reduced in the "failure" zone or alternatively by varying the amplitude factor $< u >$ of the dislocation, we can map Eq. (3.19) at constant prestress. By changing the amount of prestress while holding the dislocation invariant, we can map Eq. (3.19) as a function of prestress.

Figure 24 shows the linear behavior of δW as a function of $\sigma_{ij}^{(0)}$. As can be seen on this plot, if the medium is prestressed uniformly with a shear prestress of 200 bars, then, in the absence of gravity, the maximum energy released is found at the point of total stress relaxation on the fault plane (point A). This particular "earthquake" could release more energy, however, if it occurred in a medium with a prestress superior to the stress drop. For example, point B represents the energy available for seismic radiation for a fault that results in 200 bars drop in a prestress field of 300 bars. If body forces are included and the earthquake results in a net increase (decrease) of gravitational energy in an amount equivalent to 1.25×10^{21} ergs per km^2 of fault, δW AS A FUNCTION OF PRESTRESS

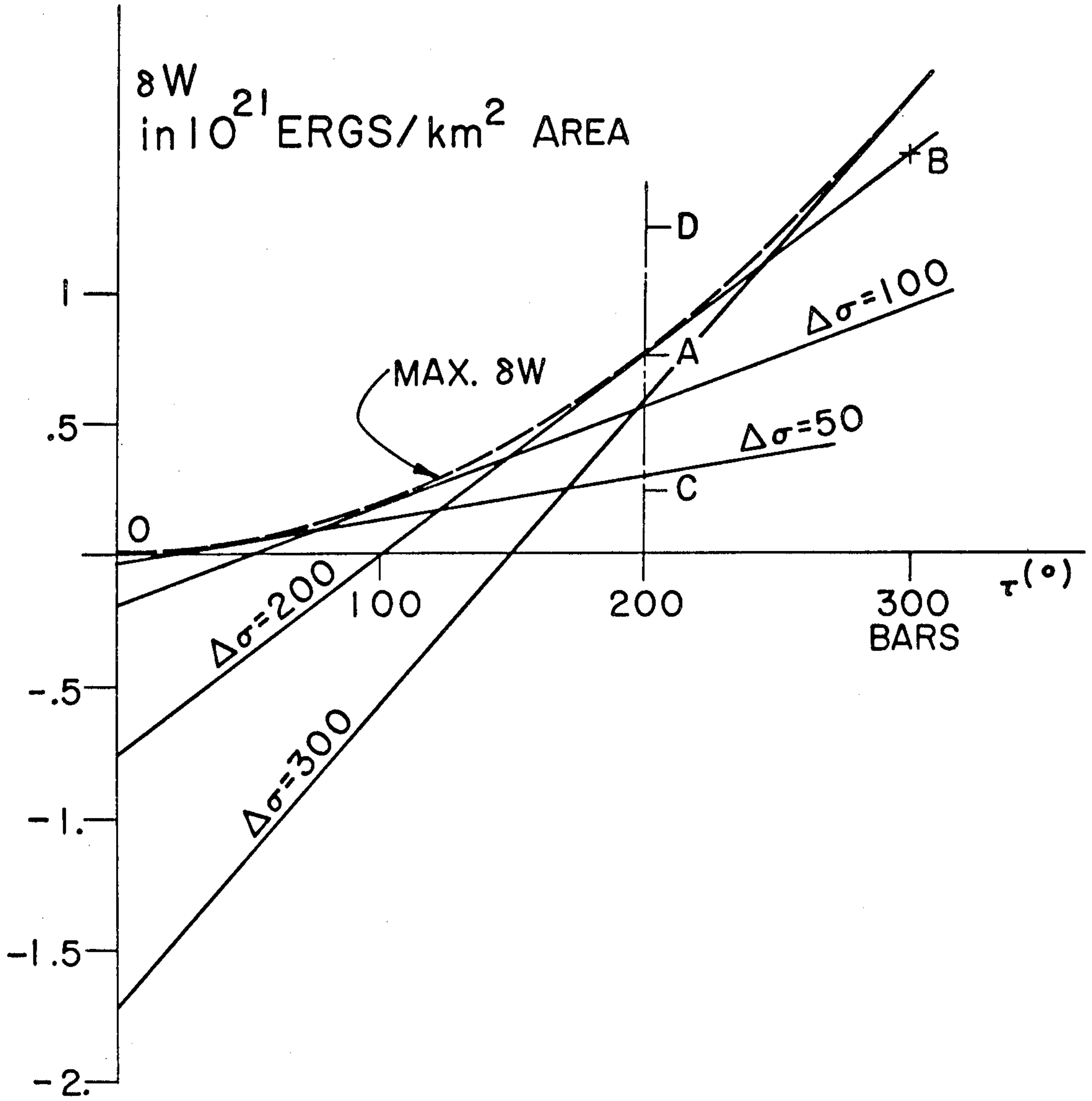

Figure 24. Results of energy calculations showing the linear relationship of δW with prestress.

then the energy available for seismic radiation changes by that amount. This is shown by point C (point D) on the figure. The envelope of all the lines of strain-energy-change, as a function of prestress, corresponds to total stress drop on the fault plane. In the absence of significant body forces effect, it represents the maximum release of energy for this model.

Figure 25 shows the quadratic behavior of δW as a function of $< U >$ (or $<\Delta\sigma>$). If the influence of body forces is neglected, the energy released, given here per square kilometer of fault area, can be interpolated to any fault, provided $\Delta\sigma_{ij}$ and $\sigma_{ij}^{(0)}$ are constant over the fault plane.

This means that if an earthquake can be represented as a phenomenon occurring in a uniform prestress environment in which it releases a constant stress along its entire fault area, its energy release can be estimated from Figure 25 by a simple scaling. For instance, assume that the San Francisco earthquake occurred in a uniform 100 bar prestress field. Assume that its stress drop was everywhere constant and equal to 96 bars (Chinnery, 1964). Then, for a fault area of 4.400 km^2 (Brune and Allen, 1967), we get directly from Figure 25

$$\begin{aligned} \delta W &= 0.19 \times 10^{21} \times 4400 \\ &= 8.36 \times 10^{24} \text{ ergs} \end{aligned}$$

This can be compared directly to the seismic energy since this event had no significant uplift or subsidence. Thus

$$\log_{10} E_{GR} = 11.8 + 1.5\, M_L$$

$$E_{GR} = 1.5 \times 10^{24} \text{ ergs for } M_L = 8.3$$

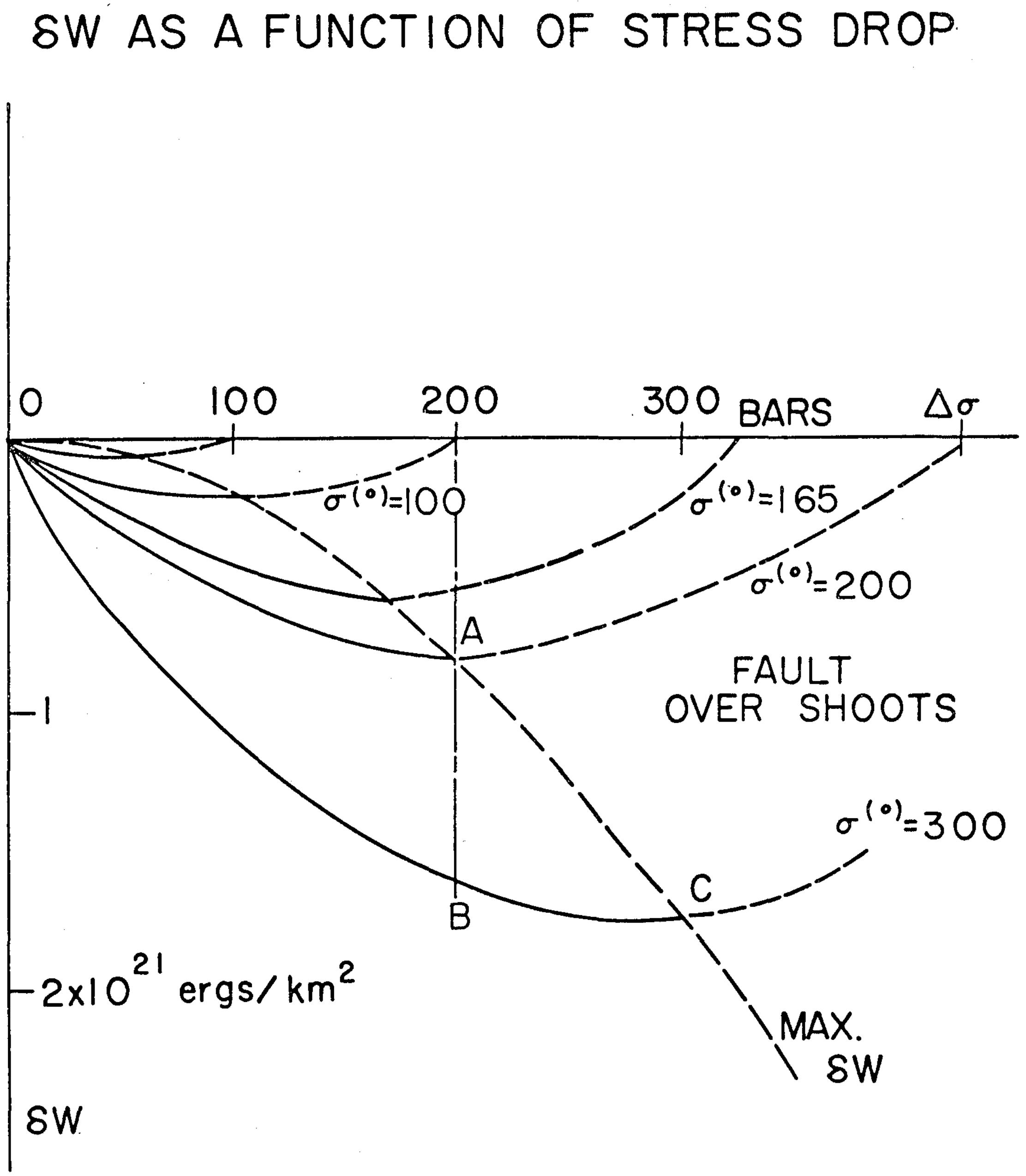

Figure 25. δW as a quadratic of $\sigma^{(0)}$, for a uniform prestress field and various levels of stress drop. Stress drop is constant along the fault surface.

This would indicate a seismic efficiency of about 0.18.

Of course, as we shall see in Chapter IV, we suspect that no earthquake fits the requirements of uniform prestress and stress drop and, as we will show, consideration of average values for them leads to large underestimates of both moment and energy change.

In Figure 25 we show the positions of points A and B discussed earlier. The curves to the right of the line of "maximum" energy released are dashed because they correspond to events that released more stress than was available. Those events would be characterized by a fault "overshoot", meaning that the system does work rearranging the prestress field instead of "relaxing" it.

If body forces (mainly the force of gravity) are considered, their influence can be viewed as an "equivalent" prestress. From (3.19) we can write

$$\langle \sigma_{BF}^{(0)} \rangle = \frac{\int_V F_i \, \delta B_i \, dV}{\int_\Sigma S_{ij}^{(0)} \Delta C_i n_j \, d\Sigma}$$

where $\langle \sigma_{BF}^{(0)} \rangle$ is the prestress equivalent of body forces. Then

$$\delta W = \left(\langle \sigma^{(0)} \rangle + \langle \sigma_{BF}^{(0)} \rangle \right) \langle U \rangle \int_\Sigma S_{ij}^{(0)} \Delta C_i n_j \, d\Sigma - \frac{1}{2} \langle U \rangle^2 \int_\Sigma \Delta A_{ij} \Delta C_i n_j \, d\Sigma$$

which is equivalent to a situation without body forces, but an "apparent" prestress of

$$\langle \sigma^{(0)} \rangle + \langle \sigma_{BF}^{(0)} \rangle$$

Assume an event caused a net loss of gravitational potential energy such that

$$\langle \sigma^{(0)}_{BF} \rangle = +100 \text{ bars}$$

If the actual prestress amplitude is $\sigma^{(0)} = 200$ bars, then the curve marked 300 is the actual energy versus stress drop relationship to consider here. It means that point C in Figure 25 corresponds to the energy released by an earthquake which occurred in a 200 bar prestress environment, but resulted in an apparent 300 bar stress drop. This stress change is actually 200 bars drop and 100 bars "overshoot". Interpreted differently, this event can be seen as transferring gravitational potential energy into seismic radiations.

Conclusions

The particular form of energy release formulation presented here shows that in order to analyze the energy balance of a shallow earthquake which results in thrust or normal faulting, one cannot neglect the influence of changes in the gravitational potential energy. It was shown through homogeneous models that the finite element numerical technique can compute directly the energy terms without the idealizations necessary to make closed form solutions tractable.

The next chapter deals with applications of this technique to several earthquakes, showing how bounds can be placed on their source parameters such as stress drop, prestress and energy released.

IV. CALCULATION OF PRESTRESS, STRESS DROP AND ENERGY RELEASED FOR THREE EARTHQUAKES

Introduction

The preceding chapters have shown how the finite element numerical technique can be used as a tool to invert zero frequency earthquake data in order to estimate the fault offset which caused them. From these possible solutions, it was shown that such important fault parameters as moment and stress drop could be directly computed without averaging. Chapter III showed that by investigating static equilibrium before and after the injection of a fault, one can place limits on the energy balance of the event on a local scale. This chapter will deal with applications of these concepts to three different earthquakes. Careful consideration will be given to the possible prestress environment in which they occurred.

The San Fernando Earthquake of February 9, 1971

This event is a particularly interesting application of the techniques described above. The finite element modeling of Chapter II has shown that in order to fit the observed permanent displacements at the free surface, the possible solutions all showed an order of magnitude variation of relative displacement along the fault surface. This allows useful investigation of stress drop with its variations in space and comparison with averaging techniques. Furthermore, this earthquake was accompanied by a net uplift of the free surface, corresponding to an increase of gravitational potential energy. Alewine (personal communication, 1972) estimated this increase to be between 10^{22} and

10^{23} ergs depending upon the decay of relative displacement with depth. Wyss and Hanks (1972) on the basis of body wave study estimated the radiated energy to be in the range of $10^{21.3}$ to $10^{22.3}$ ergs.

Clearly, regardless of how individually accurate these estimates are, they indicate that for this particular event the redistribution of mass associated with the earthquake is not a second order effect. Thus considerations of the effect of body forces on the energy balance is critical here.

For the sake of clarity, we shall start by studying the effect of a uniform prestress upon our principal solution and one of the alternatives with a large stress drop at the hypocenter. In this case, the boundary displacements applied on the grid are such that the medium is prestressed in pure horizontal compression. The force of gravity is not considered. The first part of Figure 26 shows how such a prestress is effected by the geology. We have here an average stress amplitude of 350 bars (175 bars shear stress). The presence of soft sediments (Saugus-type formations and the San Fernando Valley formation) is clearly visible in the upper left corner; they reduce the prestress by a factor of 5. The second part of the figure is an approximate contour plot of the strain energy density change caused by the failure of the medium along the fault plane. The relative displacement used here is the one of Figure 9.

Near the surface, where the displacements are unusually large compared to the average fault offset, there is an increase in strain energy density. This would be somewhat reduced if multiple faulting or plastic behavior was considered. The other region of strain energy

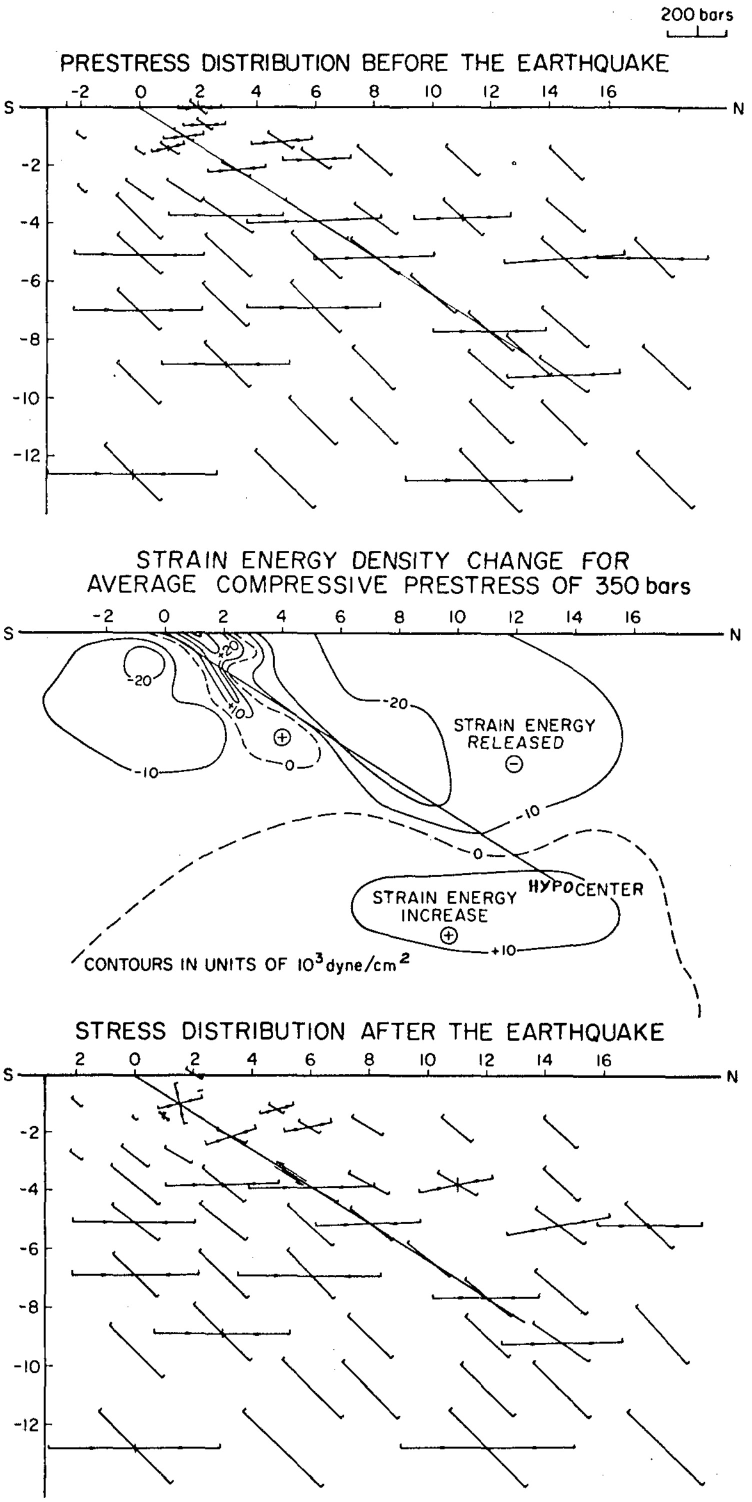

Figure 26. Prestress and final stress distirbution around the fault. The horizontal lines are the horizontal compressive stress, the maximum shear stress is shown at 45° from the σ_{max}. The "dislocation" used is shown in Fig. 12 (BB'). No gravity in this model.

increase is found in the hypocentral area. The stresses there are not relaxed and it makes it conceptually difficult to understand why the fault did not propagate downward. One possibility is that the rupture started farther up the fault and propagated in both directions growing in the upward direction because of the free surface and dying out downward because of a possible increase with depth of either the static or the dynamic stress, or an increase of the strength of the rock with confining pressure. If one of the alternative solutions of Chapter II was used, on a prestress background of 350 bars, the "earthquake" would even be more difficult to explain in terms of failure mechanism. In this case, the region immediately below the hypocentral region would be stressed up and the hypocentral region itself would show a significant overshoot. We would regard this event as impossible since crack tip stresses seem to exceed static friction or yield stress and the net strain energy of the system is increased as shown in Figure 27.

Figure 27 shows the results of several such calculations. Since the change of strain energy of the system is linear with prestress, we show two lines corresponding respectively to our principal solution for cross section BB' and to one of the alternatives with rapid growth of the offset. In both cases, this determines the origin and the slope of each line. Since we have no gravity acting, these lines correspond to

$$\int_{\Sigma} < \sigma_{ij} > \Delta u_i n_j \, ds = \delta W$$

The interpretation is that if our principal solution is the appropriate one, a prestress of 180 bars is required before any release of energy occurs. If the alternative solution is preferred, then a minimum of

420 bars is required.

A comparison with the seismic energy calculated by Wyss and Hanks (1972) from shear waves, by Trifunac (1971) from the Pacoima Dam accelerogram and E_{GR} obtained from the Gutenberg-Richter formulation, is shown in the figure. In order to get the energy released per km of fault length, we assumed a fault of 10 km length with a cross section equivalent to BB'.

Since the seismic energy is only a fraction of the strain energy change, depending on seismic efficiency (i.e., heat losses, nonlinear behavior, attenuation, etc.), the models presented here would require an average compressive prestress of at least 350 bars in order to satisfy the observations. Introduction of the force of gravity would increase this minimum by a factor of two (assuming an increase of gravitational potential energy of 5×10^{21} ergs per km of fault length or an equivalent additional prestress of 350 bars).

By contrast, if we use the conventional formulae, with averaged fault parameters, i.e.

$$\begin{aligned} E &= <\sigma><u>A \\ &= \sigma^{(0)} - 1/2\Delta\sigma = \sigma^{(0)} - 27.0 \text{ bars} \end{aligned}$$

with (compressive stress)

$$<u> = 2.35 \text{ m}$$

$$A = 16 \text{ km}^2 \text{ per km of FL}$$

we get the dashed line marked A. Since the slope of these lines is (from Chapter III)

$$\int_{\Sigma} <S_{ij}> \Delta u_i n_j \, ds \simeq \frac{M_o}{\mu}$$

ENERGY δW VERSUS INITIAL AVERAGE STRESS

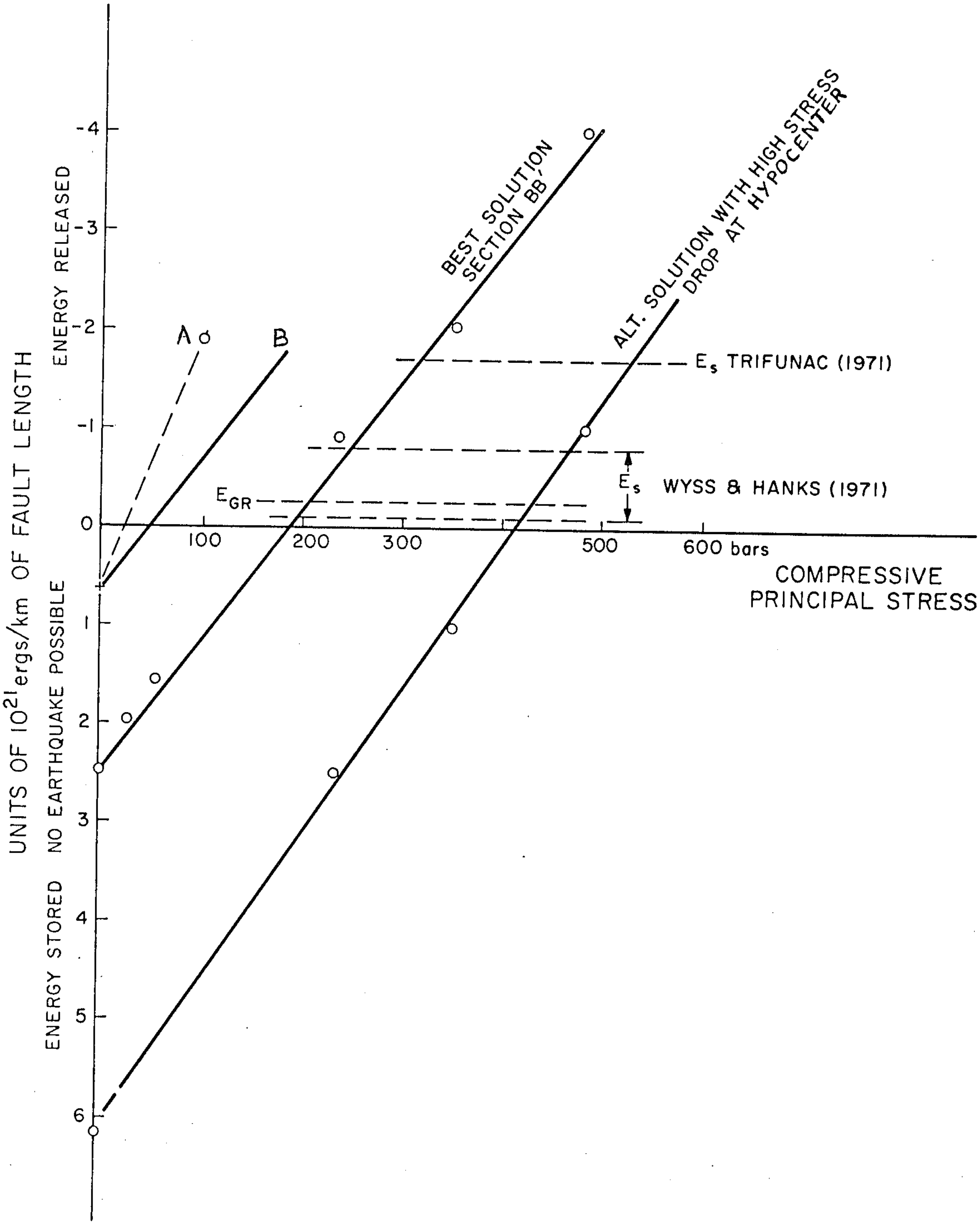

Figure 27. Change of strain energy versus prestress for section BB'. Best solution is shown in Fig. 12; the alternative is from Fig. 15. A and B represent what one would obtain from averaged values of stress drop and fault offset. No gravity in these models.

a comparison of the dashed line with the solid line with same origin and drawn parallel to the best solution (line B) gives a direct estimate of the error made in assuming σ_{ij} and Δu_i constant. Comparison of the origins is an estimate of the difference between

$$1/2\, \Delta\sigma \langle u\rangle A \qquad \text{and} \qquad 1/2 \int_{\Sigma} \Delta\sigma_{ij}\, \Delta u_i n_j \, ds$$

or of the underestimate of energy released by the fault that results from averaging the fault parameters (here a factor of 4). Clearly, this simplified approach leads to the conclusion that if average fault offsets, thus average stress drops, exist, low uniform prestress is sufficient to generate a net energy release. If strong stress drop concentrations exist, then a large uniform prestress is required before an earthquake can occur. This stems from our oversimplified prestress field. Intuitively, one can imagine a natural environment where the prestress and the stress drop have a quasi parallel distribution over the fault surface. In other words, if they can both be expressed in terms of a unit amplitude stress distribution τ_{ij}, i.e.

$$\tau_{ij} = \frac{\sigma^{(0)}_{ij}}{\left(\int_{\Sigma} \sigma^{(0)}_{ij} \sigma^{(0)}_{ij}\, d\Sigma\right)^{1/2}} = \frac{\sigma^{(0)}_{ij}}{\langle\sigma(0)\rangle}$$

and

$$\tau_{ij} = \frac{\Delta\sigma_{ij}}{\left(\int_{\Sigma} \Delta\sigma_{ij} \Delta\sigma_{ij}\, d\Sigma\right)^{1/2}} = \frac{\Delta\sigma_{ij}}{\langle\Delta\sigma\rangle}$$

This means that provided τ_{ij} has order of magnitude variations along the fault surface, one can obtain localized prestress of 1 kbar for a "background" prestress amplitude of 100 bar. In this text, we shall refer to the average prestress amplitude as first order. This first order stress could have its origin in large scale tectonic features such as plate motions of the earth's crust. We shall refer to the variations of ζ_{ij} as second order effects. These could be the result of local geology (possibly on a smaller scale than that modeled here), weak zones such as fault gouges, porous and fractured formations containing water under pressure (consolidation or swelling phenomena). Further, past earthquakes or creep events, by redistributing the stress field in a nonuniform fashion, can be responsible for such second order effects.

Clearly, in order to obtain the second order effects, some changes are required in our models. This is the subject of the next section.

Finite element model for "second order" stress variations

A portion of the finite element grid used is shown in Figure 28. This grid was designed to model a fault similar to that shown in Figure 17. Recent gravity work (Alewine, personal communication) has confirmed that a significant uplift (up to 35 cm) occurred in the San Gabriel Mountains, thus strengthening the possibility that Figure 17 represents the "best fit". The fault slip will be modeled either by a specified nodal slip or by relaxation of those elements numbered from 1 to 9.

If the displacement function of Figure 17 is adopted, then clearly, large variations of prestress are to be introduced in order to obtain enough relaxation at depth. Since we have no data on the geology at depth, we will assume that the secular uplift of the San Gabriels (Savage et al., 1971) and the absence of historic earthquakes in California at depths greater than 20 km indicate that the depth prolongation of the San Fernando earthquake has been responding plastically to the tectonic forces. This is modeled by forcing a slip on the fault below the hypocenter (indicated by arrows on the grid). Thus, the prestress field will be composed of: specified displacements on the sides of the grid, introducing pure compression horizontally (first order tectonic stress), the force of gravity, and specified "creep" at depth, resulting in a large stress concentration in the hypocentral region.

Considerable debate exists among tectonophysicists as to the state of stress in the earth's crust, in particular in terms of the stress distribution that results from the gravitational loading. For depths greater than, say, 50 km, the consensus is that the variations in elevation of the crust are supported hydrostatically. Based on the theory of isostasy, which states that the total mass of rock in any vertical column of unit cross section is constant, the reasoning includes consideration of the departures from sphericity of the geoid , postulated rebound of areas under glaciation during the last ice age and assumed creep behavior in the upper mantle.

This leads researchers (Stacey, 1969; Birch, 1964) to give quantitative estimates of the strength of materials for the upper mantle. The upper mantle, then, appears to support stress differences in the range of 10 to 100 bars, stress differences associated with a mean hydrostatic pressure of several tens of kilobars. Thus the upper mantle is very close to a hydrostatic stress distribution.

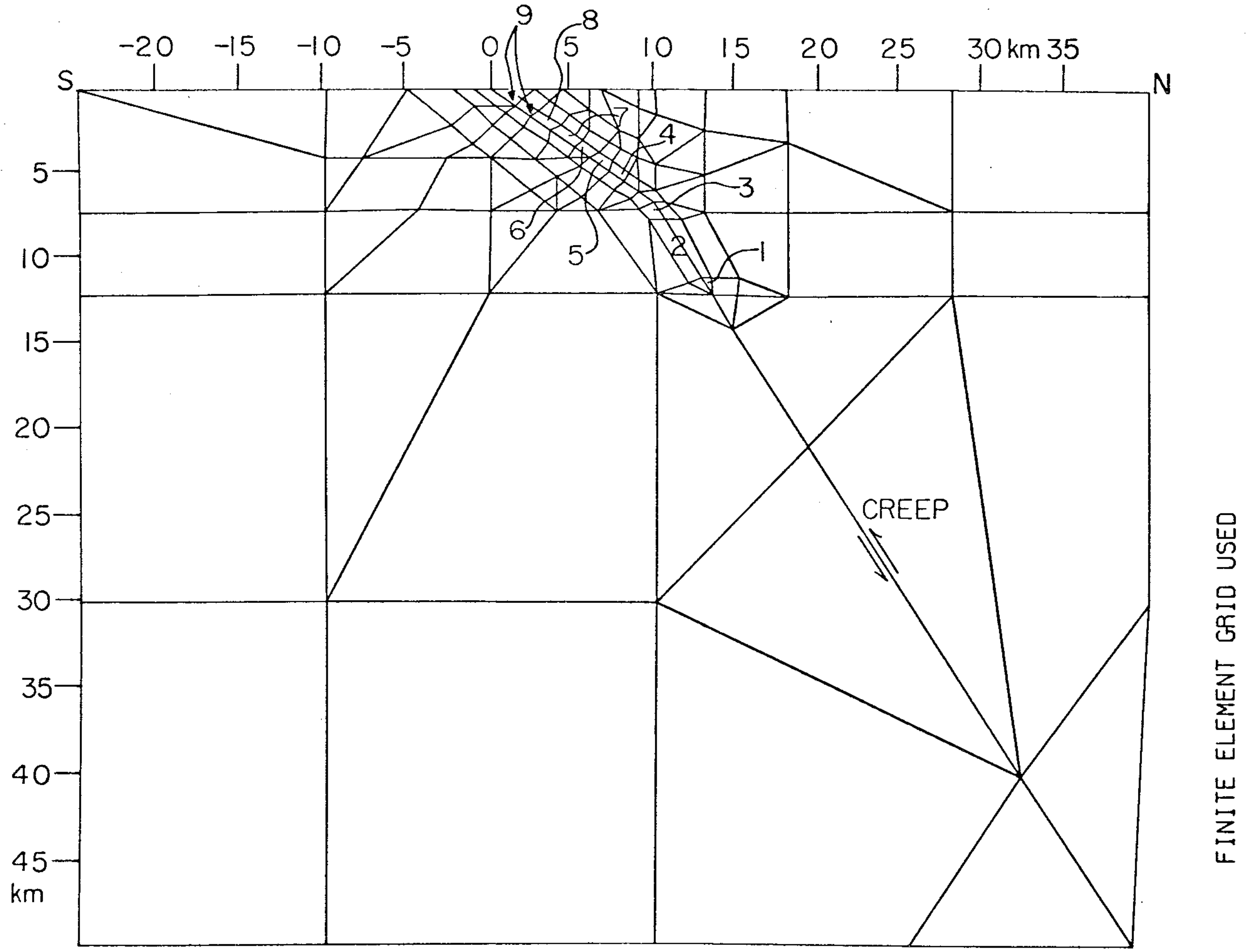

Figure 28. Small portion of the finite element grid used in Chapter III for the San Fernando earthquake. The elements numbered are those involved in the relaxation study.

This is not necessarily correct for the crust, however. Conventional theories, used in underground excavation design, have assumed in the past that hydrostatic stress distribution is valid for the earth's crust. However, many authors have recently challenged this assumption (e.g., Judd, 1964).

If we assume a perfectly isotropic homogeneous block of the earth's crust in static equilibrium under its own weight, the stress distribution throughout the body is estimated by one of the following:

(1) The hydrostatic approach

$$\tau_{xx} = \tau_{yy} = \tau_{zz} = -\rho g z \qquad \tau_{max} = 0$$

where z is the vertical coordinate.

(2) The two-directional stress approach, which uses the theory of elasticity for one-dimensional compression of a perfectly elastic solid with a definite Poisson's ratio (Clark and Candle, 1964),

$$\tau_{xx} = \tau_{yy} = \frac{\nu}{1+\nu}\,\tau_{zz}$$

so with $\tau_{zz} = -\rho g z$

then $\tau_{xx} = \tau_{yy} = -1/3\ \rho g z \qquad \text{for } \nu = 0.25$

implying $\tau_{max} = 1/3\ \rho g z$

These two approaches actually give two extremes for the influence of the body force ρg. The second gives a stress ratio

$$\frac{\tau_{xx}}{\tau_{yy}} = 1/3$$

while the first gives a ratio of 1. Handin (1964) points out that this ratio is really a function of the strength of the rock in situ, and of the time scale of the loading. Deere (1964) shows that because of the difficulty in measuring an effective Poisson's ratio for the rock mass and because of the stress history in the crust, the influence of ρg may result in a stress ratio anywhere between 0.33 and 1.

Stress measurements in situ (in tunnels and deep mines) indicate that the stress distribution is anomalous when compared to the hydrostatic theory (Wantland, 1964). Clearly, these measurements are limited to the very top of the crust where added complications arise from erosion (removal of the overlying load without necessarily reducing the horizontal stress).

In the depth range of 10 to 30 km where the hypocenters of the three earthquakes studied in this thesis are found, no in situ measurements exist. We can conjecture, however, that at those depths, the rocks can support maximum stress differences equal to those associated with the support of high mountains and deep oceanic trenches. These imply that the middle of the crust can support stress differences of the order of kilobars (Birch, 1964).

If we applied the full gravity load statically on our model, this would give (with a Poisson's ratio of 0.25) a stress difference of approximately 2.5 kbars per 10 km of depth. This is clearly too large for the rocks to support it on a geological scale without flow (Mogi, 1972).

Using complete hydrostatic distribution of the gravity load was considered unrealistic since consideration of creep in the crust is still largely a matter of speculation. Birch (1964) indicates that the reduction of mountains by erosion is probably much more rapid than their spread by creep at shallow depths which, if we follow Deere, may result in a ratio τ_{xx}/τ_{zz} approaching 1. Thus, quite arbitrarily we assumed that the effect of force of gravity on the sections studied would be best represented by loading statically one-tenth of the material weight. This is equivalent to assuming

$$\tau_{zz} = -\rho g z$$

$$\tau_{xx} = \tau_{yy} = -0.933\ \rho g z$$

or a stress ratio of 0.933. This result could have been obtained by loading the material with the full body force while making Poisson's ratio equal to nearly one-half, thus modeling flowage. In this case, the natural stress distribution caused by the force of gravity could be directly computed. However, the rocks involved react nearly like a Poisson's solid during the time scale relevant to the earthquake phenomenon. Thus, for the simplicity of the numerical scheme, it was felt easier to keep for the geological units a Poisson's ratio of nearly one-quarter, while keeping only a small portion of the force of gravity as an instantaneous static load.

The best prestress field, in terms of net energy released and failure mechanism, was obtained for a tectonic compression of approximately 360 bars (180 bars maximum shear stress), a creep on the fault at depth resulting in a 10 m relative displacement and a shear stress concentration of nearly 600 bars at the hypocenter. Together with the nonhydrostatic effect of body forces added as a static load, this result in the maximum shear stress distribution is shown in Figure 29.

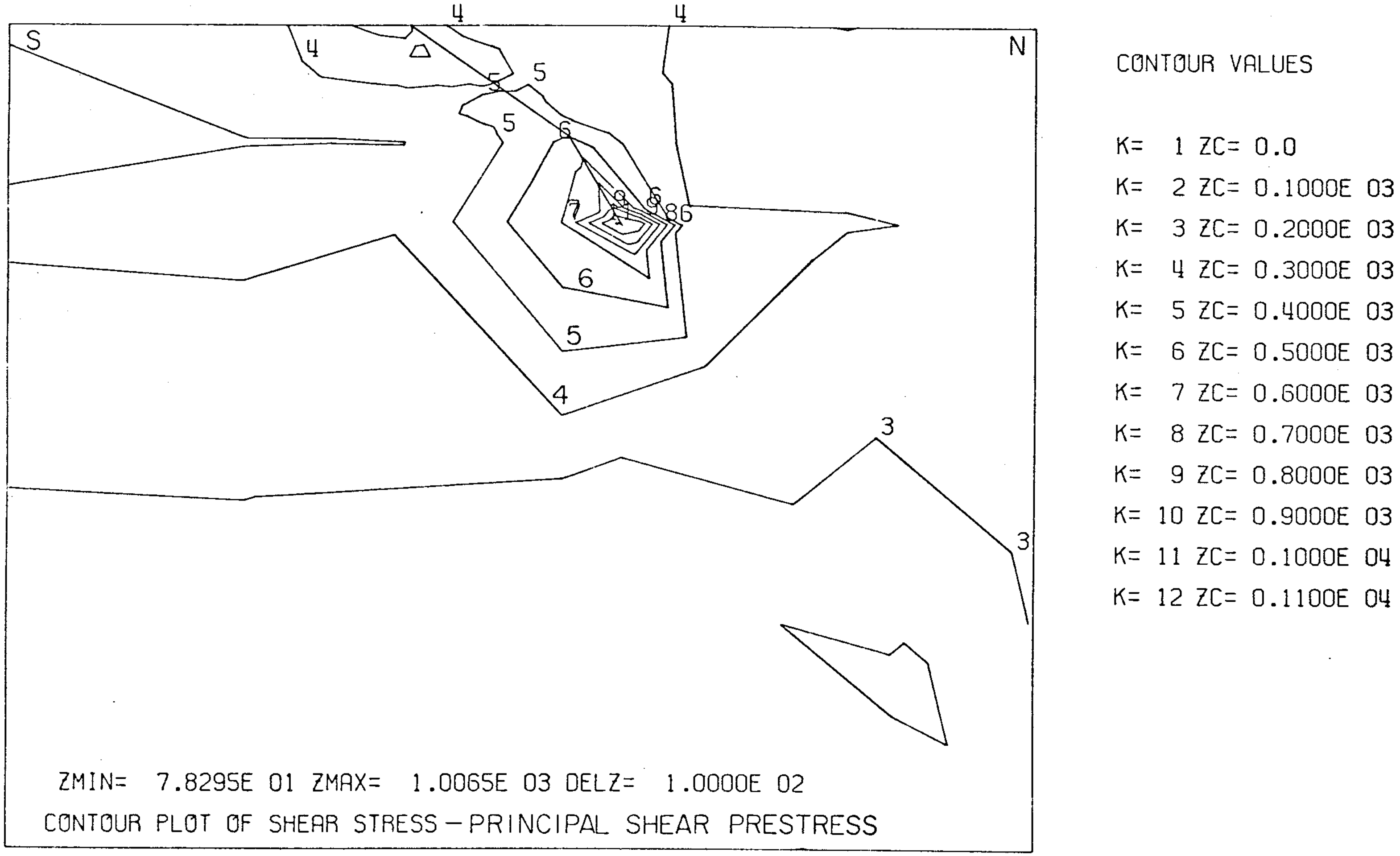

Figure 29. Prestress field (in bars) used for the "best" model.

This represents the initial stress field of our best model. The soft Saugus-type formation again results in a local low prestress and the largest shear stress is found at the hypocenter (985 bars). The contour plot of stored strain energy density (first part of Fig. 30) shows that its distribution matches that of shear stress. Thus most of the energy available to the earthquake is stored in the hypocentral region. This is dramatized in the second half of the figure where the strain energy density change caused by relaxing only the hypocentral region (numbered 1 on the grid) is shown.

The net δW can be estimated to be approximately 1×10^{21} ergs per kilometer of fault length or a large portion of the total energy released, comparable, in fact, to the estimates of Trifunac (1972) for the near field seismic energy.

Systematics of Relaxation

As was described in the preceding chapter, we can study the prestress-energy release of an earthquake either by imposing an offset along the fault surface or by "relaxing" elements parallel to the fault. The second technique has the advantage of being more natural in the sense that the medium responds to the prestress field without introduction of internal forces which could result in overshoot.

Because of stability requirements of the numerical technique (i.e., relative size of the elements of the stiffness matrix), the material blocks which are relaxed need have a finite thickness to length ratio. This can be corrected by assuming that the stress drop is constant while the strain drop increases with diminishing thickness of the

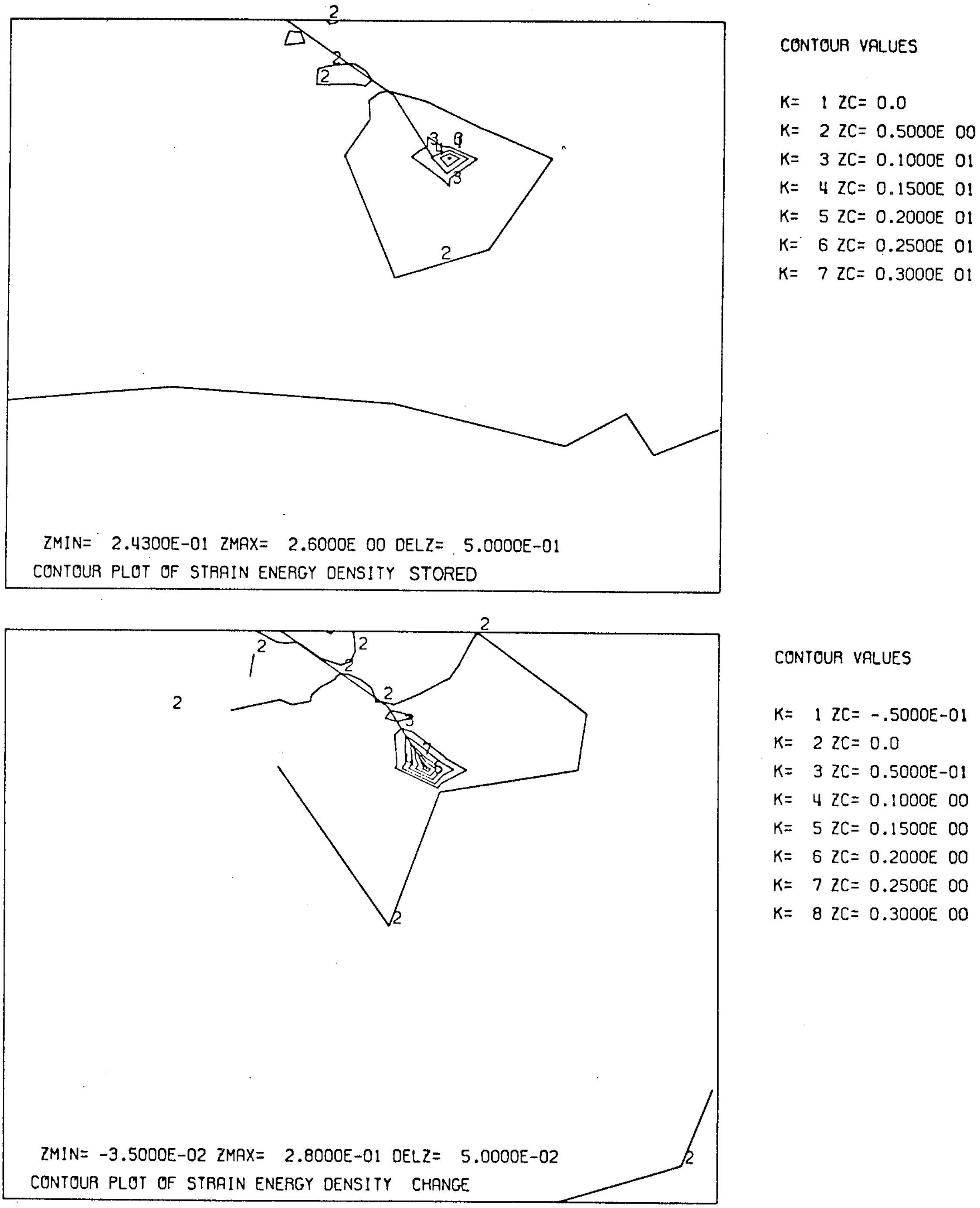

Figure 30. Comparison of the stored strain energy before the event, with the strain energy change caused by relaxation of element 1. Units are 10^{21} ergs per km^3.

failure zone. This insures that the displacement field away from the fault and the stress drop remain unchanged.

In the model of the San Fernando earthquake, the elements relaxed are indicated in Figure 28 by numbers in the actual sequence of fault propagation. They have a thickness between 0.5 and 1.5 km. Table 3 gives the shear moduli assigned to each of the materials, together with the "real" drop in shear strength, assuming a thickness of the fault gouge of 50 cm. The values in Table 3 are those which gave a vertical uplift on the free surface similar to the dislocation solution presented in Figure 17.

The largest drop of shear strength is found in element 9a where the largest fault slip occurred. Multiple faults branching off at 1 km depth would have the same result. The relaxation in the hypocentral region (elements 1, 2 and 3) is also very significant. This is needed in order to obtain up to 35 cm uplift in the epicentral area. Similarly, we left unchanged those materials at the knee of the fault (between elements 3 and 4) in order to force the free surface uplift to be less than 10 cm, 6 km north of the fault scarp.

Figure 31 gives a comparison of the relative vertical displacements generated by dislocation and relaxation in cross section BB'. The resulting displacement fields are remarkably similar except at a depth of 1 km. There the dislocation generated an 8 m offset at one point only, while the relaxation spreads it over the entire length of element 9a. Furthermore, since the relaxed materials were isotropic, there is a small amount of dilation occurring, spreading the

TABLE 3

Element N=° from Fig. 28	Shear Modulus in dynes cm^2		
	Before	Relaxed	Corrected for 0.5 Thickness
1	3.46×10^{11}	0.1×10^{11}	3.3×10^6
2	3.46×10^{11}	0.1×10^{11}	3.3×10^6
3	3.46×10^{11}	0.1×10^{11}	3.3×10^6
4	3.13×10^{11}	0.3×10^{11}	30.0×10^6
5	3.13×10^{11}	0.3×10^{11}	30.0×10^6
6	1.5×10^{11}	0.3×10^{11}	30.0×10^6
7	1.5×10^{11}	$.072 \times 10^{11}$	7.2×10^6
8	1.5×10^{11}	$.072 \times 10^{11}$	7.2×10^6
9a	1.5×10^{11}	$.01 \times 10^{11}$	1.0×10^6
9b	1.5×10^{11}	$.3 \times 10^{11}$	30.0×10^6

displacements away from the fault ever so slightly.

Figure 32 compares the shear stress drops obtained by injecting the dislocation in the prestress field described above with that generated by the dislocation. Although the shape of the contours are very similar, important differences arise here.

Because the numerical computation of stress is made at the centroid of each element, then transferred to the nodal points by averaging the stresses of the elements surrounding the node, a significant error is introduced in the values given for the nodes on the fault surface. By contrast, the relaxation gives the actual values of the stress drop on the fault surface, but because of the finite thickness of the "fault gouge", these maximum stress drops occur on a greater area than they would if the gouge was only 50 cm thick.

As a result, the actual stress drop plot should be a composite of the two plots of Figure 32 with the maximum values on the fault given by the relaxation and the stress drop away from the fault given by the dislocation model. The result is shown in Figure 33. In any case, the interpretation here is that our model of the San Fernando mechanism results in a large stress drop in the hypocentral region up to a maximum of 650 bars. At 6 km depth, the fault changes slope and locks up, resulting in a large stress increase up to 400 bars. This places severe constraints on the history of this event and will be discussed later in this thesis in terms of failure criteria and aftershocks. At this point, we will explore further the evolution with time of the fault.

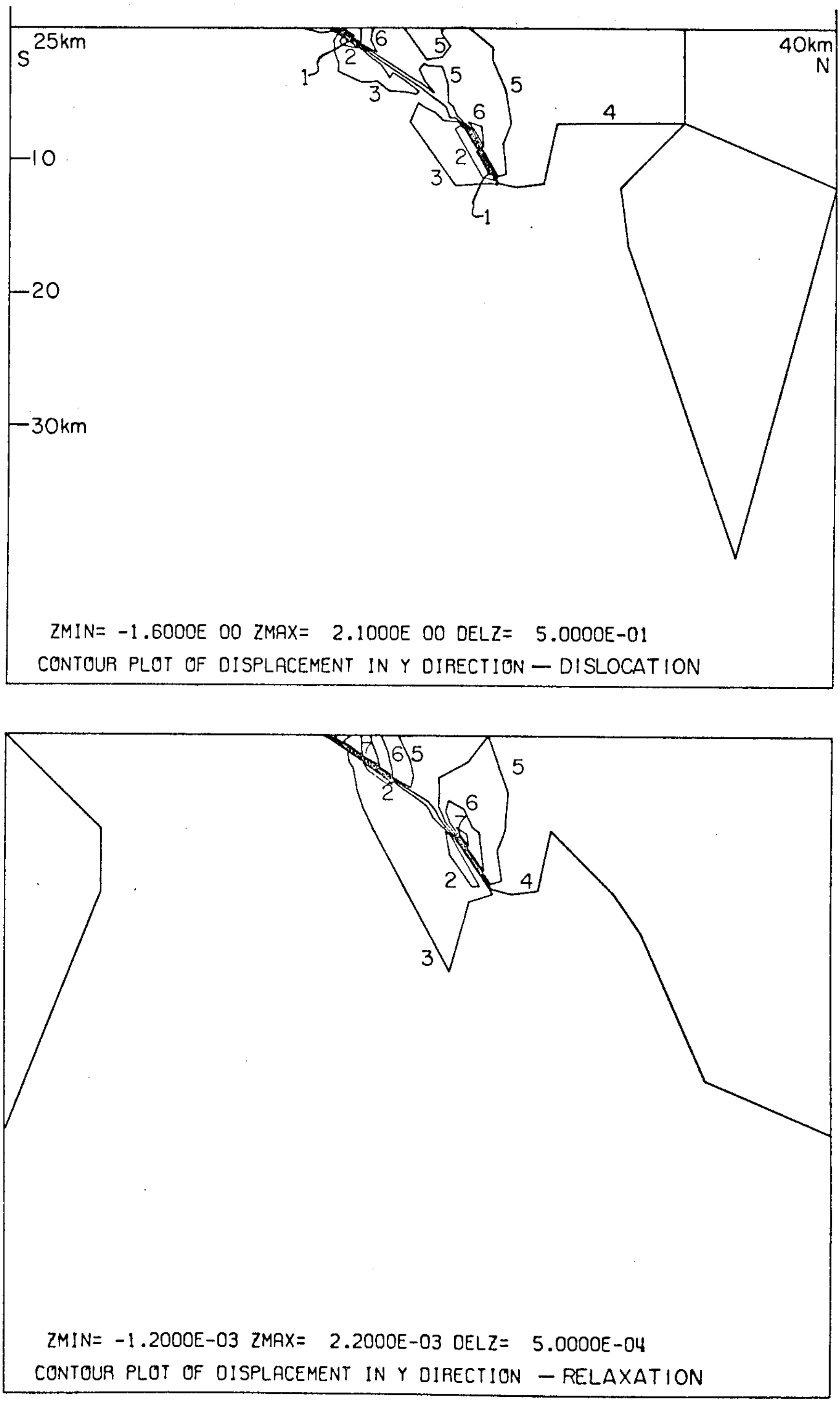

Figure 31. Vertical relative displacements that result from the finite element models of "dislocation" and "relaxation". Units are kilometers.

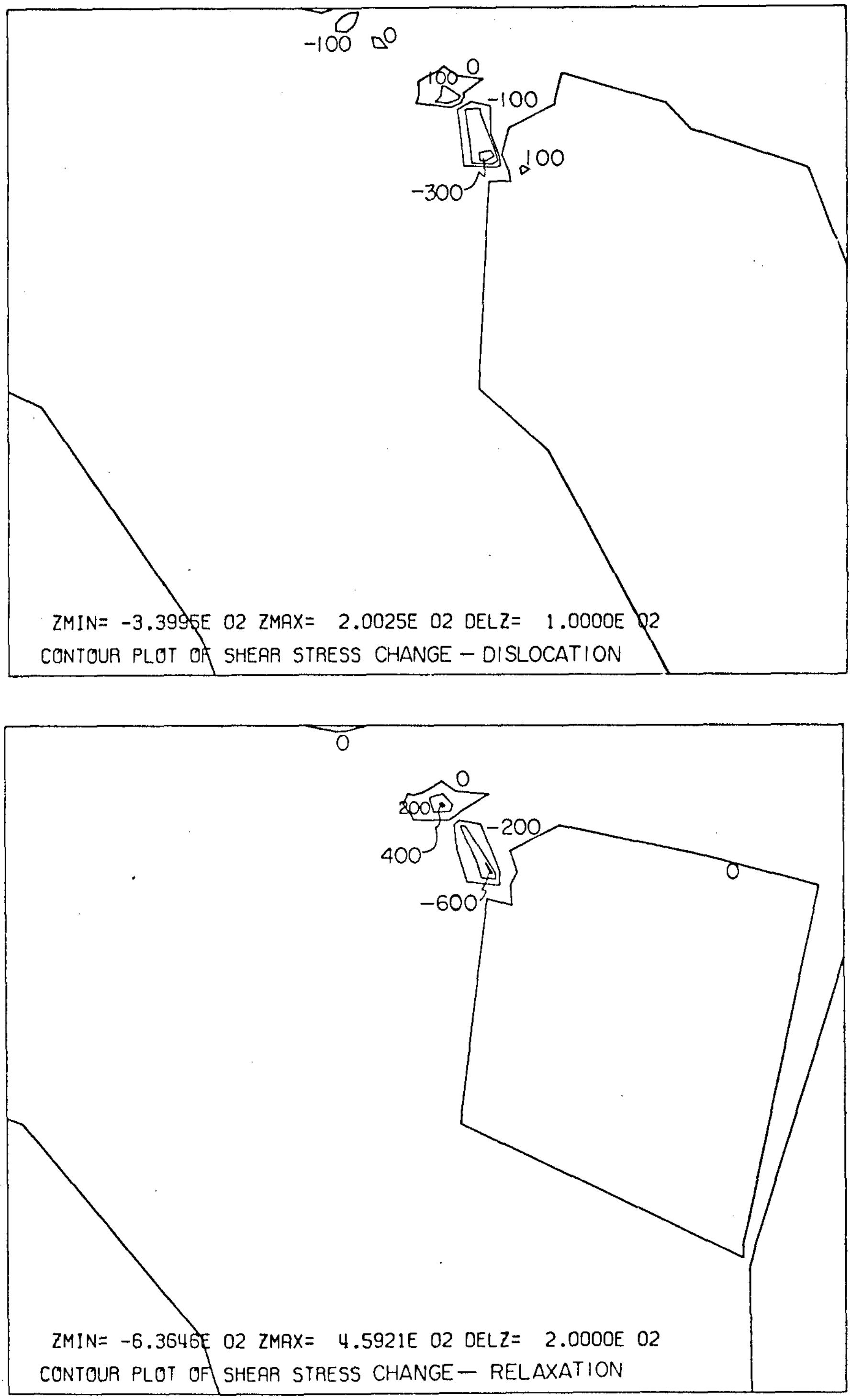

Figure 32. Shear stress change at 40° dip. Units are bars.

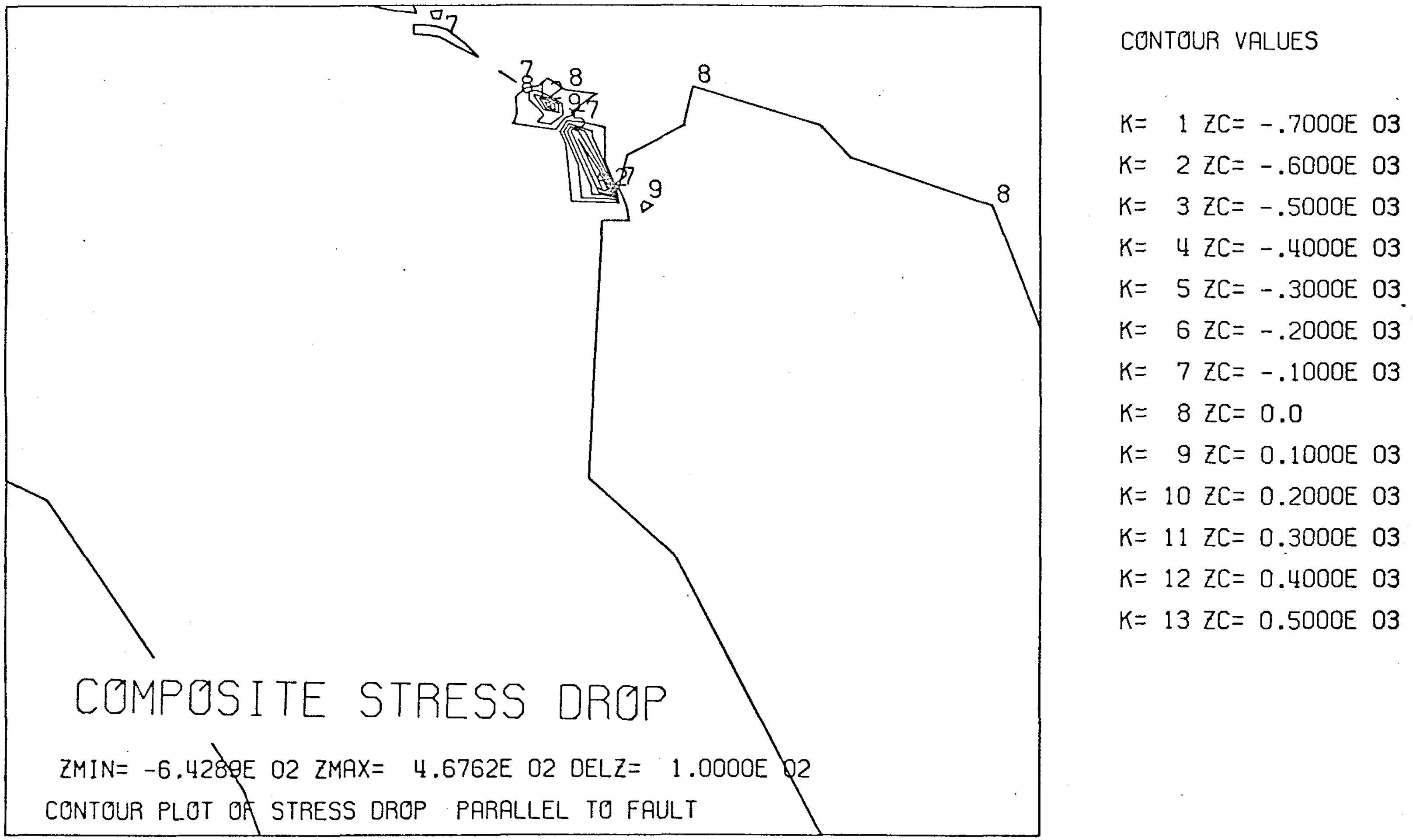

Figure 33. This composite stress drop is a combination of the two plots of Fig. 32. Maximum values are from the relaxation and the contour shapes are from the dislocation.

Evolution with time of relative displacements and stress drop

In this section, we will investigate the growth of the San Fernando fault by analyzing static equilibrium solutions. With the prestress field of Figure 29 as a starting model, equilibrium static solutions are computed for eight different models involving sequential relaxation of elements 1 through 9 (1, 1+2, 1+2+3, etc.). Since all transient effects are ignored here, these solutions will not in a true sense give a picture of the time history of the fault propagation. However, some clear understanding of what these various static solutions mean can be obtained from consideration of the elastic displacements in the near field of a propagating fault.

In Haskell (1969) we find explicit expressions of the components of displacement for a shear fault in an infinite space. In particular, with

$u_i^{(j)}(x, t)$: the elastic displacement component i, computing at time t and at a point of coordinates x caused by the component j of the fault offset

$\Delta u_j(t)$ = fault offset

α = P-wave velocity

β = S-wave velocity

S = area of the fault already broken

$\underset{\sim}{\xi}$ = coordinates of point of integration on the fault

r = $\left|\underset{\sim}{x} - \underset{\sim}{\xi}\right|$ distance of observation point to fault integration point

$f(\gamma)$ = function of direction cosines; puts a weight on the amplitude of $u_i(j)$ and can be taken here as constant for each i and j set v = velocity of crack propagation

we can evaluate Haskell's formulae for the purpose of defining the relative importance of the static solution. For a fault with only one direction of offset in its plane (either pure shear or pure thrust) we have only six expressions for $u_i^{(j)}$. They differ only by a factor $f(\gamma)$ which corresponds to the radiation pattern. Thus we can write quite generally

$$u_i^{(j)}(\underset{\sim}{x}, t) = \frac{\beta^2}{4\pi}\iint_S f_1(\gamma)\left\{\frac{30f_2(\gamma)}{r^4}\int_{r/\alpha}^{r/\beta}\Delta u_j(\underline{\xi}, t-t^1)\, dt^1\right.$$

$$+\frac{12f_2(\gamma)}{\alpha^2r^2}\Delta u_j(\underline{\xi}, t-r/\alpha) - \frac{12f_2(\gamma)}{\beta^2r^2}\Delta u_j(\underline{\xi}, t-r/\beta)$$

$$\left.+\frac{2f_2(\gamma)}{\alpha^3r}\Delta \dot{u}_j(\underline{\xi}, t-r/\alpha) - \frac{2f_2(\gamma)}{\beta^3r}\Delta \dot{u}_j(\underline{\xi}, t-r/\beta)\right\}d\underline{\xi} \qquad (4.1)$$

From Eq. (4.1) it is possible for specific values of P and S wave velocity, as well as for a specific value of the fracture velocity (i.e., position of ξ with time), to get an explicit value of $u_i^{(j)}$ as a function of the fault offset. More specifically, we want to investigate the evolution with time of a small region ahead of the failure in order to understand how much the final fault offset of the already broken region influences it (if at all) in terms of prestress. Thus for distances away from the source equal or smaller than the distance travelled by a shear wave in one second (i.e., $\left|x - \xi\right| \leq \beta(1) \cong 3$ km)

$$u_i^{(j)}(\underset{\sim}{x}, \tau) \leq \frac{1}{4\pi}\iint_S\left\{\frac{30}{\beta^2}\int_{1/2}^{1}\Delta u_j(\underset{\sim}{\xi}, t-t')\, dt'\right.$$

$$+\frac{12}{4\beta^2}\Delta u_j(\underset{\sim}{\xi}, t-1/2) - \frac{12}{\beta^2}\Delta u_j(\underset{\sim}{\xi}, t-1)$$

$$+ \frac{2}{8\beta^2} \Delta\dot{u}_j(\xi, t-1/2) - \frac{2}{\beta^2} \Delta\dot{u}_j(\xi, t-1) \Big\} \, d\xi \qquad (4.2)$$

This means that a point near the source "sees" first the second and fourth terms of (4.2), together with some portion of the first term. They have amplitude factors of, respectively, 1/3, 1/36, and 3.3. Later, with a time delay equivalent to $[x-\xi]/(\alpha-\beta)$, the observation point "sees" the third and fifth terms, together with the last part of the mixing function of the first term of (4.2). These have amplitude factors of 4/3, 2/9, and 3.3, respectively.

In all cases, this says that in the near field, the Δu terms which contain the static solution as a limit overwhelm the $\Delta\dot{u}$ terms. But the function $\Delta u_j(\xi, t)$ has a rise time which cannot be neglected.

Let us consider only a small region ahead of a propagating crack tip. Assume the crack propagates at a constant velocity $v = 1/2\ \beta$. This means that at our point of observation $\underset{\sim}{x}$ (3 km from the hypocenter) we will have the full static information only from that portion of the fault which has attained final static offset (meaning $\Delta\dot{u}_j = 0$ and $\Delta u_j = \langle \Delta u \rangle$ static). All the observations available on rise time of a fault offset point out to small particle velocities (of the order of 1 m/sec, B. Minster, personal communication). This implies for a fault offset of 4 m, a rise time of at least 2 seconds.

Clearly, then, the full static information (contained in the first three terms of (4.2) will reach point x at times such that the fault has already propagated beyond x. As a result, a static equilibrium solution for the hypocentral region cannot give a quantitative understanding of of the fault's propagation. The successive relaxation solutions can give us only the final equilibrium displacement and stress field that would be present if the fault had stopped propagating.

Then, a contrario arguments can lead to a qualitative understanding of why it did not stop. On the other hand, these solutions, because of the superposition principle, give the contribution to the final static field of each of the fault segments (assuming, of course, that the relative displacement does not overshoot the equilibrium position during the fault propagation).

Looking at the size of the elements relaxed, we can have an idea of the time "delay" involved between each calculation. Taking a crack velocity of 2.5 km/sec as a reasonable estimate for the average over the fault width, we get the following:

Element 1 is broken 0.4 seconds after the onset of failure.

Elements 1 and 2 are broken 1.4 seconds after the onset.

Elements 1 to 3 (defining the hypocentral region) have ruptured after 2.04 seconds.

Then we assume that some short time after that the failure restarts in the upper portion with the following travel times:

0.44 sec through element 4,

0.88 sec through elements 4 and 5,

1.32 sec through elements 4 to 6,

1.96 sec to break elements 4 to 7, and

3.16 sec to break elements 4 to 8.

If the knee of the fault broke without significant offset, we get a total travel time of the failure from the hypocentral region of 6.82 seconds.

The difference between two of the successive travel times given above is an approximation of the time delays between each of the contour plots shown below.

Figures 34 and 35 show the horizontal displacement caused by relaxation of elements 1 to 8 (number 6, for example, means that all six elements numbered 1 to 6 in Figure 28 are relaxed together in a prestress environment equivalent to the one in Figure 29). The hypocentral region is represented by sequence 1 to 3. In these positive contour values indicate a relative displacement to the left of the figure (south). Figures 36 and 37 show the corresponding vertical displacements.

Considering both relative movements together shows that at the onset of failure (plot numbered 1), the net maximum fault offset is less than 40 cm. The next two steps show a maximum fault offset growing to 4 m, the value it will have at the end of the faulting.

Step 2 shows that the significant thickness of the elements relaxed causes some dilation. At this stage the horizontal component of offset is greater than the vertical, giving the slip vector a smaller dip than the fault plane. This is corrected in the third step.

Steps 4 through 8 involve the relaxation of the upper portion of the fault under a prestress field onto which has been added the hypocentral relaxation. Throughout this process, the static displacement field in the hypocentral area remains practically unchanged even though it was not locked, implying that the movement of the upper portion does not change the stress field at depth sufficiently to create further movement.

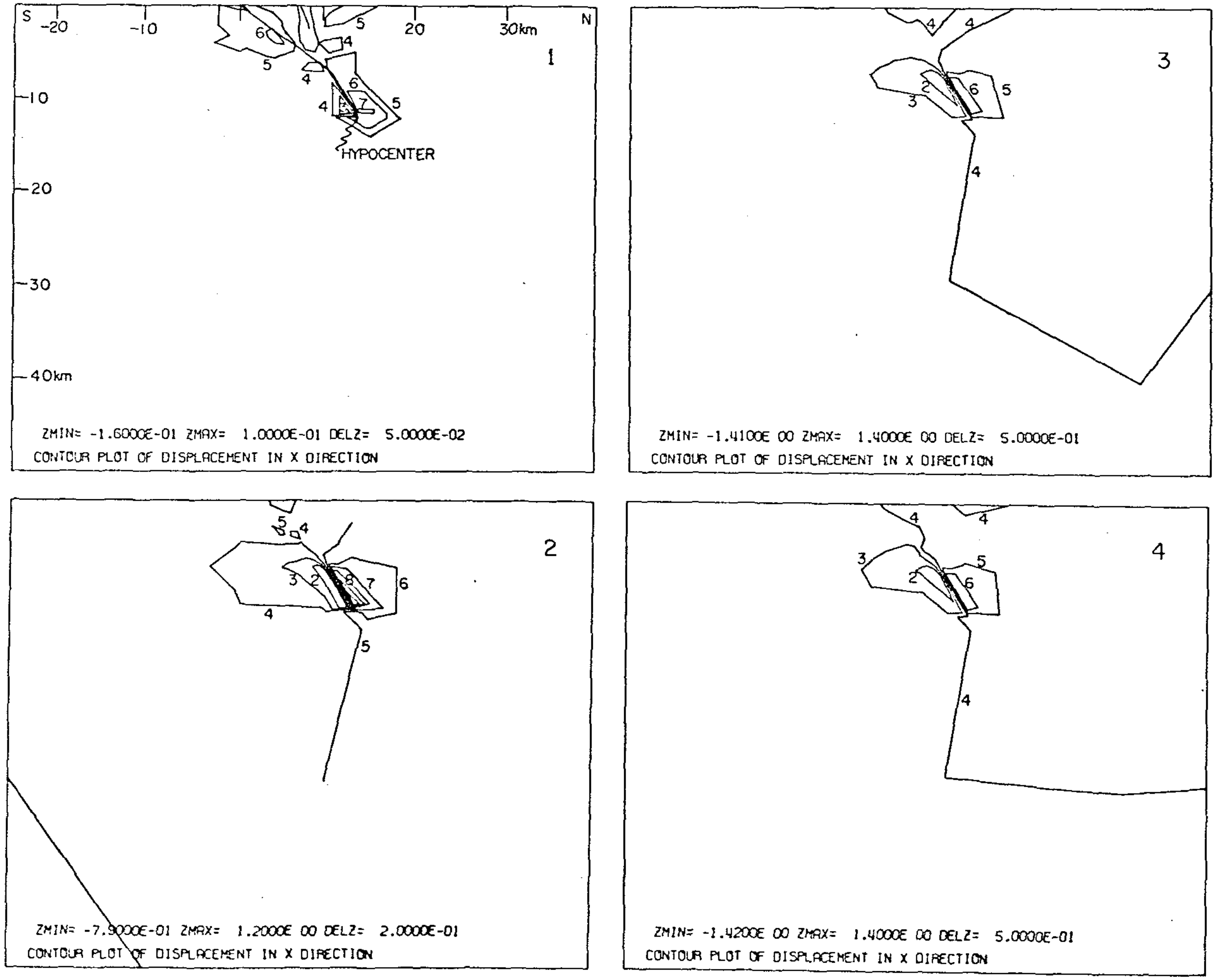

Figure 34. Evolution of the horizontal relative displacements with increasing fault width. Units are meters. Contour values for plot 1 are from -15 cm (2) to 20 cm (9), with increments of 5 cm; for plot 2, from -60 cm (2) to 120 cm (11) with increments of 20 cm.

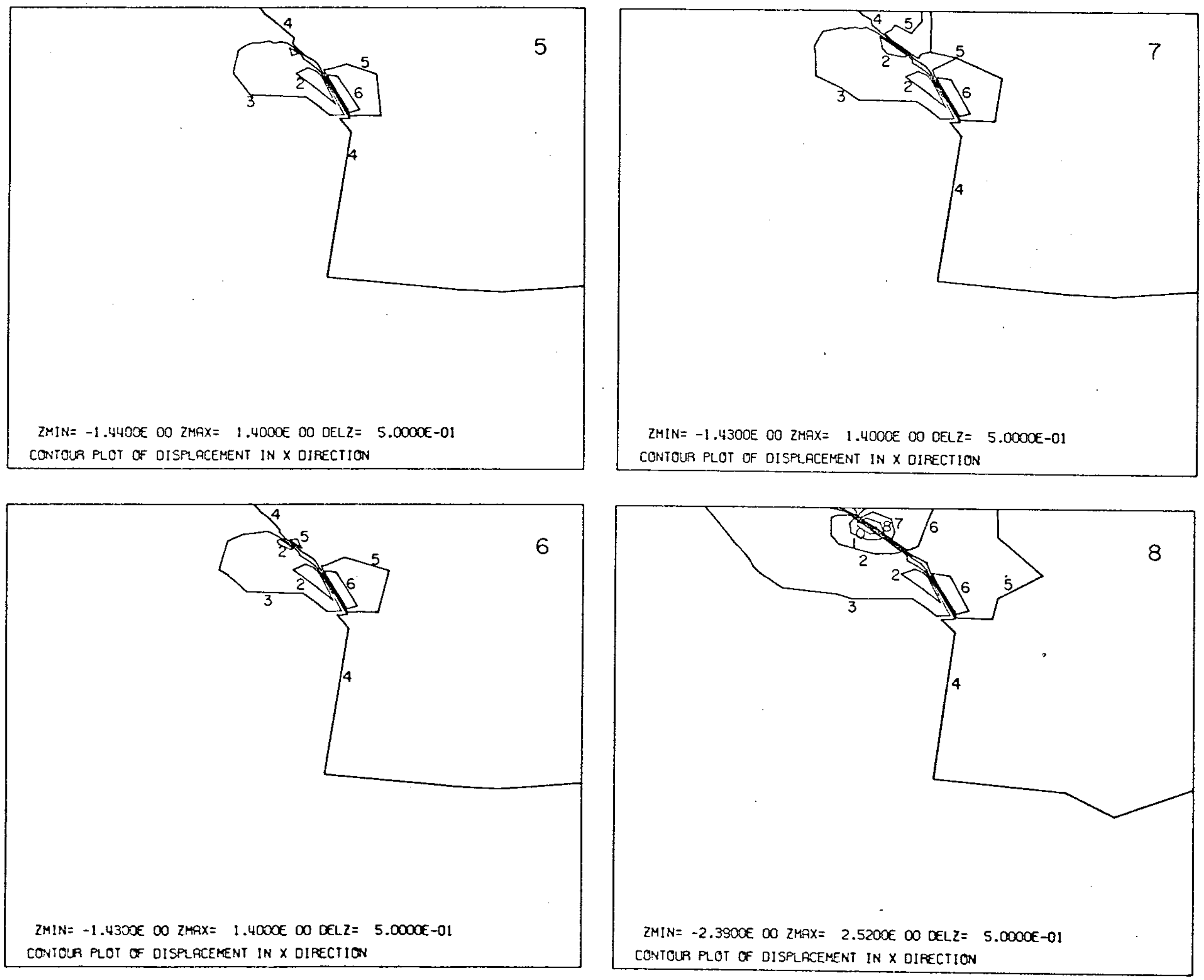

Figure 35. Evolution of the horizontal displacements for the upper portion of the fault. Units are meters. Plots 3 to 7 have contour values from -1 m (2) to +1 m (6) with 50 cm increments. Plot 8 has contour values from -2 m (2) to 2.5 m (11) with same increments.

The fault offset on the upper portion of the fault grows according to the amount of relaxation allowed in elements 4 to 8. Since these were estimated with the intent of getting the observed vertical uplift at the free surface, it is not surprising to find a maximum offset at step 8 of 5.5 m. The final relaxation involving elements 9a and 9b results in a maximum offset of over 8 m. Each of these relaxations was controlled by the initial prestress field modified by the relaxation of the previous steps.

The next two figures (38 and 39) show the evolution of the shear stress change (equilibrium solution) caused by the eight step process discussed above. The shear stress is computed at a dip of 40° giving a value for the stress drop roughly parallel to the fault plane.

Step 1 shows that the hypocentral region relaxed a maximum of 273 bars (or about 30% of the available prestress) without stressing up the region ahead of it. Steps 2 and 3 show that if the relaxation at the hypocenter is increased by at least a factor of two, the knee of the fault gets a stress increase of 250 bars. The following steps do not modify the hypocentral region where the maximum stress release remains at a level of 640 bars. While the stress drop in the upper part of the fault remains well below 100 bars, step 4 through step 8 continue the stressing up of the fault's knee to a final stress increase of 390 bars. This is shown in Figure 40. It compares the final change in the stress field, seen as a change of shear stress quasi parallel to the fault and as a change in maximum principal shear stress.

These two figures are not identical for obvious reasons. If we express the stress tensor of the prestress field, it can be written as

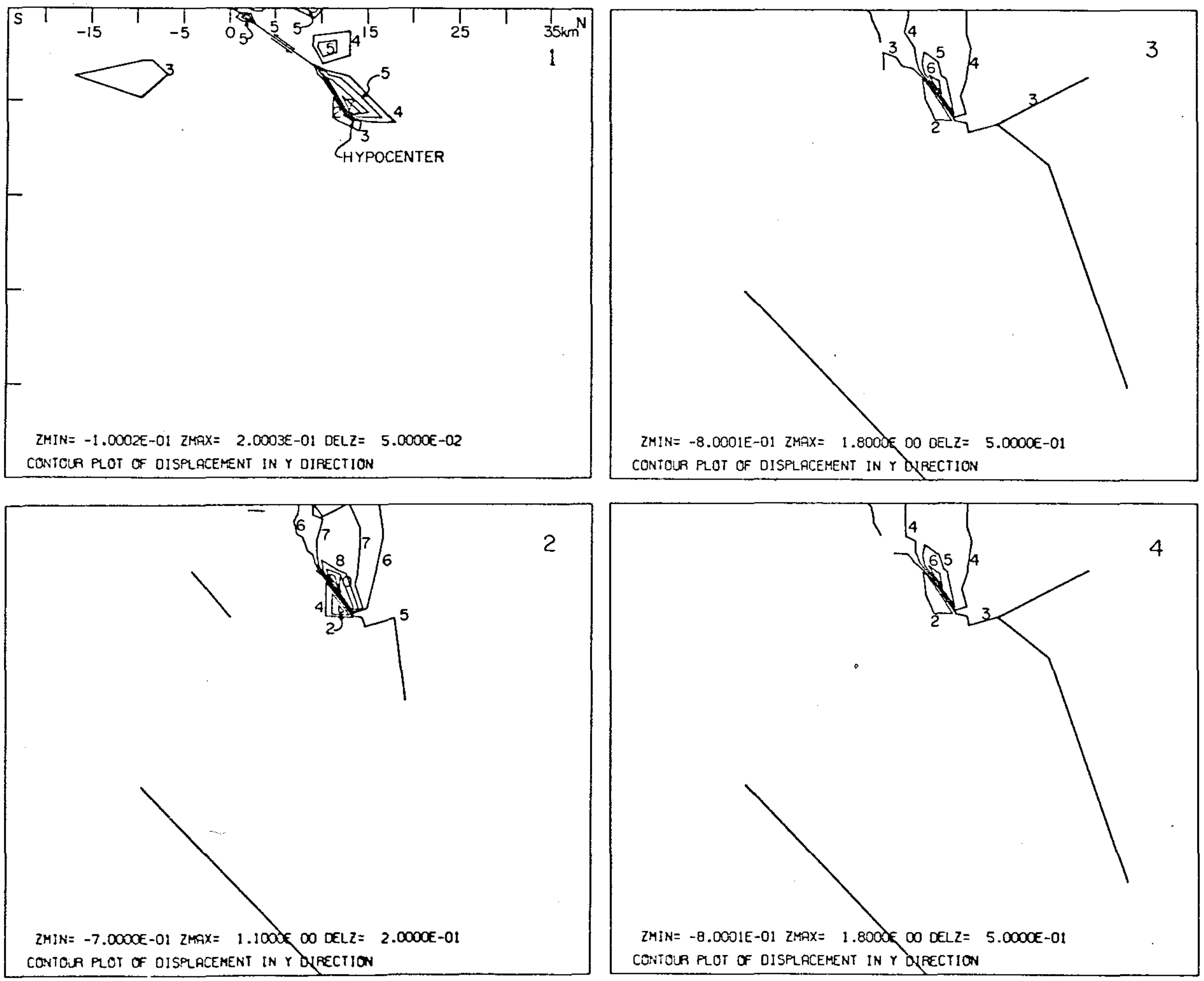

Figure 36. Evolution of vertical relative displacements. Plot 1 has contour values from -10 cm (2) to +20 cm (8). Plot 2 has contour values from -60 cm (2) to +1 m (10).

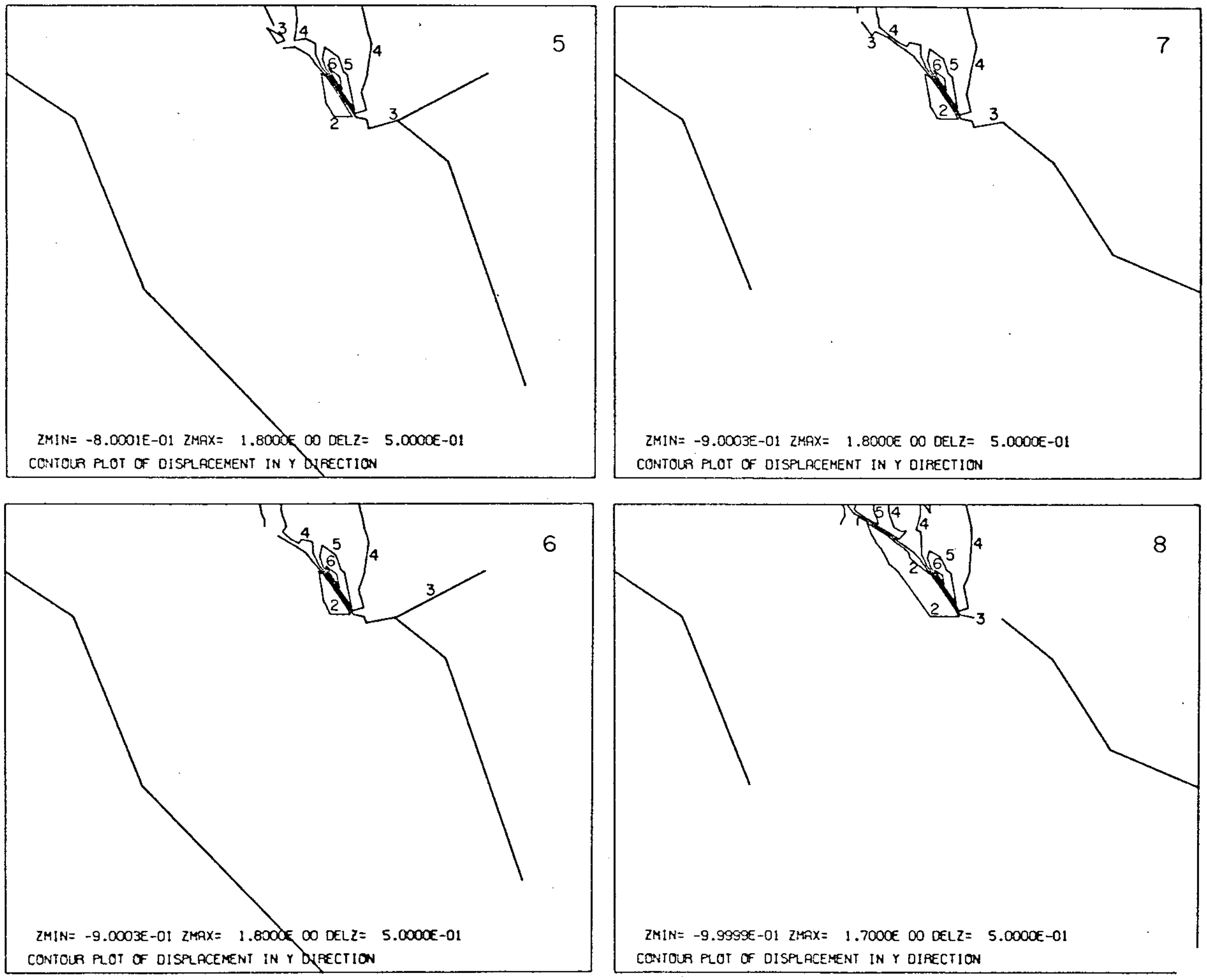

Figure 37. Evolution of vertical relative displacement for the upper part of the fault. Plots 3 to 8 have contour values from -50 cm to 1.5 m.

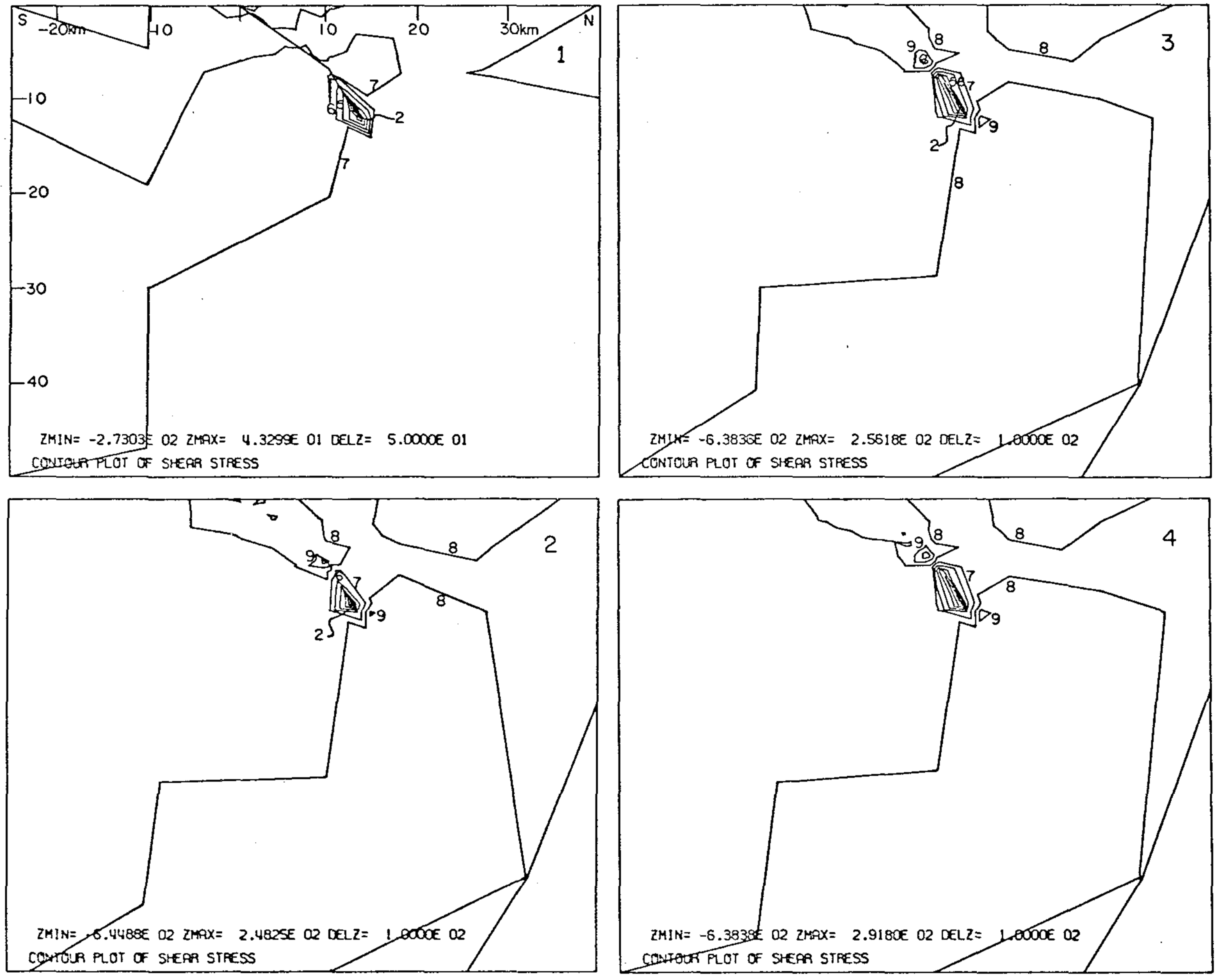

Figure 38. Evolution of shear stress change parallel to the fault. Plot 1 has contour values from -250 bars (2) to 0 bars (7). Plot 2 has contour values from -600 bars (2) to 200 bars (10).

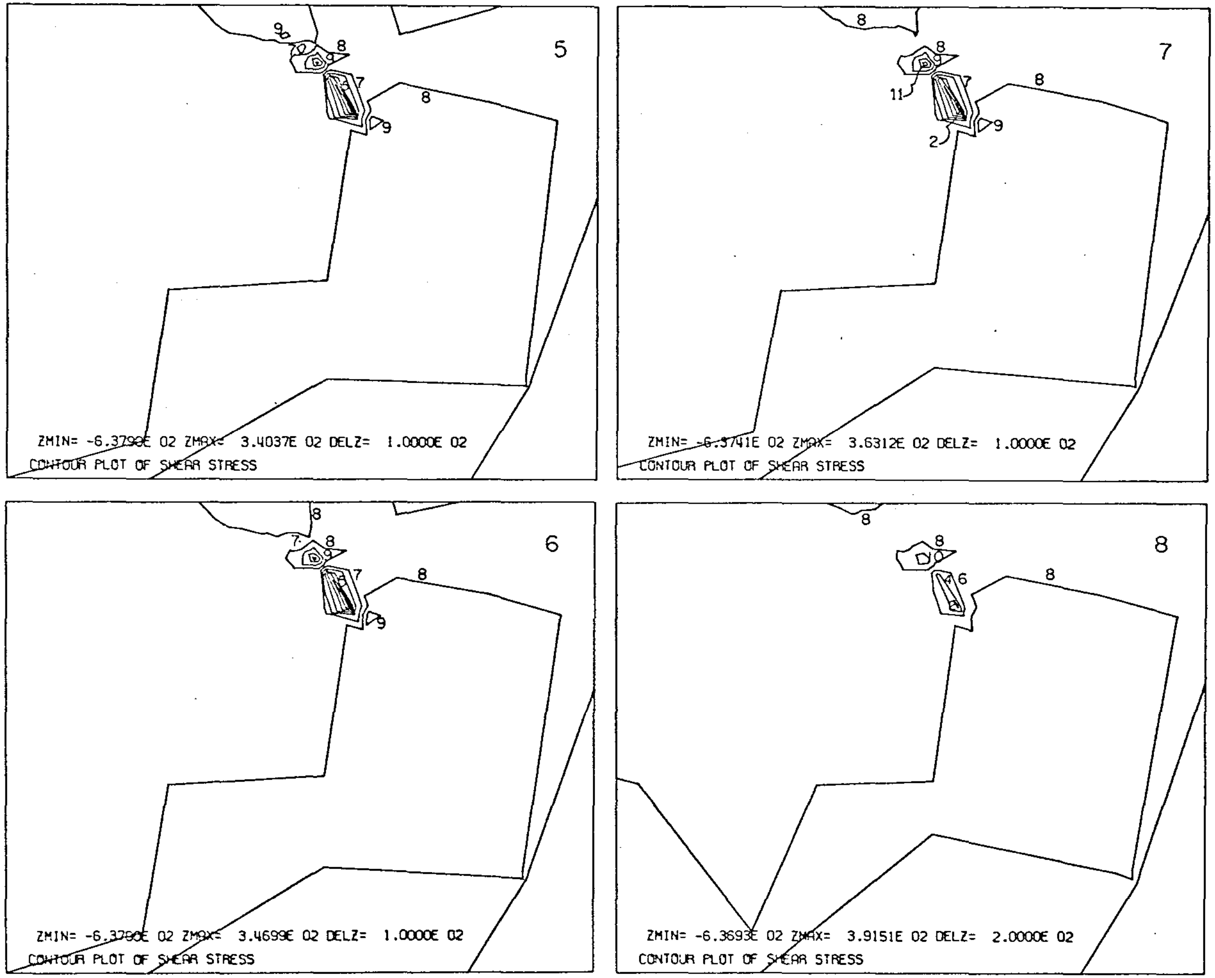

Figure 39. Evolution of shear stress change for the upper part of the fault. Plots 3 to 8 have contour values starting at -600 bars and incrementing by 100 bars (except 8 where it is 200).

(in two dimensions) for the hypocentral region,

$$\tau_{ij}^{(0)} = \begin{bmatrix} \tau_{11}^{(0)} & \tau_{12}^{(0)} \\ \tau_{12}^{(0)} & \tau_{22}^{(0)} \end{bmatrix} = \begin{bmatrix} \sigma_{max}^{(0)} & 0 \\ 0 & \sigma_{min}^{(0)} \end{bmatrix}$$

where the first matrix would be the stress distribution with one of the directions (1 or 2) parallel to the fault, and the second would be the expression of the stress tensor in the principal axis.

If the prestress field is such that the maximum shear stress is parallel to the fault, i.e., the fault makes an angle of 45° with the maximum compressive stress, then

$$\tau_{12}^{(0)} = \tau_{max}^{(0)} = \frac{1}{2}\left(\sigma_{max}^{(0)} - \sigma_{min}^{(0)}\right)$$

and

$$\tau_{11}^{(0)} = \tau_{22}^{(0)} = \sigma_{n}^{(0)} = \frac{1}{2}\left(\sigma_{max}^{(0)} + \sigma_{min}^{(0)}\right)$$

In the final state, we have

$$\tau_{ij}^{(1)} = \begin{bmatrix} \tau_{11}^{(1)} & \tau_{12}^{(1)} \\ \tau_{12}^{(1)} & \tau_{22}^{(1)} \end{bmatrix} = \begin{bmatrix} \sigma_{max}^{(1)} & 0 \\ 0 & \sigma_{min}^{(1)} \end{bmatrix}$$

where the orientation of the principal axis does not necessarily coincide with that of the prestress field. Yamakawa (1971) shows that both pairs of principal axes coincide only in two cases: (1) if the final stress is purely hydrostatic and the shear stress is completely relaxed, (2) if all components of the initial stress tensor are uniformly reduced.

As can be seen from Figure 40, this is not the case in our model. The first figure represents

$$\tau_{12} = \tau_{12}^{(0)} - \tau_{12}^{(1)}$$

while the second is

$$\tau_{\max} = \tau^{(0)}_{\max} - \tau^{(1)}_{\max}$$

A hydrostatic final stress field implies

$$\tau^{(0)}_{12} = \tau^{(0)}_{\max} \qquad \text{and} \qquad \tau^{(1)}_{12} = \tau^{(1)}_{\max} = 0$$

and a uniform reduction of τ_{ij} would imply

$$\begin{bmatrix} \tau^{(1)}_{11} & \tau^{(1)}_{12} \\ \tau^{(1)}_{12} & \tau^{(1)}_{22} \end{bmatrix} = \begin{bmatrix} c\tau^{(0)}_{11} & c\tau^{(0)}_{12} \\ c\tau^{(0)}_{12} & c\tau^{(0)}_{22} \end{bmatrix}$$

where $0 < c < 1.$

As we shall see in the next paragraph, we get for the hypocentral region

$$\tau^{(1)}_{12} \cong 50 \text{ bars} \qquad \tau^{(0)}_{12} \cong 750 \text{ bars} \qquad \text{or } c = 0.0666$$

and

$$\tau^{(1)}_{22} = 600 \qquad \tau^{(0)}_{22} \cong 600 \qquad \text{or } c = 1$$

Since the maximum shear is relaxed at the hypocenter, we see that for the onset of failure, at least, the final stress field is near hydrostatic. As the failure progresses towards the surface, this is less the case as shown from the increasing differences between the two plots.

The maximum shear stress remaining after the major shock is shown in Figure 41. It shows that the shear stress concentrations generated by the San Fernando earthquake would be, according to this model, at the knee of the fault and at the tip of the rupture below the hypocenter. It would be in the neighborhood of 800 bars in both these regions. A three-dimensional model would place additional stress

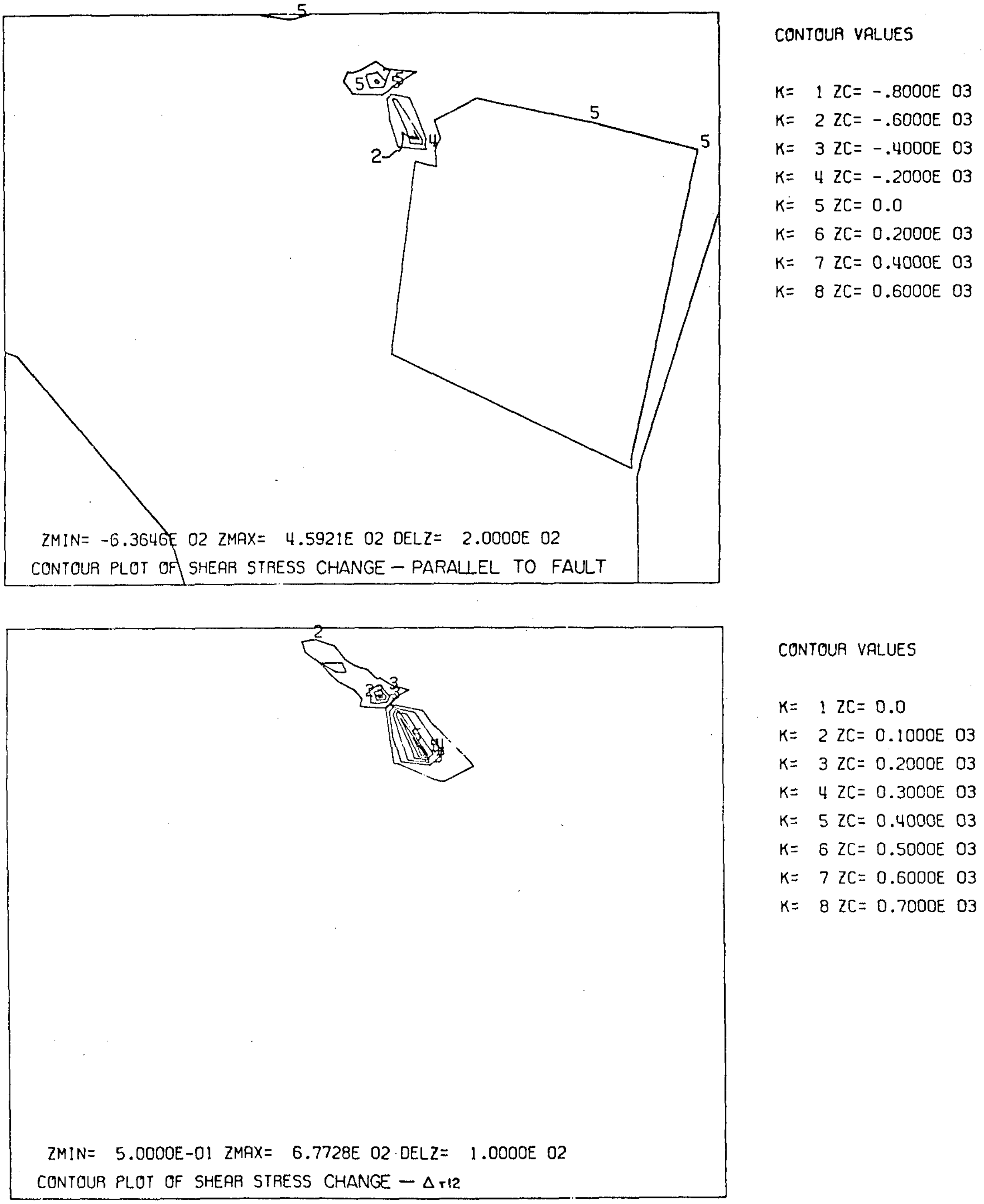

Figure 40. Comparison of the final shear stress change parallel to the fault with the change in maximum shear stress (Fig. 29 minus Fig. 41).

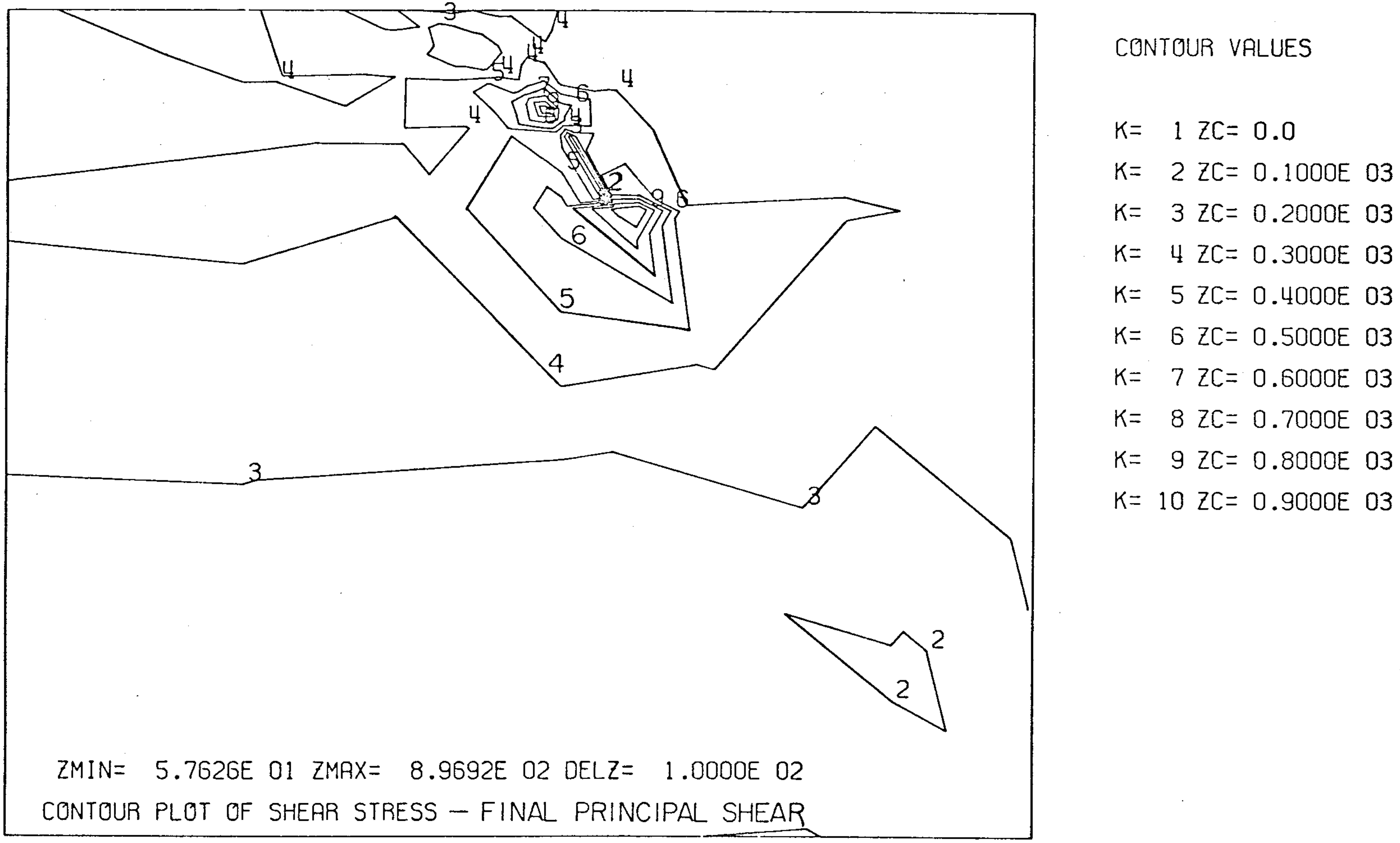

Figure 41. Final maximum shear stress field, showing the stress concentrations that result from the "relaxation".

concentrations all around the fault boundaries, similar to the one below the hypocenter.

Following the accepted idea (e.g., Mogi, 1962) that aftershocks must result from stress increases produced by the main shock, we suggest that they will be found in this event at the knee of the main fault (i.e., above and to the south of the main shock) immediately below the hypocenter and at the lateral boundaries of the rupture plane.

Summary of the fault mechanism

Since the model discussed above has given us a prestress field as well as a stress drop which vary considerably along the fault width, we can make a reasonable attempt at understanding the failure processes involved in this event.

Assuming that the prestress field that we investigated is the critical stress as defined in fracture mechanics, we can test our model against the failure criteria applicable to frictional sliding or brittle failure. Since we get the stress field relevant to a small region of the fault, a direct comparison can be made with laboratory experiments in an attempt to explain the San Fernando failure in a self-consistent manner.

Of the current fracture criteria, it appears that Coulomb's criterion predicts most of the laboratory experiments of sliding friction. Byerlee (1971, Penrose Conference) showed that experimental data for rocks scatter about two straight lines

$$\tau = 0.85\,\sigma_n \qquad \sigma_n < 2000 \text{ bars} \qquad (4.3)$$

$$\tau = 500. + 0.6\,\sigma_n \qquad \sigma_n > 2000 \text{ bars} \qquad (4.4)$$

where τ and σ_n are the shear and normal stresses measured in bars. The first equation is relevant for the San Fernando earthquake and can be viewed as either Mohr's criterion $\left(\tau = f(\sigma_n)\right)$ or Coulomb's criterion with a zero shear strength.

Figure 42 shows the variation along the fault surface of both the shear stress parallel to the fault and the compressive stress perpendicular to it. The upper plot in the figure shows the prestress relevant to the failure criterion. The region covered by distances on the fault plane from 12 to 18 km represents the hypocentral area, dipping at 52°. For that angle, we can see that Eq. (4.3) is satisfied and the medium should fail.

To get an idea of the material strength implied by these numbers, we can apply Griffith's criteria. Griffith showed that, provided $\sigma_1 \neq \sigma_3$ and $3\sigma_1 + \sigma_3 < 0$ (where σ_1 and σ_3 are the principal stresses in plane strain), the critical tensile strength of the material is defined as

$$T = \frac{(\sigma_1 - \sigma_3)^2}{8(\sigma_1 + \sigma_3)} \qquad (4.5)$$

Since at the hypocenter, the stresses are approximately

$$\sigma_1 \cong -1500 \text{ bars}$$

$$\sigma_3 \cong 350 \text{ bars}$$

we get T = -372 bars, which is much lower than the actual shear stress applied. However, McLintock and Walsh (in Mogi, 1972) modified Griffith's criterion in order to take into account the fact that in a compressive stress field, Griffith's cracks close up and support an additional shear stress. Their critical shear strength is defined as

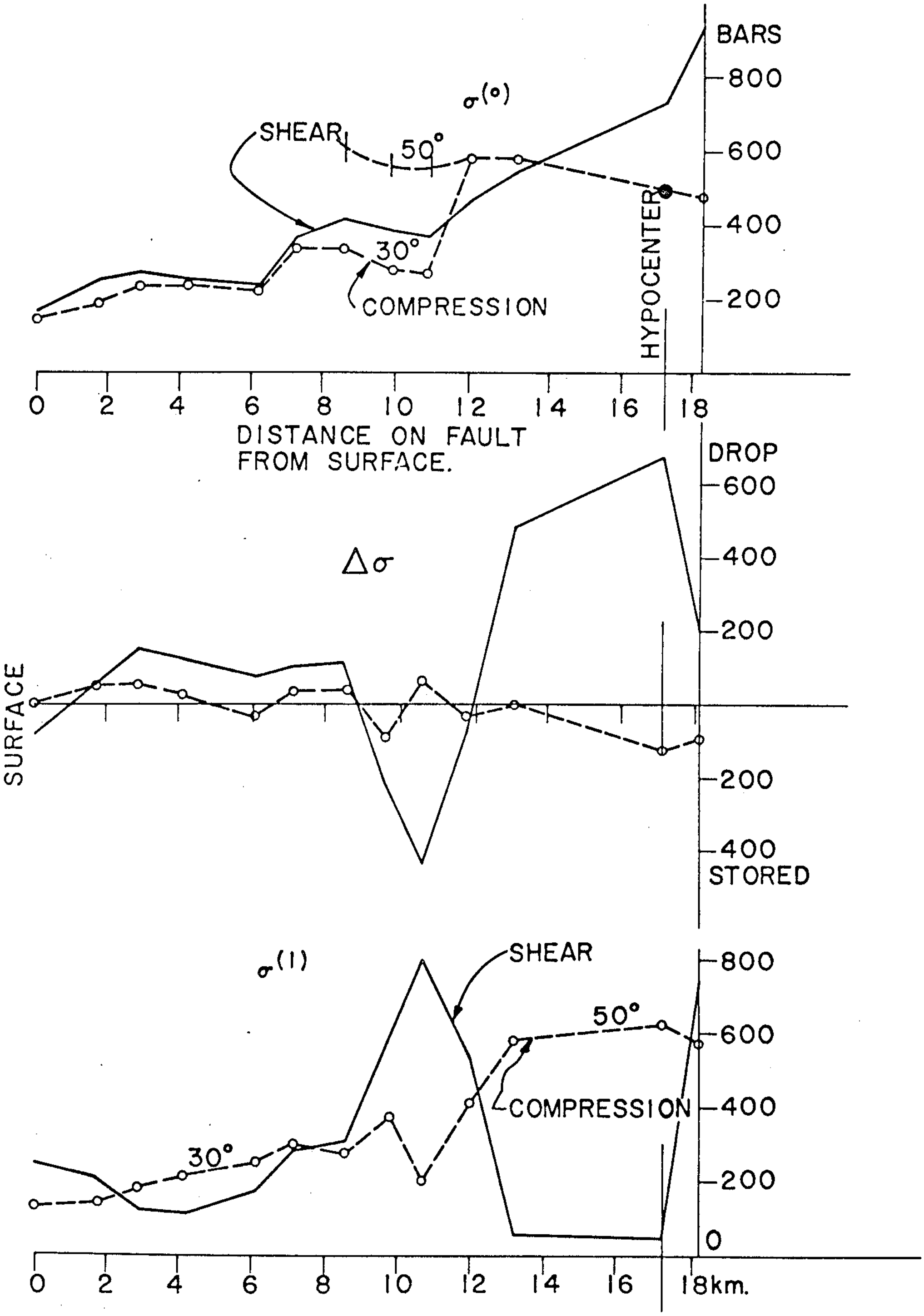

Figure 42. Comparison of shear stress parallel to the fault with normal compressive stress.

$$T_o = \frac{1}{4} \quad (\sigma_1 - \sigma_3)\,(1+\mu)^{1/2} + \quad (\sigma_1 + \sigma_3) \tag{4.6}$$

where μ is the coefficient of sliding friction. Using 0.8 as a typical value of μ (Byerlee, 1967), we get

$$T_o = -850.\ \text{bars}$$

which is close enough to the shear prestress at the hypocenter (18 km from the surface measured along the fault). Thus, the shear prestress involved in our "best" model is consistent with a critical stress as given by the modified Griffith criterion. This defines a brittle failure in two dimensions, and can be used to our model against laboratory measurements.

Accepting our numbers for principal prestress as representative of middle crust in situ, we get for the compressive strength

$$\sigma_1 - \sigma_3 = -1850\ \text{bars} = 27,195\ \text{k psi/in}^2$$

and confining pressure (here tensional because of the assumed creep at depth)

$$\sigma_3 = +350\ \text{bars} = -5.145\ \text{k psi/in}^2$$

A value of compressive strength near 2 kbar is quoted by most authors for materials such as granite and quartzite (e.g., Mogi, 1972).

Clearly we cannot improve these values since our models are two-dimensional, and we have no control on the intermediate stress, which by virtue of plane strain assumptions is perpendicular to our cross section and equal to

$$\nu(\sigma_1 + \sigma_3) \cong -276\ \text{bars compression}$$

where ν is the Poisson's ratio. However, we can conclude at this stage that we have successfully modeled the hypocentral region in a way which is self-consistent with:

(1) the observed vertical displacements at the free surface

(2) the interpretation of the Pacoima Dam accelerogram which requires a large hypocentral offset (Hanks, 1972)

(3) the laboratory experiments of brittle failure in materials such as those we might expect below the San Gabriel Mountains.

We will now apply the same principles to the upper portion of the fault to see if the models remain consistent in terms of failure criterion and material strength.

As can be seen in Figure 42, as the fracture propagates toward the surface, it rapidly reaches a region where the shear stress is considerably less than the compressive prestress. This is what we called the knee of the fault where it curves toward a 30° dip. The prestress at that dip, however, is such that Coulomb's failure criterion is once again satisfied, and the upper portion of the fault can fail.

The stress drop plots show that the compressive stress essentially did not change (which satisfies the stick slip failure hypothesis), and the major area of stress relaxation is near the hypocenter. It also shows that once equilibrium is attained, the knee of the fault stores a very significant amount of shear stress. As was pointed out earlier, the kinematics of failure are such that this stress buildup may have reached critical values some time after the fault had already reached the free surface. This could explain why this particular portion of the fault did not fail during the main shock.

If this is true, the last part of the figure shows that the final stress state is such that Coulomb's failure criterion is satisfied at the knee of the fault, and we expect aftershocks to occur. The next paragraph will show that they did. Clearly this picture of the faulting processes could be modified if we considered the effects of the third dimension.

However, we pointed out in Chapter II of this thesis that plane strain assumptions led to an underestimate of the fault's offset at depth compared to the real situation of a short fault length. Larger offsets in the hypocentral region would simply increase all the stress estimates presented here. On the other hand, if the fault was modeled as curving gently from 50° dip at depth to approximately 30° near the surface, this would place the knee of the fault deeper and permit some reduction of the stress stored in this area. However, some aftershocks were found in the region surrounding the knee of the fault (Whitcomb et al, 1972), implying that our model is correct at least qualitatively, since if we modify the picture to the point where the prestress is relieved throughout the fault plane no aftershocks could have occurred there.

A three-dimensional picture of the event

In Figure 43 we drew a three-dimensional perspective view of the observed surface uplift. The data are those of Chapter II, corrected for the epicentral area using the latest gravity measurements of Alewine (personal communication). The cross sections AA' and BB' treated in Chapter II are shown in their relationship with the overall uplift.

The second part of the figure is a simplified, highly speculative perspective view of the fault at depth. On sections AA' and BB' at depth are drawn arrows indicating the amount of thrust (relative offset) as determined by inversion of the uplift data. These arrows are scaled so that they are proportional to the values quoted in Chapter II (Fig. 17). At the junction of the Tujunga and the Sylmar segments, we placed a step in the fault plane. This step dies out with depth from the measured amount near the surface to zero at the point where the plane bends to a steeper dip.

This shows that the width of the Tujunga segment is approximately 1.5 km greater than that of the Sylmar segment. This explains, in part, the discrepancies between section AA' and BB'. However, if the offset of the step is constructed by assuming that the relative displacement is constant over the length of both segments, it results in a large gradient of displacement over the surface of the step which cannot be explained by the difference in width or by the possible lateral variations of geology. Multiple faulting near the surface can reduce this problem considerably, but is highly nonunique in terms of number of small faults and the offsets they carry.

This problem can be avoided if we assume that the offsets of section BB' are reduced as we move west along the fault length and those of section AA' are increased as we move east so that the offsets are equal as they reach the hanging wall. If this is the case, this will occur in a rather narrow region around the step since the observed uplift changes rather rapidly between the two fault segments.

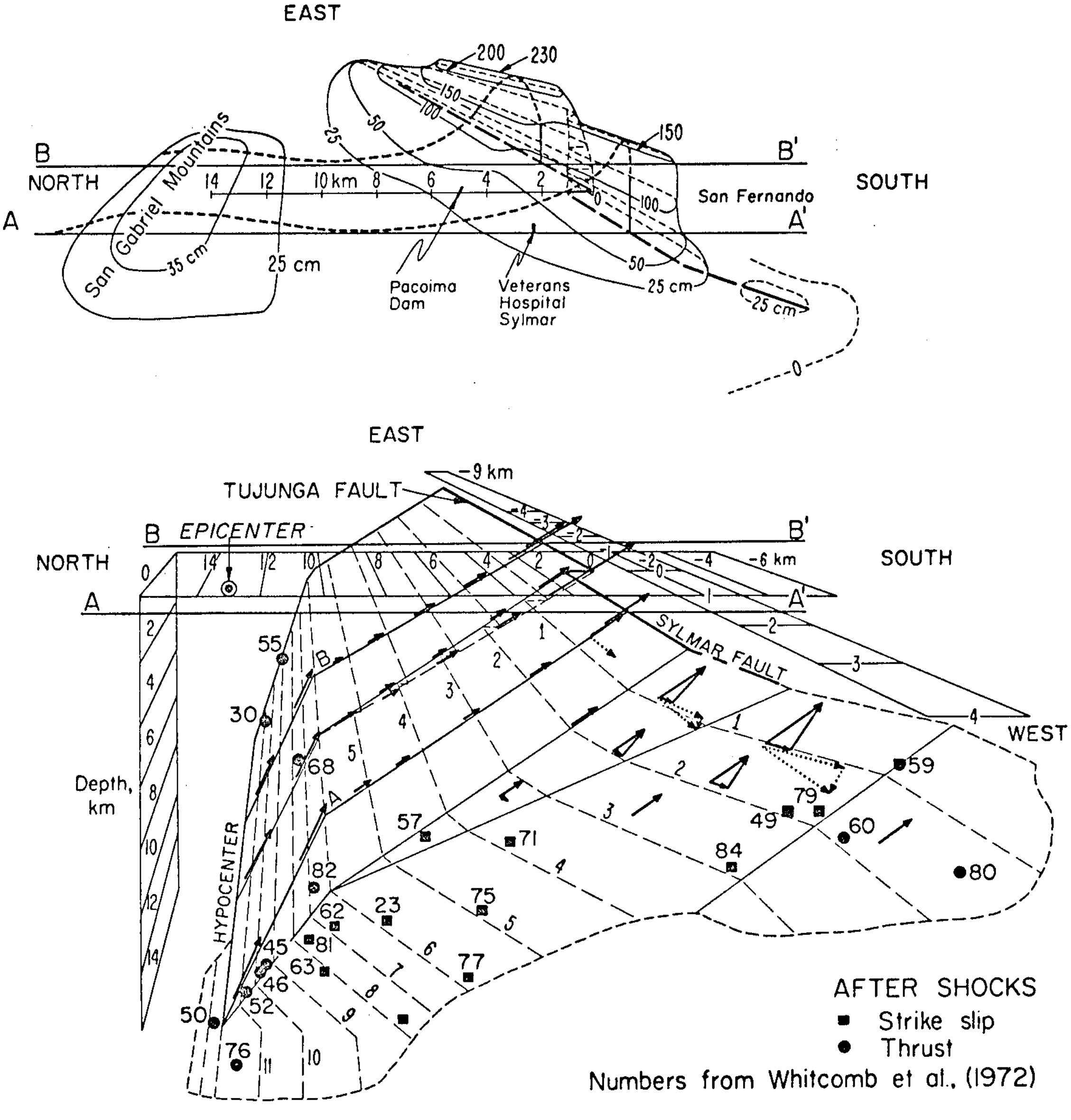

Figure 43. Three-dimensional perspective of the observed vertical movement at the free surface and composite interpretation of the fault plane at depth.

On the basis of aftershock analyses (Whitcomb et al., 1972), and from the trend of the western portion of the Sylmar segment, the westernmost part of the fault (toward the observer in Fig. 43) is assumed to be a series of planes which are closer and closer to the vertical. The two extreme ends, to the southwest near the surface and to the west near the hypocenter, are shown as thrust planes. They are postulated by Whitcomb (personal communication) on the basis of a series of aftershocks which had a thrust fault plane solution.

Most of the major aftershocks were drawn on the figure with their determined hypocentral location. The numbers assigned to them are from Whitcomb's classification. They are listed with their magnitude and depth determination in Table 4.

A square indicates a strike slip fault plane mechanism and a circle, a thrust. Aftershock 53 has the characteristics of both strike slip and thrust, thus it is shown in a place where the fault plane changes from mainly vertical to a dip of about 30°.

Aftershocks such as 50 and 76 confirm the stress increase below the hypocenter of the main shock and 82 and 68 confirm the interpretation of our final stress field at the knee of the main fault plane. Their relatively small magnitude compared to the stress available to them (up to 700 bars) can be argued by considering the plot of strain energy change after the main shock (Fig. 44). As can be seen the area of stored strain energy density is rather small compared to the size of the region exhibiting release. Furthermore, as was pointed out earlier, this model could be viewed as enhancing the fault's knee effect. Thus, from the point of view of strain energy available to the aftershocks, it can be argued that they have the size (magnitude-wise) necessary to release the stress stored in that area.

All of the other shocks shown here besides those can be interpreted as fault end effects. The strike slip aftershocks which cluster along the westerly panel can be explained by considering the strike slip component of the main shock. A vector construction shows that because of the change in slope, the thrust vector of section AA' can be transferred onto the western panel with a significant strike slip component. A hypothetical strike slip on section AA' could be transferred in the same manner and result in a significant thrust component of opposite direction. It is easy to envision how the proper mixing of both would result in a strike slip focal mechanism for the aftershocks such as 84, 79 or 49, etc.

The energy released

Let us assume that our representation of the San Fernando earthquake is the correct one. Let us assume further that our section BB' represents the length averaged behavior of an earthquake with the same energy balance of the total San Fernando earthquake. Let that imaginary event have a length of 10 km over its entire width. Then we can apply the techniques of Chapter III in order to get the energy relationship of the San Fernando earthquake.

Going back to Figure 44, we can show that a major portion of the strain energy released by the faulting came from the hypocentral area. There, we find a maximum change in strain energy density of 0.58×10^{21} ergs/km^3. Some strain energy was released near the free

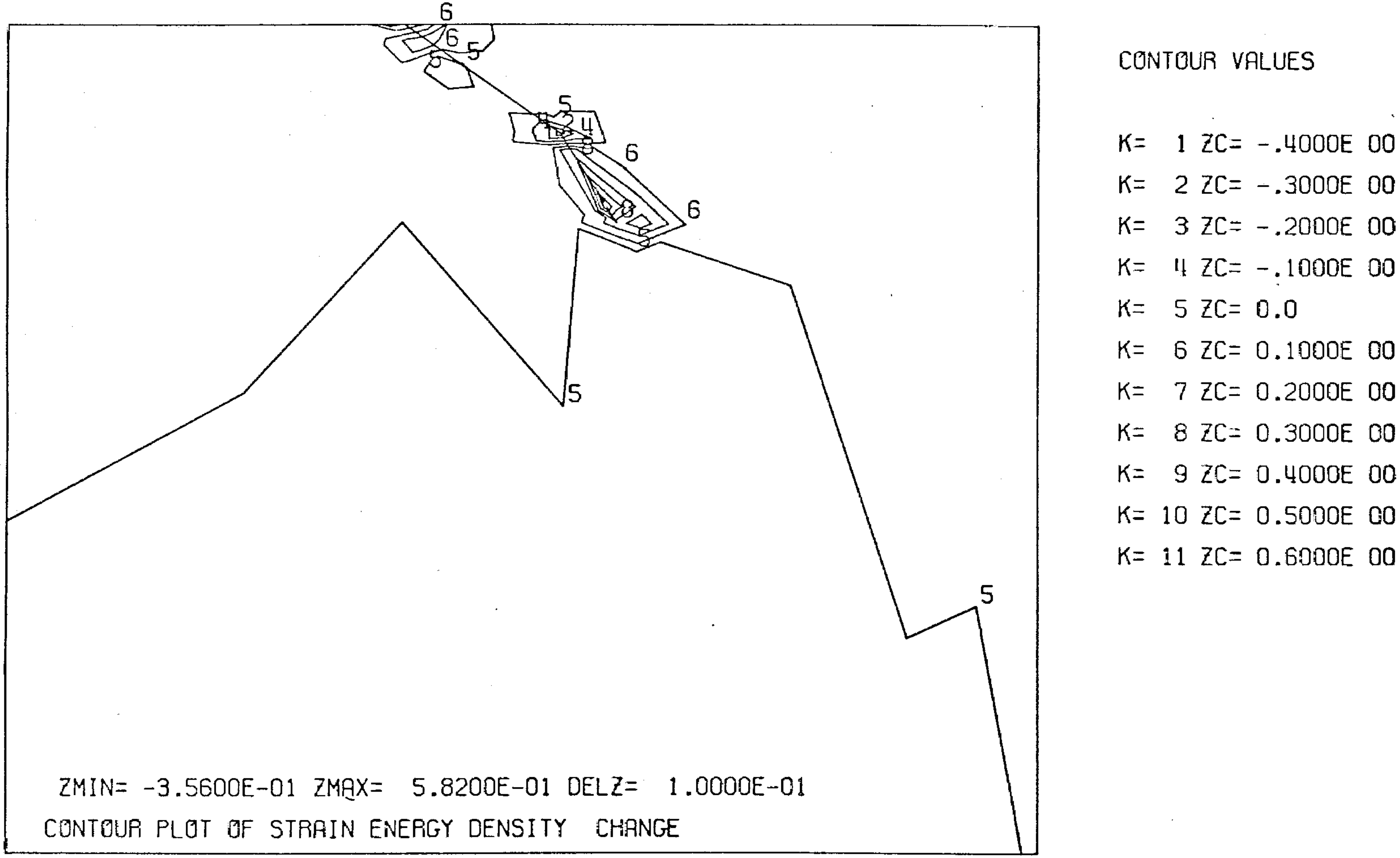

Figure 44. Final strain energy density change. Shows the area where energy is available for aftershocks.

TABLE 4

Aftershock Number	M_L	Depth
23	4.2	6.
30	3.5	11.3
33	3.2	8.
45	3.4	9.5
46	3.9	9.2
49	3.8	1.1
50	3.9	12.9
52	3.4	9.7
53	3.5	.6
55	3.1	10.
57	3.2	4.4
60	3.6	6.8
62	4.5	7.2
63	3.4	4.9
68	3.5	7.5
71	4.5	3.2
75	4.3	4.6
76	3.3	11.3
77	3.7	5.7
79	4.6	2.1
80	3.4	6.3
81	4.2	7.1
82	3.2	7.9
84	4.0	3.0

From Whitcomb *et al*. (1972).

surface, but it could be argued that coming some 6 seconds after the onset of failure it probably appeared in the break out phase.

These contours, integrated over the area they encompass, define the W discussed in Chapter III for this particular model. Since the center of mass of our model went up, this strain energy released by the fault is partitioned locally into gravitational potential energy and dynamic radiations. At this prestress level, the partition is almost one to one which means that the prestress equivalent of the gravitational potential increase is equal to approximately one-half the average prestress. This is shown in Figure 45 where the model discussed above is marked (3). Because of the flexibility of the finite element technique, we can vary the prestress field while maintaining the fault offset invariant, thus mapping all possible values of δW versus prestress which would still fit the static observations. This results in the two lines shown in Figure 45. Lines A and B exhibit the linear relationship between energy change and average prestress. The others have a combination of more or less slip on the fault at depth and compressive tectonic prestress. The values quoted on the abscissa axis are averaged shear stress on the fault surface. Line A is the solution that would be obtained if the gravitational potential energy was ignored. Thus line B is the actual amount of energy available for seismic radiation.

Trifunac's (1972) estimate of near field radiated energy from the Pacoima Dam accelerogram was 1.7×10^{22} ergs. For comparison's sake with our model of a 10 km long fault we place his estimate at about 2×10^{21} ergs per km of fault length. His value is approximately twice the highest estimate of Wyss and Hanks (1972) from teleseismic body

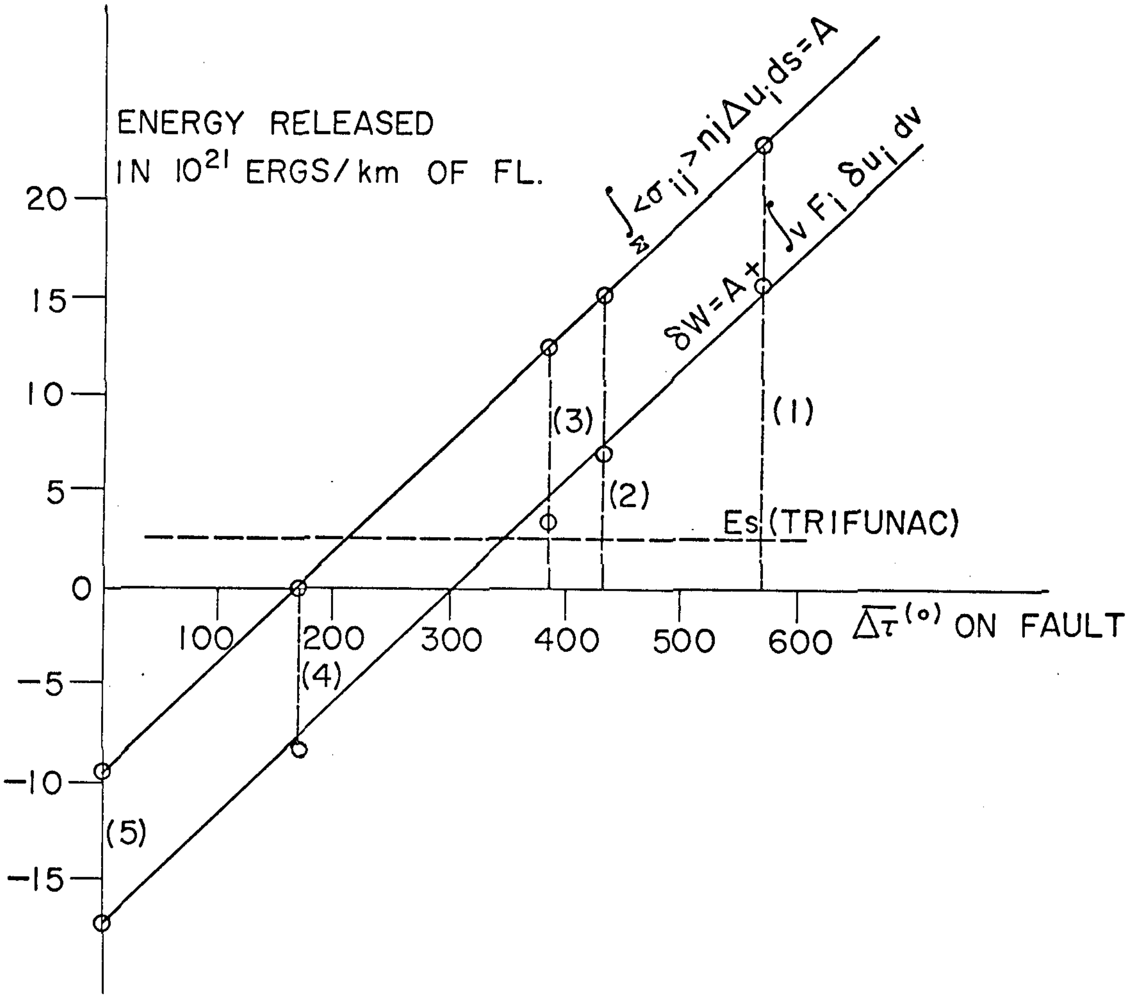

Figure 45. Energy balance for this model of the San Fernando earthquake per kilometer of fault length. Assumes a constant behavior for a total fault length of 10 km.

waves and nearly an order of magnitude bigger than E_{GR} for a local magnitude of 6.6. Thus if we assume that Trifunac's estimate is the best estimate of seismic energy we can conclude that our best model of the San Fernando earthquake is

(1) The prestress level was averaged over the fault: 350 bars

(2) The average stress drop was between 150 and 200 bars

(3) The local increase in gravitational potential was 7.5×10^{22} ergs

(4) The energy radiated was 4.5×10^{22} ergs, which compared to E_s implies a seismic efficiency of 0.4.

The value given for the average stress drop is between a factor of 10 and a factor of 5 larger than those calculated by Wyss and Hanks (1972) on the basis of empirical and theoretical formulae. This is not surprising since the parameters they used are values averaged over the fault area, and we showed previously that when the fault offset varies by an order of magnitude in space, then, moment, stress drop and related fault parameters estimates can be grossly underestimated. Even here, when values of stress drop are quoted they are only average values and are not very meaningful taken out of context. For example, our "average" stress drop of about 150 bars varies from 675 bars at the hypocenter to 80 bars at 4 km depth with a stress increase of up to 400 bars at the knee of the fault. Similarly, the prestress level of 380 bars of our best solution varies from 850 bars at the hypocenter to about 200 bars near the surface.

The estimate of prestress most widely quoted in the literature is attributed to Chinnery (1964) who, upon assuming that the San Francisco earthquake of 1906 relieved the entire stress available, computed the prestress to be equal to the magnitude of stress drop. What he called the strength of the earth's crust was computed from dislocation theory and found to be 100 bars. This number may be correct for the maximum average stress drop for a strike slip earthquake in California, but it does not necessarily have much meaning. The assumption of complete stress release is open to considerable debate and it can be very misleading. As we have shown above, the stress drop can vary between, say, -500 bars and 1000 bars on a local basis.

Brune et al. (1969), upon finding no heat flow anomaly in the areas where the San Andreas fault is creeping, found that an initial prestress of 200 bars (averaged over the region they studied) could fit the observations. They assumed that all of the strain energy released by the creep was transformed into heat. The uncertainties involved, however, made them admit the possibility of a 500 bar upper limit for the average prestress.

Clearly, all of these estimates can accommodate very large local variations, and we can conclude from them that our models of the San Fernando earthquake lead to a significant improvement in terms of understanding the tectonic processes involved in thrust faulting.

The other two earthquakes we studied will show a similar pattern of large variations of stress drop along their fault surfaces confirming the fact that the finite element technique is ideally suited for earthquake modeling.

The Alaska Earthquake of 1964

Previous studies by Stauder and Bollinger (1966) of the static displacement of the Alaska earthquake of 1964 led Plafker (1970) to estimate the stress change using the values of reduction of the horizontal strain from the dislocation model. He assumed the stress strain relationship to be

$$\delta P = Ee$$

where δP is the stress change, E is Young's modulus, e is the strain change. He found a stress "drop" of 77 bars averaged over the area and a maximum of 210 bars near the axis of subsidence. His values are in fact the horizontal stress that one would get from bending a plate in pure flexion ($e = y/\rho$, where y is the distance to the neutral or unstressed axis and ρ is the radius of curvature of the plate). Thus, it is not the stress drop on the fault surface, but is instead an indication of the magnitude of stress change involved in this event. A much lower estimate of stress drop on the fault is given by Brune and Allen (1967). From Savage and Hastie's dislocation model they estimate a stress drop of 27 bars. This is clearly another example of an average stress drop value which has little bearing on the fault mechanism involved. This can be seen in Figure 46 where we show a contour plot of the stress drop generated by the "best fit" offset presented in Chapter II and computed throughout the section for a direction approximately parallel to the megathrust ($\cong 10°$ dip).

As we have said in Chapter III, the stresses computed by the numerical technique on the fault surface are an average of the stresses at the centers of the elements surrounding the nodes. For the dislocation model this results in an underestimate by approximately a factor of two (function of the width of the elements surrounding the fault plane).

With the assumption that the error is exactly a factor of two, we see that in our model the stress drop varies along the fault surface from -86 bars to +215 bars. Thus a stress drop averaged over the fault surface could indeed be very misleading.

The details of the variation of stress change are very interesting. It is found that both ends of the fault exhibit a net increase of shear stress. For the upper portion of the megathrust, this is in fact an argument in favor of our best fit solution. As we showed in Chapter II, the lack of data south of Middleton Island made the inversion for that area completely nonunique. It is easy to show that if we increased the offset near the trench, the stress change would increase in proportion and this in turn would make that region a prime candidate for aftershocks. The fact that significant aftershocks were not observed here argues for our best fit solution.

Another region of stress increase is found in that portion of the thrust where the offset function goes through a local minimum (between Montague and Middleton Islands). We have shown in the section on resolvability that this is not unique because of the lack of data between the two islands. This local stress increase, then, is not resolvable. By contrast, the central portion of the megathrust is well resolved, and we feel that the maximum stress drop of 215 bars really occurred below Montague Island. We can thus feel confident that most of the energy available for seismic radiation came from that central portion

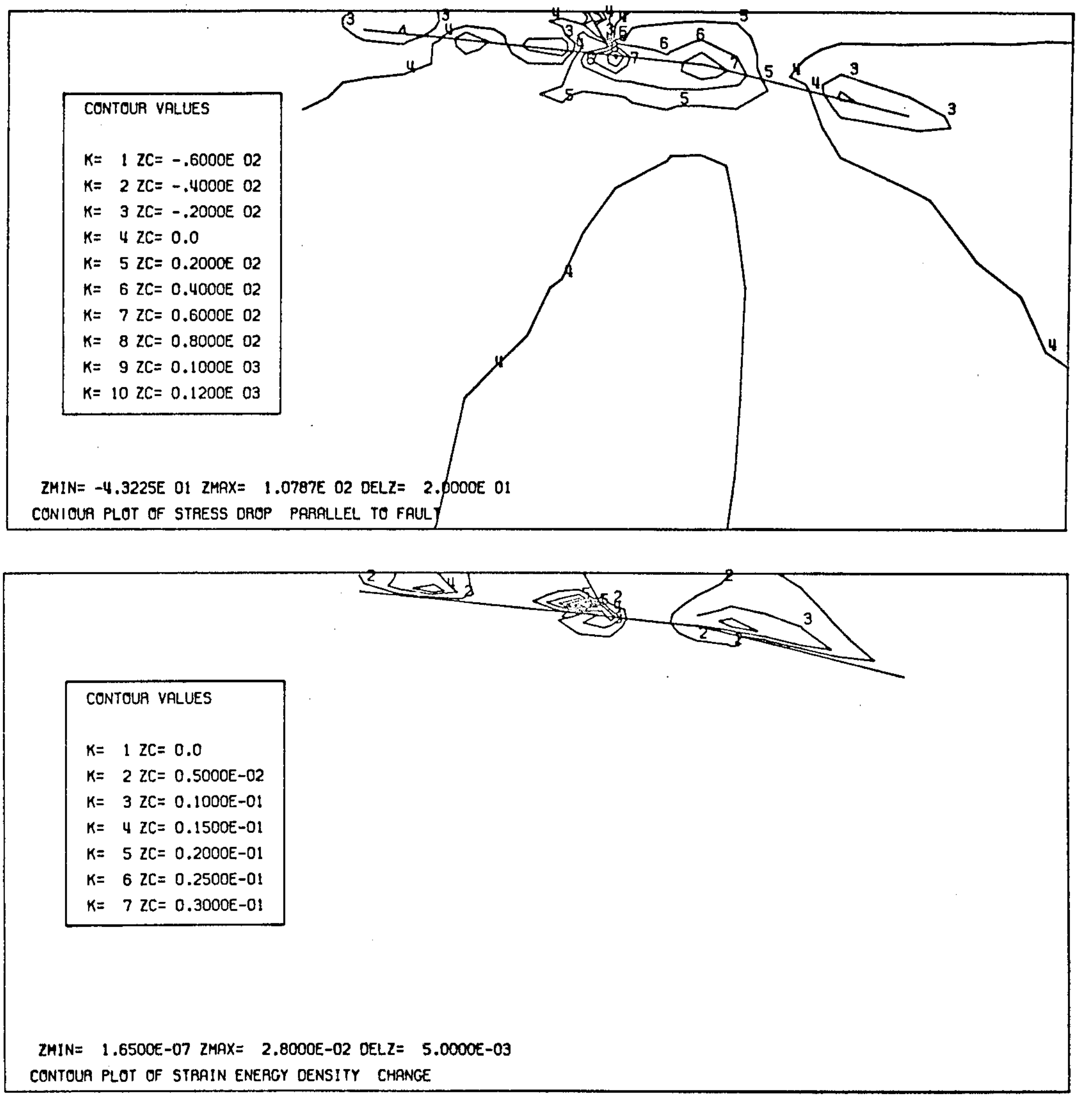

Figure 46. Stress change and strain energy released for the Alaska earthquake for an average prestress equal to the average stress drop. Units are bars and 10^{21} ergs per km^3, respectively.

of the megathrust. This can be seen from the bottom part of Figure 46 where the strain energy density change is shown to concentrate below Montague Island.

In fact, a direct comparison can be made between the strain energy density plot and the multiple rupture characteristic that Wyss and Brune (1967) found for this event. They postulate a multiple event source mechanism whereby the propagating rupture "triggers" distinct events larger than the initial rupture of the hypocentral region. The largest of the discrete events occurred on the megathrust, below Montague Island, and resulted in a delayed pulse with an amplitude significantly larger than the initial shock (up to 30 times larger). This compares very well with our estimate of a large strain energy density change of up to 0.28×10^{20} ergs/km^3 concentrated below Montague Island, while for the hypocentral region, the energy density change is only 0.02×10^{20} ergs/km^3. Thus, their dynamic model and our static analyses appear to agree qualitatively.

The prestress fields applied to the model for the energy calculations were composed of one-tenth of the material's own weight applied as a body force and a tectonic prestress. This "tectonic" prestress was obtained by specifying the displacement at the locked boundaries in the following way: the block representing the oceanic upper mantle was displaced to the right and the block representing the continental crust was displaced to the left. This was intended to model the tectonic situation described by Plafker, i.e., the Pacific plate underthrusting the Alaskan continent. The amount of displacement at the boundaries of these units was varied in order to vary the prestress field. The result is shown in Figure 47. Total energy values for the Alaskan earthquake can be obtained by multiplying the values quoted by 600, the length of the fault.

Since the released seismic energy is about 1-2 x 10^{24} ergs(log E_{GR} = 11.4 + 1.5 M) and considering that it can be an underestimate by a factor of ten or more, we estimate the prestress to have been at least 150 bars (average shear prestress parallel to the fault). For this model, the local increase of gravitational potential energy is computed to be 1.3 x 10^{23} ergs per km of fault length or a total of approximately 9 x 10^{25} ergs for the entire fault. Since this is nearly two orders of magnitude greater than E_{GR}, we can conclude that here again considerations of gravity as a local body force is critical for the energy balance of the earthquake.

The prestress field used in this study did not contain any large scale stress concentrations such as would be caused by past earthquakes or creep at depth. This is why the average prestress values used in Figure 47 should really be taken to include stresses between 100 to 1000 bars in keeping with the meaning of stress fields used throughout the thesis.

The Hebgen Lake, Montana, Earthquake of 1959

The Hebgen Lake, Montana, earthquake (M = 7.1) of August 18, 1959, produced an extensive subsidence, and in complete contrast with the San Fernando event, produced no recorded uplift. Even though some of the subsidence is attributed by Fraser et al. (1964) as secondary compaction, it is felt to be significant enough to have generated a

decrease in gravitational potential energy, which, according to Chapter III of this thesis, must have been transferred into kinematic energy or stored strain energy. Brune and Allen (1967) estimate an average stress drop of 355 bars for this earthquake. Based on averaged fault offsets and derived from an empirical formula this number is surprisingly large. Using Fraser et al. (1969) isobase map, we choose a cross section running through the center and perpendicular to the fault break. Its orientation is northeast-southwest. An elastic half space with a Poisson's ratio of 0.25 and a shear modulus of 3×10^{11} dyne/cm^2 is used. We follow Savage and Hastie's (1966) solution for this event since their 10 m average offset is the one used by Brune and Allen's (1971) stress drop calculation. In order to get a closer fit to the observations, we chose a fault width of 25 km instead of their 15. We consider two models with different fall off of the offset at the hypocenter (more exactly at the deep end of the fault since the epicenter is assigned by Savage and Hastie (1966)) to be several kilometers northeast of the northernmost fault scarp, while Savage and Hastie's solution dips 54° to the southwest. Thus, the model used in this section will not be unique by any means. It is meant only as an example of radiated energy being enhanced by gravitational potential drop. The upper portion of the fault is left as Savage and Hastie assumed it, i.e., 10 m offset at 1 km depth, no offset at the free surface. Since the fault length is 30 km while the width is only 25 km, plane strain modeling is accurate for the cross section chosen.

Figure 48 shows the observed subsidence and fault scarps and compares them with the best solution obtained from the models. Clearly the fit is not very good, but is satisfactory for a qualitative interpretation. The gravitational potential energy change obtained from our models will probably be an underestimate since the major discrepancy between the model and the observed subsidence is near the Red Canyon fault. Besides body forces reduced to 10% as a static load, the prestress applied to both models is pure horizontal tension at a level of approximately 400 bars. This makes the maximum shear associated with the tectonic stress have a 30° angle from the horizontal (i.e., dipping at 50° just like the fault surface.

Figures 49 and 50 show contour plots of the shear stress drop parallel to the fault, the maximum final shear stress and the strain energy density change. Figure 49 was obtained for a fault offset of 10 m along the entire fault width, offset which "grows" rapidly at both ends of the fault (over 1 km at the top and 500 m at the bottom). The first part of Figure 49 gives a false impression of large stress drop at depth; actually the fault overshot by a large amount at both ends of the fault, giving stresses larger than the prestress but with the opposite sign. Only the middle portion of the fault relaxed the prestress without overshooting.

This is clearly seen in the second part of the figure where the final stress is shown to be reduced in the middle (from the bend in the contour lines) while both ends of the fault exhibit a stress increase of the order of 400 bars. The plot of strain energy density change shows that strain energy was actually stored at both ends (up to a maximum of 1.67×10^{21} ergs/km^3). This is, however, limited to the very tip of the fault so that net balance shows a drop of 14.5×10^{21} ergs/km of

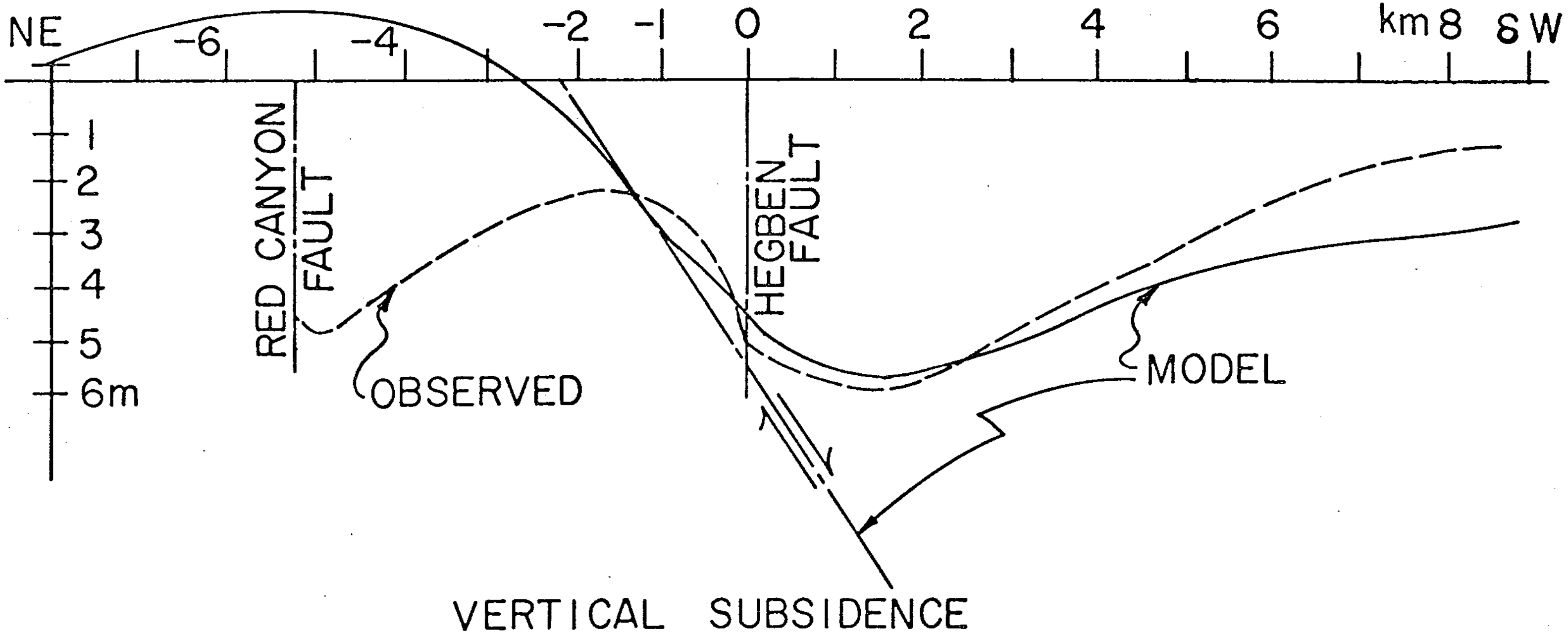

Figure 48. Comparison of observed and calculated vertical movement for the Montana earthquake. Cross section normal to the main fault at the middle.

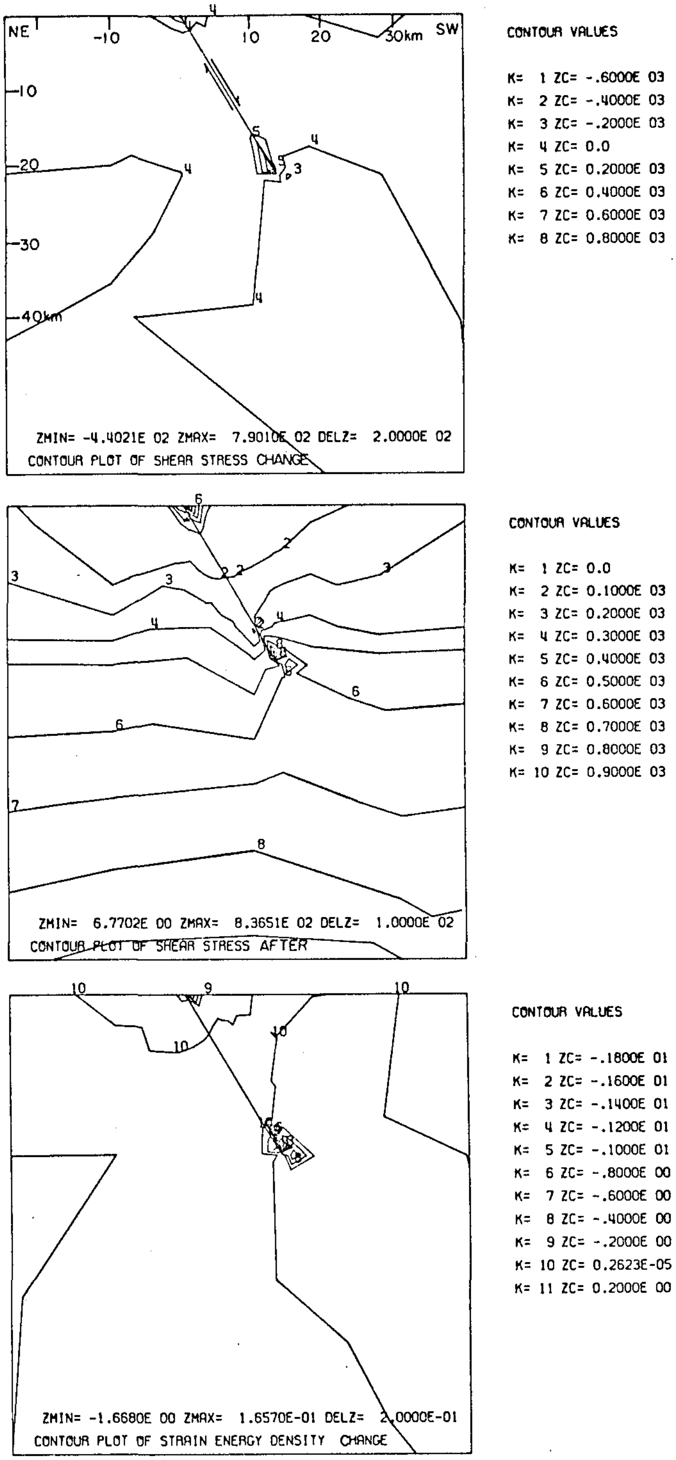

Figure 49. Shear stress change parallel to the fault, final shear stress and strain energy change for model 1. Units are bars and 10^{21} ergs/km^3.

fault length. This is clearly unacceptable even if the fault was driven to overshoot by the drop in gravitational potential energy.

Figure 50 is then the result for a model wherein the relative displacement dies out more smoothly at the hypocenter (from 10 m to 0 over 6.5 km of fault width). The result is a slightly increased stress drop over the middle of the fault and a stress increase limited to the free surface and below the hypocenter. The strain energy density increase is reduced by almost a factor of 10 at the hypocenter and the net energy balance exhibits a drop in strain energy of 24×10^{21} ergs/km of fault length.

The same models were run with no prestress which gives direct measurements of how much work would have to be done to create these faults. We found 35×10^{21} ergs/km of fault length for the first model and only 22×10^{21} ergs/km of fault length for the second. These values correspond to the origins of the lines of energy versus prestress shown in Figure 51. The lower set of lines correspond to model 1 and the upper set to model 2. In each case, the lowest line is the energy released by the fault relative offset, the upper line is the strain energy change. The difference between the two is the change in gravitational potential energy which, for both models, is positive and equal to about 8×10^{21} ergs per km of fault length. The stress drop averaged over the fault width and including overshoots for the sake of comparison with Brune and Allen's estimates are found to be, respectively, 400 and 300 bars. We can compare the possible energy released to E_{GR} (here for a hypothetical fault with properties of our cross section and length of 20 km). Assuming that the total energy released is greater than E_{GR}

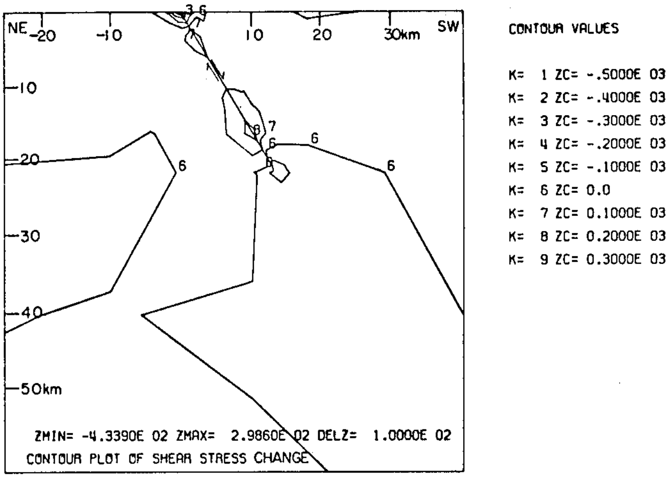

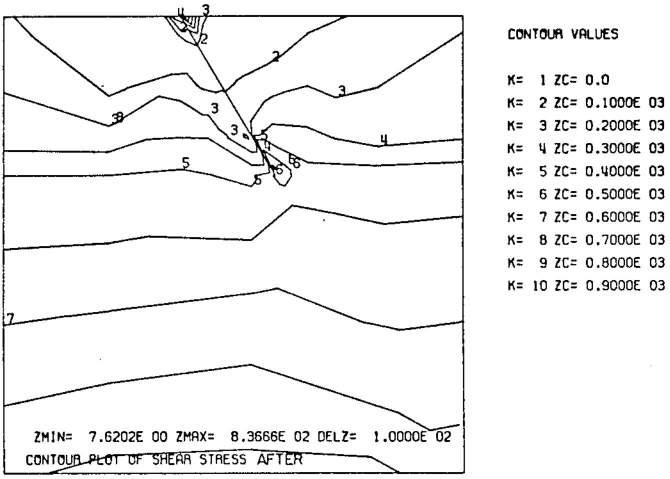

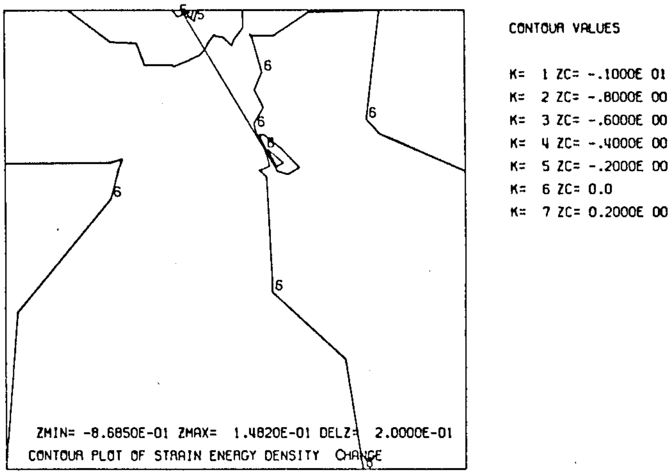

Figure 50. Model 2 with small gradient of slip in the hypocentral region.

by a factor of five, we see that the earthquakes described by our models could occur in an average prestress environment of less than 200 and 150 bars, respectively, even though work has to be done on the fault (or the stress drop is greater than the prestress).

From this oversimplified nonunique model of the Hebgen Lake, Montana, earthquake, we can conclude at least qualitatively the following:

(1) The average stress drop of 365 bars quoted for this event may very well be an apparent stress drop in the sense that a significant portion of it may represent fault overshoot.

(2) The local drop of gravitational potential energy may have been the driving force since it can be seen as an equivalent prestress (negative prestress).

(3) The resulting energy radiated contains the change in gravitational potential energy because it is a significant portion of the final δW.

A simple conceptual model like this one could be made for the Fairview peak, Nevada, earthquake of 1954 since it resulted in a net subsidence and in an apparent average stress drop of 180 bars (Savage and Hastie, 1966; Brune and Allen, 1971). This implies that normal faulting can occur in a relatively low prestress level (as opposed to thrust faults) while resulting in a large stress drop. The major difference between the tectonic processes involved in thrust and normal faulting could be simply the sign of the local change in gravitational potential energy since in the first case it absorbs energy released by the fault motion and in the second it provides a large portion of the radiated energy.

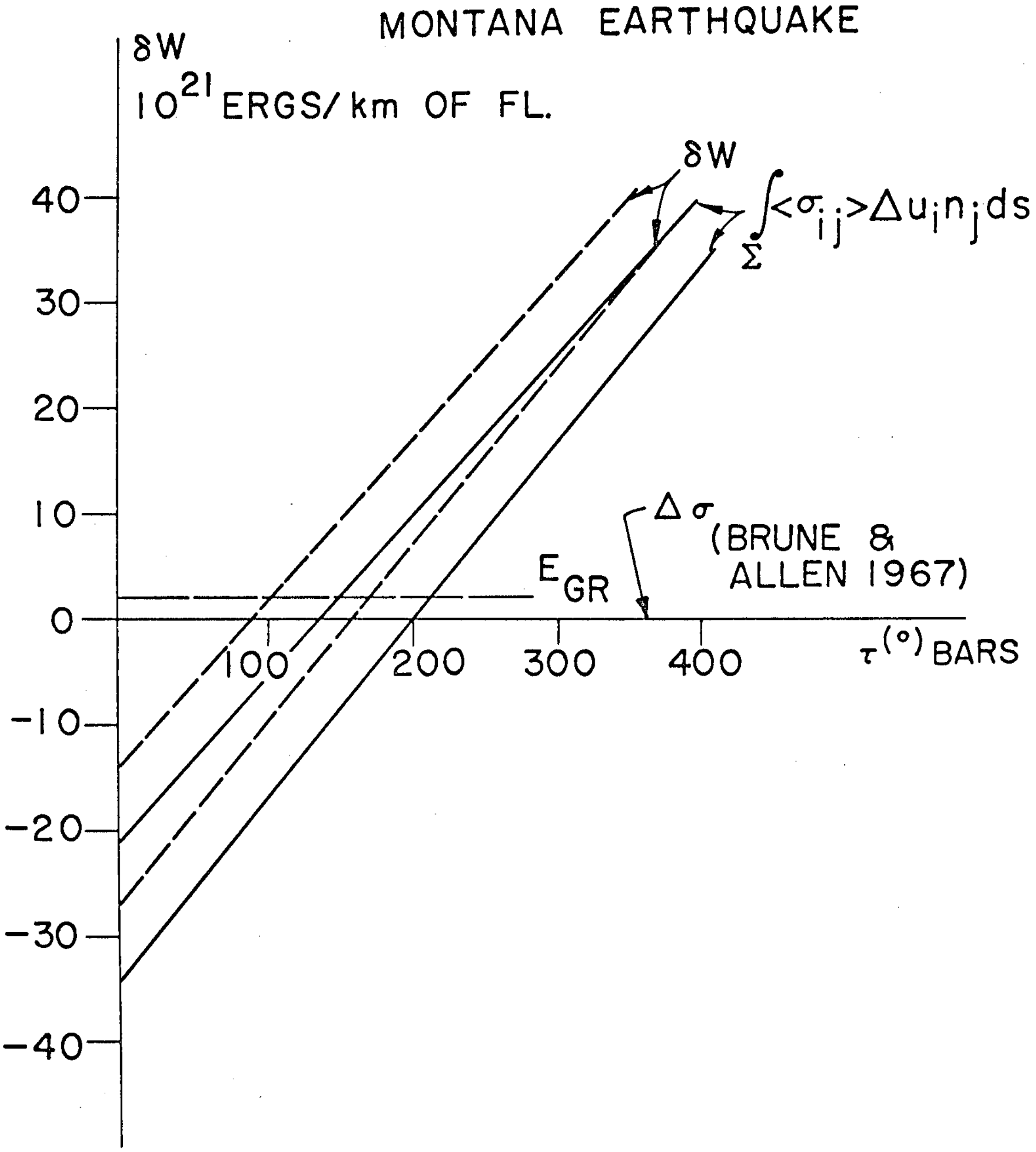

Figure 51. Idealized energy balance for the Montana earthquake. The upper two lines correspond to model 2.

V. TECTONIC EFFECTS OF FLUID-ROCK INTERACTION

Introduction

In the past decade, geophysicists have been increasingly aware of the fact that man, through his activities, can modify the prestress that is generated in the earth's crust by tectonic forces and that several mechanisms could be important.

Prompted by progress in civil engineering design, we have been constructing bigger dams and their subsequent filling with water has had the double effect of an additional static load and of weakening of some layers through the raising of water tables. This has generated some well recorded earthquakes in areas where natural seismic activity was nonexistent or of very low frequency (Kremasta, Greece, Kariba Dam, Rhodesia, Monteynard Dam, France and Koyna Dam, India).

Underground nuclear explosions have been shown to increase the seismic activity near the Nevada test site and the Aleutian test site, although there is some statistical evidence that they do not trigger far field events (Healy et al., 1968). This chapter will be concerned with the tectonic processes associated with removal of fluids from a stressed region.

The oil industry has been using a technique known as hydrofracture for more than three decades. Used basically as a hydraulic process for increasing reservoir productivity (Clark, 1949), it involves injection of brine at bottom-hole pressures equal or superior to 75% of the overburden. This was known to induce and extend fractures in the vicinity of the well (Harrison et al., 1954). The theory involved the use of the thick pipe formula

$$p_i = 2\sigma_H + S_t$$

where σ_H is the horizontal tectonic stress, S_t is the tensile strength of the rock and p_i is the hydrostatic pressure applied in the borehole.

These techniques were usually restricted in their geographical usage to non-tectonically stressed regions, and no earthquakes were reported with a direct connection with hydrofracture operations although a denser network would have probably detected small events. More recently, however, underground injection in tectonically active regions was used by the oil industry for the purpose of secondary recovery (or repressurization of an oil field) and by various other agencies for the purpose of waste water disposal. In this case, by contrast with hydrofracture, the well head pressure is not of the order of magnitude of the overburden, but is sustained for long periods of time. The consequence, as can be seen from considerations of the simple equations of a well in a confined aquifer, is a build up of pressure head farther and farther away from the injection point. After some time, fluid pressure buildups will spread to areas which because of tectonic prestress may be in a state of incipient failure.

Such a conceptual model was proposed for the Denver, Colorado earthquakes of 1962 to 1964 by Healy et al. (1968) by comparing the time-space distribution of the swarm with the pumping records of the Rocky Mountain Arsenal well.

In a controlled experiment conducted by the U. S. Geological Survey at the Rangely (Colorado) oil field, it was found that water pressures exceeding the hydrostatic (water weight) trigger earthquakes on preexisting faults (Raleigh and Healy, at the Penrose Conference of September, 1971).

In California, the ground rupture that resulted in the catastrophic failure of the Baldwin Hills Reservoir was genetically related to high pressure pumping in the local oil field (Hamilton and Meehan, 1971).

The last example of earthquake-underground pumping relationship is found in the Wilmington oil field, where as a direct result of oil removal, the free surface subsided down to a maximum of 9 m. Several earthquakes were recorded in the area from December 14, 1947 to April 4, 1961.

The physics of injection and removal is the same and involves considerations of effective stress and consolidation (or swelling) phenomena. This is the subject of the next papagraph. Later on, we shall try to model the Long Beach oil field situation by using an axisymmetric finite element program which embodies the theory.

Theory of Effective Stress and Consolidation

Various theoretical models have been developed to describe the mechanical interactions between the solid and the fluid constituents of a saturated porous solid material such as soil or rock. Developed by soil engineers, the basic theory involves considerations of gradual settlement of saturated soils, i.e., consolidation or compaction.

The first simple mechanism to explain this phenomenon is due to Terzaghi who developed the effective stress law for saturated soils as

$$\sigma_n = \sigma - p \tag{5.1}$$

with σ_n the effective normal stress on a plane, σ the total normal stress on the plane, and p the excess pore water pressure or neutral stress (= total pore pressure minus hydrostatic pore pressure (ρwh)). This is then used by most authors inside the concept of a Coulomb's failure criterion. Then

$$\tau_{\text{failure}} = \tau^{(0)} + \sigma_n \operatorname{tg}\varphi$$

This adequately explains the Rangely oil field microearthquakes (Raleigh, 1971) and was used in a slightly modified form by Hubbert and Rubey (1959) to explain overthrust faulting. However, Terzaghi's approach is essentially one-dimensional and although it is a good approximation of soils, it is not necessarily adequate for rocks subjected to high tectonic stresses.

Various authors apply correction factors to the effective stress concept, but these correction factors are empirical in nature and require laboratory determinations of empirical factors. However, all of these empirical formulations are not three-dimensional and transient effects of flow are not considered explicitly.

The next major extension of the theory of consolidation was made by Biot (1969) in which the process was analyzed in three dimensions. In his formulation, a set of constants is used to account for the interaction between the rock matrix and the fluid and formal solutions of his equations have been obtained only in a limited number of cases for which explicit laboratory tests exist (together with their connection to Biot's constants). All of this is readily available in the soil engineering literature (Jumikis, 1962; Scott, 1963; Lee, 1968) and we will limit ourselves here to writing Biot's general formulation with special reference to the basic assumptions involved and the physical meaning of the constants.

All the formulation is linear and as such it applies to saturated soils and rocks where:

(1) The strains are small compared to unity.

(2) The stresses and strains are linearly related.

(3) The velocities are slowly varying so that inertial forces can be neglected.

(4) The flow inside the rock matrix is laminar (small Reynolds number).

(5) The drag forces between the pore fluid and the rock matrix are linearly related to the relative velocity between the fluid and the rock grain (i.e., the Darcy's law describes the flow macroscopically).

In a summary of his work (1962), Biot reviews his derivation of the mechanics of deformation of a saturated porous solid. Essentially his derivation is based on considerations of the strain energy of the system which he assumes must be a function of the six strain components relevant to the rock matrix and a volumetric strain tensor relevant to the fluid (the fluid content). This last one is defined as (in vector notation)

$$\xi = \nabla . \left(n(\underset{\sim}{\overline{U}} - \underset{\sim}{\overline{u}}) \right) \tag{5.3}$$

where n is the porosity coefficient, $\underset{\sim}{\overline{U}}$ is the absolute displacement of the fluid, $\underset{\sim}{\overline{u}}$ is the displacement of rock matrix. Thus

$$W = W(\epsilon_x, \epsilon_y, \epsilon_z, \gamma_x, \gamma_y, \gamma_z, \xi) \tag{5.4}$$

Then, quite generally, he writes

$$\tau_{ij} = \frac{\partial W}{\partial \epsilon_{ij}}$$

and (5.5)

$$p = \frac{\partial W}{\partial \xi}$$

where p is the pressure in the fluid of Eq. (5.1). For an isotropic medium (or layer of rock) the strain energy is quadratic in strain. This allows Biot to derive an empirical stress strain relationship for the medium such that

$$\tau_{ij} = 2\mu\epsilon_{ij} + \lambda\delta_{ij}\epsilon_{kk} \quad - \alpha\,\delta_{ij}p$$

and (5.6)

$$\xi = \alpha\,\delta_{ij}\epsilon_{ij} + \frac{1}{M}p$$

where α and M are constants derived by Biot. They are "elastic" coefficients which have to be determined by performing specific experiments. For example, Biot defines α implicitly, through an "unjacketed" compressibility test giving a coefficient

$$\delta = (1 - \alpha)\varkappa \qquad (5.7)$$

where $\varkappa$ is the compressibility of the rock matrix defined in elasticity as the inverse of the bulk modulus. This means that physically α relates the bulk modulus of the rock matrix to the bulk modulus of the rock grains. Although not explicitly stated in Biot's work, this involves a relationship between the pore size and their evolution with time.

From considerations of Eqs. (5.6) and (5.3), we can see that if $\alpha = 1$ (which is true for some water saturated clay (Biot, 1941)), we see that the stress strain relationship becomes completely connected to the fluid pressure ($M = \infty$ for incompressible fluid). Physically this means that a triaxial compression test (initial $p = 0$) would result in a volume of seeping water equal to the volume that the specimen is compressed ($\xi = -(\epsilon_{xx} + \epsilon_{yy} + \epsilon_{zz})$). Or, applied to an oil field, the total volume of subsidence would be equal to the amount of oil removed. The other extreme of α should be zero and not the porosity coefficient as claimed by Biot and Willis (1957). As can be seen from Eq. (5.6), $\alpha = 0$ and $1/M = 0$ (incompressible fluid) leads to a complete decoupling of the fluid flow and the rock matrix (i.e., the rock-fluid system behaves like the rock alone (see Eq. (5.7)).

Equilibrium conditions in the rock matrix can be expressed by combining the momentum equations for fluid and rock. Thus using Biot's empirical stress strain relationship and ignoring inertial forces (small accelerations are required for Darcy's law to apply), we get

$$2 \frac{\partial}{\partial x_j} (\mu \epsilon_{ij}) + \frac{\partial}{\partial x_j} \left[\lambda \delta_{ij} \epsilon_{kk} \right] + \rho f_i = \frac{\partial}{\partial x_j} \left[\alpha \delta_{ij} p \right] \tag{5.8}$$

or for a homogeneous material, in vector notation

$$\mu \nabla^2 \vec{u} + \left[K + 1/3\, \mu \right] \nabla (\nabla \cdot \vec{u}) + \rho \vec{f} = \alpha \nabla p \tag{5.9}$$

The left-hand side of (5.9) is the familiar equilibrium equation of elasticity and the contribution of the consolidation is entirely on the right-hand side.

The next equation needed to solve the problem is the compatibility or continuity of the two phases (rock and fluid). For that, we use the generalized Darcy's law (which itself is a special case of the

Navier-Stokes equation). It is written here as

$$\frac{\partial}{\partial t}(\bar{U}_i - \bar{u}_i) = \frac{k}{\nu}\frac{\partial p}{\partial x_i} + \frac{k}{\nu}\rho f_i \tag{5.10}$$

where k is the permeability coefficient, ν is the kinematic viscosity of the fluid. From Eq. (5.3), we get by differentiating (5.10) by x_i

$$\frac{\partial}{\partial t}(\xi) = \frac{k}{\nu}\left(\frac{\partial p}{\partial x_i} + \rho f_i\right)_{,i} \tag{5.11}$$

From the definition of ξ (Eq. 5.6) this is for an isotropic medium and assuming that Biot's constants do not depend on time

$$\frac{1}{M}\frac{\partial p}{\partial t} - \alpha\frac{\partial}{\partial t}(\delta_{ij}\epsilon_{ij}) = \frac{k}{\nu}\frac{\partial^2 p}{\partial x_i^2} + \frac{k}{\nu}\frac{\partial}{\partial x_i}(\rho f_i) \tag{5.12}$$

or in vector notation

$$\frac{1}{M}\frac{\partial p}{\partial t} - \frac{k}{\nu}\nabla^2 p = \frac{k}{\nu}\nabla\cdot(\rho \underset{\sim}{f}) + \alpha\frac{\partial}{\partial t}(\epsilon_{xx} + \epsilon_{yy} + \epsilon_{zz}) \tag{5.13}$$

Eqs. (5.9) and (5.13) completely define the problem at hand, with the following mixed boundary conditions

$u_i(\underset{\sim}{x}, t) = C$ on S_u

$\tau_{ij}(\underset{\sim}{x}, t)n_j = T_i$ on S_τ

$p(\underset{\sim}{x}, t)$ = constant on the permeable boundaries

$\frac{\partial}{\partial t}\left[(\bar{U}_i - \bar{u}_i)n_i\right] = Q_o$ on the boundaries where a flow is assigned.

Ghaboussi and Wilson (1971) developed a finite element formulation for solving this set of equations and boundary conditions for two-dimensional and axisymmetric problems. Their technique is a direct application of what is known as Gurtin's variational method which results in a set of integral equations quite similar to those presented in Chapter I of this thesis (Gurtin, 1964). Isoparametric rectangular elements are used where the displacements are a quadratic function of the coordinates (Zienkiewics, 1972). This code uses a simple explicit finite difference scheme for the time stepping. During each interval of t and t + Δt, a linear variation of pore pressure and matrix displacement is assumed.

We used their program for modeling the Wilmington oil field with only small corrections designed to improve the initial response to a step function input such as Q_o.

The Wilmington Oil Field Subsidence

Observations

The Wilmington oil field, located at the southwest end of Los Angeles, is interesting for several reasons. One is that its surface has exhibited the largest amount of subsidence on record, directly attributable to man's activities (Gilluly and Grant, 1949). Because of its location, the surface movement has been recorded continuously since the beginning of the oil production (1928). Further, because of the shearing of several producing wells concomitant with minor earthquakes, we have a record of the hypocentral location of events triggered by this activity with nearly absolute precision, together with a good determination of the amount of slip. Some of these earthquakes with magnitudes ranging from 2.4 to 3.3 have been recently analyzed by Kovach, Archambeau and Harkrider (1972) and provide us with estimates of the average stress drop associated with them. Furthermore, for the central part of the subsidence bowl, the structure can be considered almost axisymmetric which permits us to model it by using the finite element program of Ghaboussi and Wilson. This stems from the shape of the reservoir, which for the region involved, looks like a dome with a very small curvature of its anticlinal axis. This is seen quite clearly in the subsidence plots of Allen (1971).

Models

Figure 52 shows the finite element grid used in this study. For simplicity and lack of better information, the layering was represented as flat. The 12 layers which are represented as perfectly parallel are essentially composed of a thick, impervious nonproductive top layer which confines the seven major oil producing zones. Layers 3 and 4 were added because all of the earthquakes occurred at those depths (Kovach et al., 1972), and layer 4 is bounded by two thin layers of clay clearly visible on the spontaneous potential log (in Manyuga, 1970). An artificial boundary was added between layers 6 and 7 to represent the bottom of the Pliocene. The elastic properties and hydro-geological characteristics of each layer are shown in Table 5. The geological information is from Manyuga (1970), and the elastic parameters are from Kovach, Archambeau and Harkrider (1972). The bottom of the oil-producing strata is Franciscan schist and is clearly impervious from the SP-R logs.

In order to obtain the coefficient of dynamic viscosity used in the program, we used an average value for oil at room temperature or 100 centipoise (10^{-3} kgrmass/cm·sec). Since we have to model the oil field for a period of 32 years, we used a first time step of only

28 days, reaching 32 years by 42 time steps increasing in length. This insured the stability of the finite difference scheme. During the period covered by the model (1930-1962), the rate of oil withdrawal remained practically constant at 100, 000 barrels per day or 18.4 m^3/sec.

As a first model, designed to determine the approximate value of Biot's constant α for the field as a unit, we imposed a constant pumping rate throughout the oil producing units with a total yield at the "well" head of 18.4 m^3/sec. Our well is at the center of the axisymmetric model, the left-hand side of the grid. Since the oil field is larger than our grid in the northwest-southeast direction, we imposed a constant pressure boundary condition on the outer boundary of the model. This permits flow to occur from the parts of the oil field outside the grid. For the purpose of solving the equilibrium equation, a no displacement boundary condition is imposed. The bottom of the grid is made impervious, displacement free in the vertical direction and traction free in the horizontal. The free surface is stress free and layer 1 is quasi impervious. The results showed that for a coefficient $\alpha = 1$ the amount of subsidence matched exactly the total volume of fluid removed.

In order to get the calculated subsidence to fit that observed, a coefficient $\alpha = 0.023$ was required. This is at least an order of magnitude less than the average porosity of the formations, which according to Biot (1962) is the minimum value for α.

From the discussion of the previous paragraphs, this can be tentatively interpreted as an indication that under overburden pressures such as can be expected at depths of the order of a kilometer, the soft

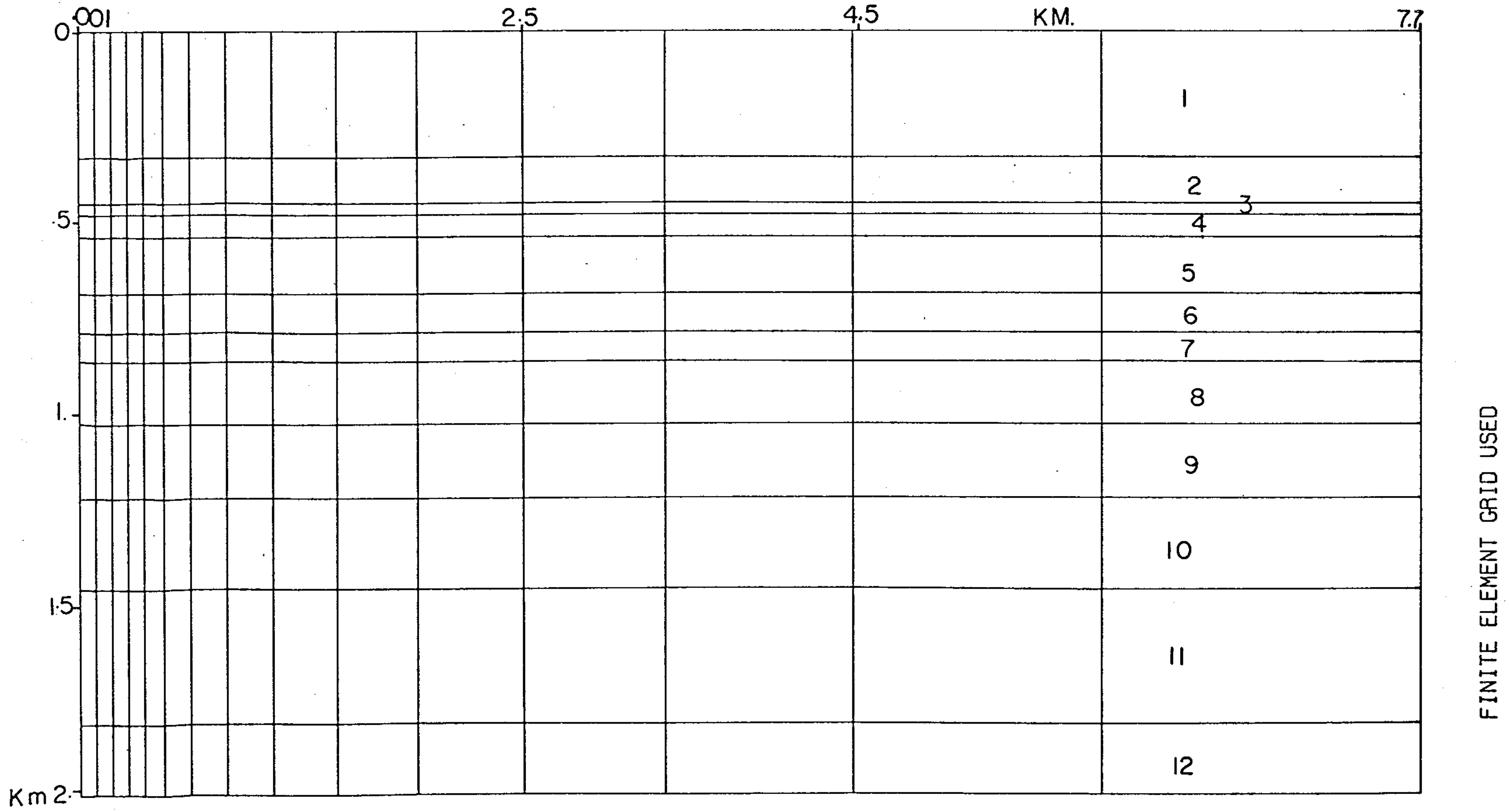

Figure 52. Axisymmetric grid used to model the Wilmington oil field. The Earthquakes occurred in layers 3 and 4.

TABLE 5

	Layer	Geologic Unit	Poisson's Ratio	Young's Modulus kbars	Coeff. of Permeability $m^2/sec \cdot kbar$	Porosity	Permeability in Milidarcy
	1	Recent	.299	60.5	.0001	?	?
	2	Upper Pliocene (Pico)	.299	60.5	.003	35-40%	≃ 3000
	3		.299	60.5	.003	35-40%	≃ 3000
	4		.299	60.5	.0001	?	?
	5	Lower Pliocene (Upper Repetto)	.299	60.5	.003	35-40%	≃ 3000
	6	Lower Pliocene (Middle and Lower Repetto)	.299	60.5	.003	35-40%	≃ 3000
MIOCENE	7	Delmontian	.299	60.5	.002	35-40%	≃ 1750
	8		.299	60.5	.00075	30-40%	≃ 750
	9		.299	136.	.0005	25-30%	≃ 550
	10	Puente	.299	136.	.0001	20-25%	≃ 110
	11	Momnian	.299	136.	.00005	20-25%	≃ 55
	12	Luisian	.299	136.	.00001	20-25%	≃ 105
	Franciscan						

sediments of the Los Angeles basin do not behave like soils, but more like "rocks" whose overall bulk modulus exhibits only small variations as a function of fluid pressure.

Model 2 has one refinement compared to the first. It was felt that since layers 2 to 7 (excepting 4) are reported as being the major oil producing zones and since they have permeabilities nearly an order of magnitude larger than the lower five layers, we should attempt to approximate the real situation by making the flow rates proportional to K (scaled to give a "well" head production of 18.4 m^3/sec).

This is shown in Figure 53. This contour plot of horizontal flow is a clear indication of the "pumping" pattern. Since it represents flow rates inside a segment of the axisymmetric model of thickness equal to the radius, the maximum values at the well (1 m radius) are found in layers 1, 3 and 3 to 5 ($\simeq$7 liters per meter of well per sec).

Model 3 differs from model 2 in that instead of a constant coefficient α of 0.023, we scaled α to the value of permeability of each layer (the best result was obtained for $\alpha = 20$ K, K from Table 5). This stems from the assumption that the greater the porosity (permeability), the more the medium will consolidate like a soil.

Figure 54 shows a comparison between the maximum subsidence observed (in 1962) and the calculated values for the three models. From the surface subsidence alone, it seems that the results are insensitive to the model variations we imposed. In all three cases, the fit is good and could possibly be improved by giving a slight curvature to the layers and by varying the properties of the units laterally.

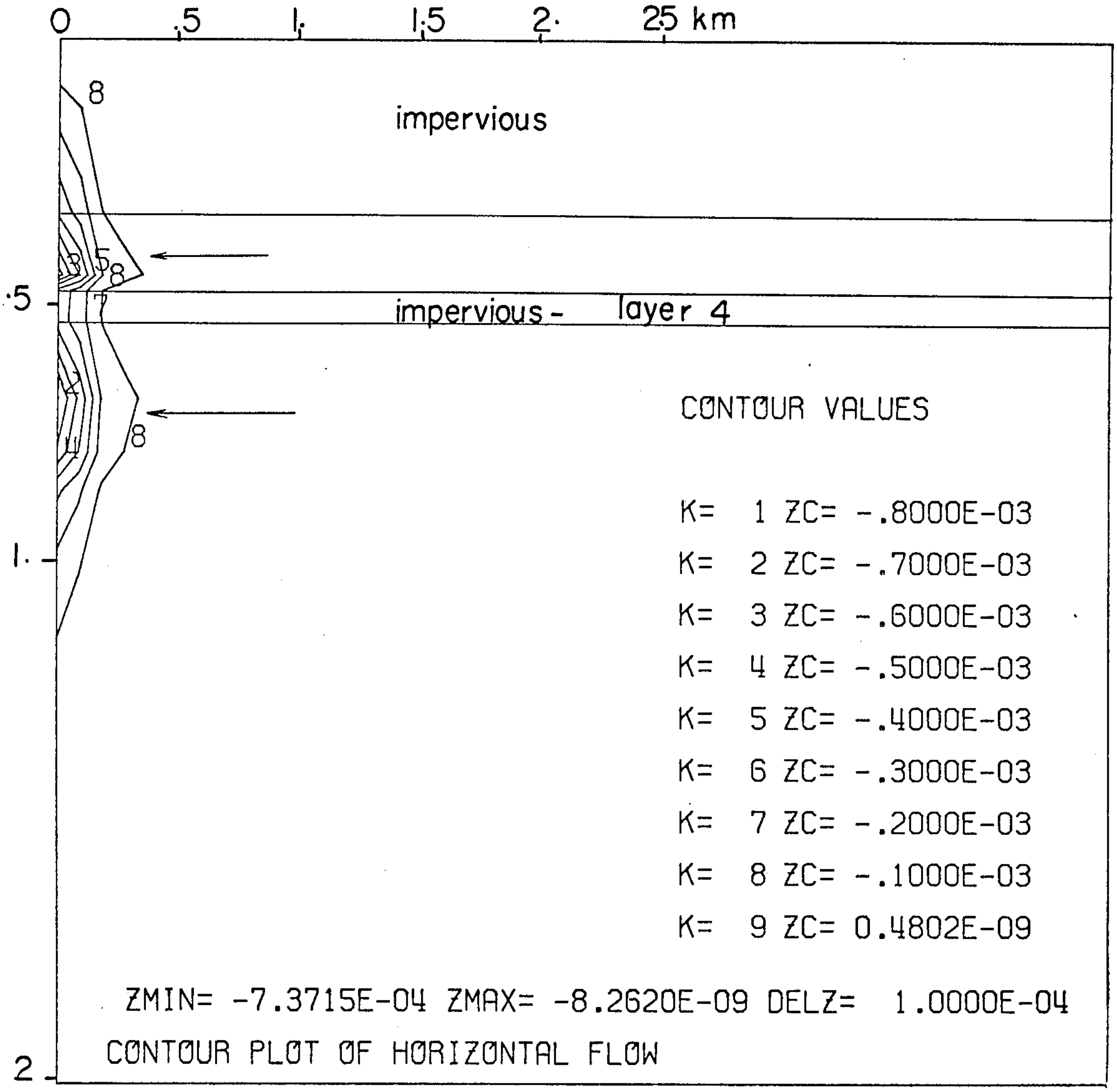

```
CONTOUR VALUES

K=  1 ZC= -.8000E-03
K=  2 ZC= -.7000E-03
K=  3 ZC= -.6000E-03
K=  4 ZC= -.5000E-03
K=  5 ZC= -.4000E-03
K=  6 ZC= -.3000E-03
K=  7 ZC= -.2000E-03
K=  8 ZC= -.1000E-03
K=  9 ZC= 0.4802E-09

ZMIN= -7.3715E-04 ZMAX= -8.2620E-09 DELZ=  1.0000E-04
CONTOUR PLOT OF HORIZONTAL FLOW
```

Figure 53. Flow rates in cubic meter per second in a sector of the axisymmetric model. The rates are proportional to the permeability coefficients of the layers.

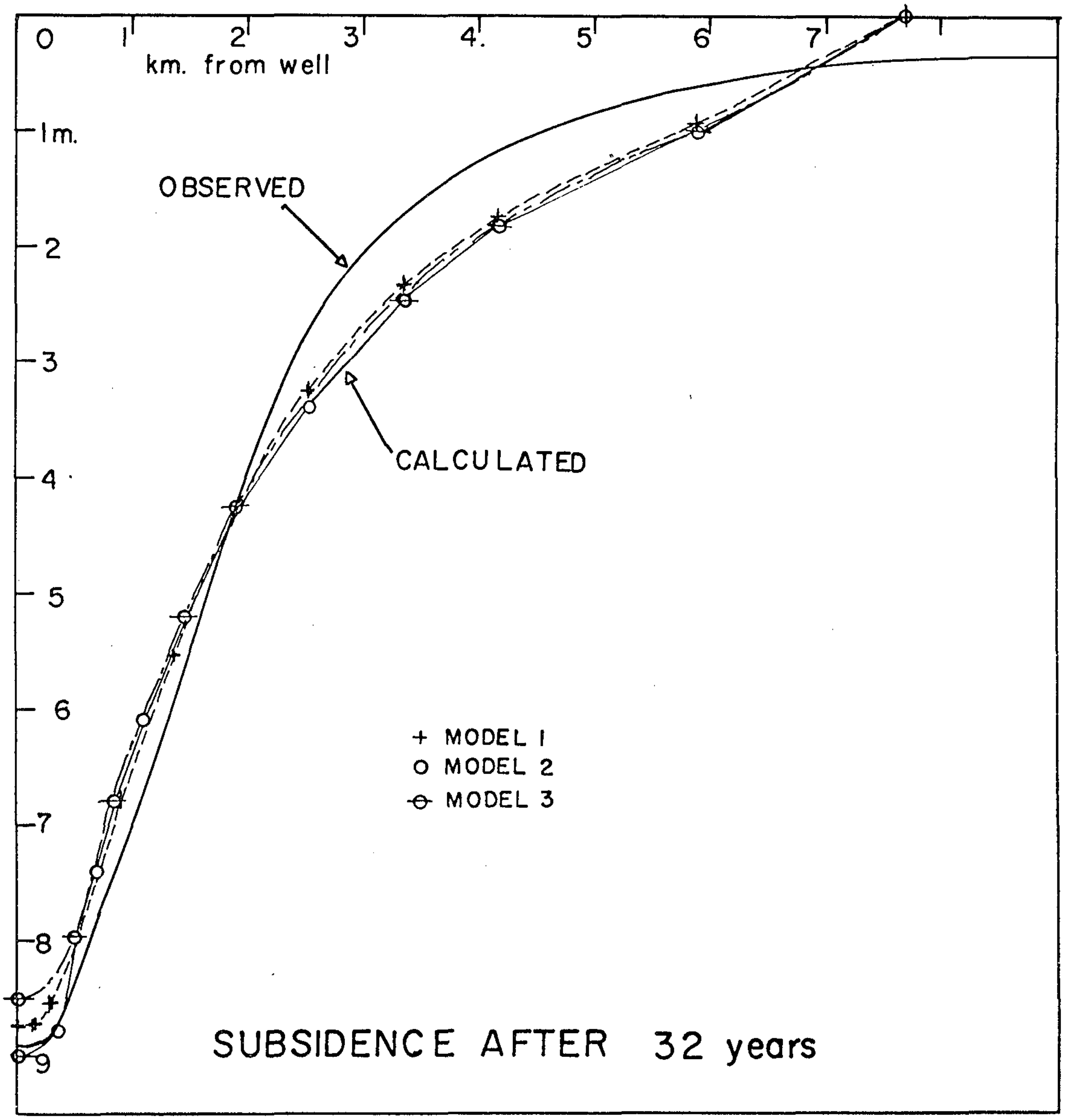

Figure 54. Comparison of observations with calculated maximum subsidence of the free surface.

Figure 55 shows the same comparison for the horizontal movement. Here the fit is not very good except that all three models have a neutral axis (separating extension from compression) which matches the observed. However, Allen (1971) points out that the control on the observations is not good and the data could be considerably in error. In fact, although his contour lines indicate a general convergence towards the axis of the field, this axis is shown to have a horizontal movement of 1.2 m. Since this should be the zero displacement point (relative, horizontal), 1.2 m may be the size of the error for these data. Here again, the difference between the models is not significant.

This is not true at depth as is clearly shown in Figure 56. The upper plot corresponds to model 2, the lower one to model 3. For model 2, where α was constant throughout the grid, the subsidence is regularly distributed and appears to be insensitive to the variations in flow rates with depth. For model 3, the upper layer and layer 4 ($\alpha = 2 \times 10^{-4}$) behave like pure elastic beams (Eq. 5-7) and the vertical displacement is larger at the bottom than at the top (reverse from model 2). By contrast, the layers with larger α (0.06) and large flow rates, show a significant amount of consolidation. The bottom layers of the "oil field" have coefficients α and flow rates decreasing with depth and show a small amount of reversed consolidation (swelling). The contrast between models 2 and 3 is amplified in Figure 57. This is to be expected from Eq. (5.6) where α and the pore pressure (function of the flow rate) are shown to act on the stresses in the same direction. Model 2 results in a maximum shear stress of approximately 114 bars in the layers with high flow rates. This shear stress is maximum 500 m from the axis.

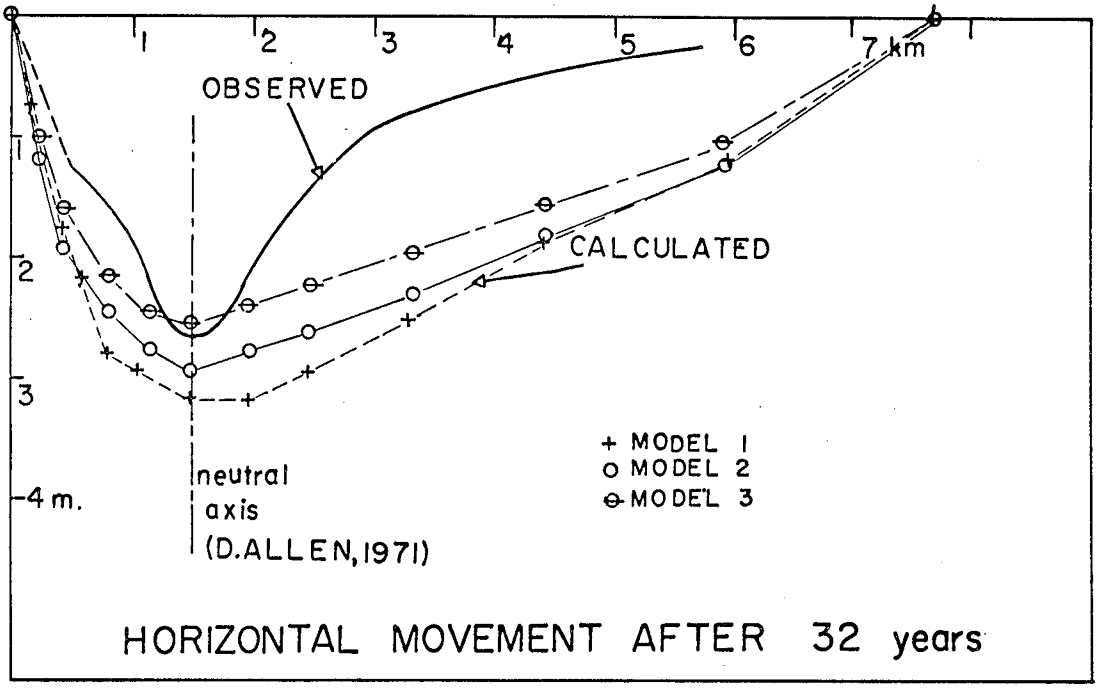

Figure 55. Comparison of observed and calculated maximum horizontal movements of the free surface.

For model 3, the maximum shear stress is 489 bars in the same areas. Furthermore, it shows rapid changes from layer to layer. In fact, inside layer 4 the maximum shear stress is only 100 bars, but it is averaged over by the plotting program. Since a significant amount of oil was removed from layer 4 (Allen, 1968), we think that the contour plot is a better representation.

Kovach et al. (1972) report that all seven earthquakes they studied had a hypocentral depth between 472 and 518 m and an epicenter approximately 1 km away from the axis of subsidence. This would place these events in the region of calculated maximum shear stress in both models. On the basis of horizontal offsets of 20 cm, measured on redrilled oil wells, they estimate an average stress drop of approximately 20 bars. However, on the basis of his source theory calculations, Archambeau (personal communication, 1972) estimates the prestress to be at least 50 bars.

Since all these values are averaged over fault areas of the order of 4 km^2 and in view of the results of the preceding chapters of this thesis, we feel confident that our models, however crude, are a good estimate of the stresses generated by the Wilmington consolidation.

As a first order estimate, Kovach et al. (1972) give as a failure criterion the modified Coulomb-Mohr criterion (Eq. 5.2). They estimate an effective compressive stress (vertical) at 520 m depth of 65 bars. This includes a lithostatic pressure of 114 bars minus a fluid pressure of 49 bars ($\rho_1 gz$ in both cases). Thus, following the failure criterion, they estimate an upper bound for the shear stress at failure of 65 bars. From Eq. (5.6) we get a direct calculation of all three components of stress in the rock matrix (after 32 years of flow, for a point 1 km away from the axis and at 520 m depth). If we use a generalization of the von Mises failure criterion (Mogi, 1972), i.e.

$$\tau_{oct} = f(\sigma_{oct}) \cong C_1 \sigma_{oct}$$

where τ_{oct} is the maximum shear stress in three dimensions, and σ_{oct} is the mean effective stress defined as

$$\sigma_{oct} = 1/3\left(\sigma_1 + \sigma_2 + \sigma_3\right) - p$$

$$\tau_{oct} = 1/3\left((\sigma_1 - \sigma_2)^2 + (\sigma_2 - \sigma_3)^2 + (\sigma_3 - \sigma_1)^2\right)^{1/2}$$

we get (in the region of the hypocenters) after 32 years (we assume that the stresses computed at that time are the yield stresses)

For model 1

$$\tau_{oct} = 43 \text{ bars}$$

$$\sigma_{oct} \cong 218 \text{ bars}$$

$$C_1 \cong .197$$

For model 2

$$\tau_{oct} = 75.5 \text{ bars}$$

$$\sigma_{oct} \cong 261.3 \text{ bars}$$

$$C_1 \cong .289$$

For model 3

$$\tau_{oct} = 265 \text{ bars}$$

$$\sigma_{oct} \cong 700 \text{ bars}$$

$$C_1 \cong .378$$

This increase of the ratio of octahedral stress to mean stress is found for other material tested in the laboratory (Mogi, 1972). Even though the tests he reports are for dolomite and involve higher confining pressures, this qualitative agreement indicates that the stress relationship that results from our models is self-consistent. As a result, the failure mechanism of the Wilmington oil field subsidence earthquakes is represented by relatively high prestress levels (when compared to their average stress drop). We can also point out that τ_{oct} is in the plane defined by the vertical and radial stresses and is inclined at approximately 40° to the horizontal. It corresponds to the maximum shear stress of Figure 57. The faulting associated with the subsidence earthquakes was horizontal in nature and from the redrilling data, the slippage places were shown to be thin shale layers of about 2 m thickness. Thus, the interpretation is that failure occurred in "weak" zones making an angle of approximately 40° with the maximum principal shear stress. Of course, it is possible that a model including elements with a 2 m scale would rotate locally the principal axis in such a way that the principal shear stress would become horizontal in the shale beds.

Rate of subsidence and stress build up

The subsidence earthquakes occurred between 1947 and 1961. It is then of some interest to compare our "best fit" solution and its evolution with time with the available data on past surface movements. Subsidence rates are shown in Kovach et al. (1972) for the years 1946 to the present. From these data it is possible to make an approximate integration with the 1962 subsidence as an initial value, while tying the results to the reported 3 m total subsidence measured in 1946. The

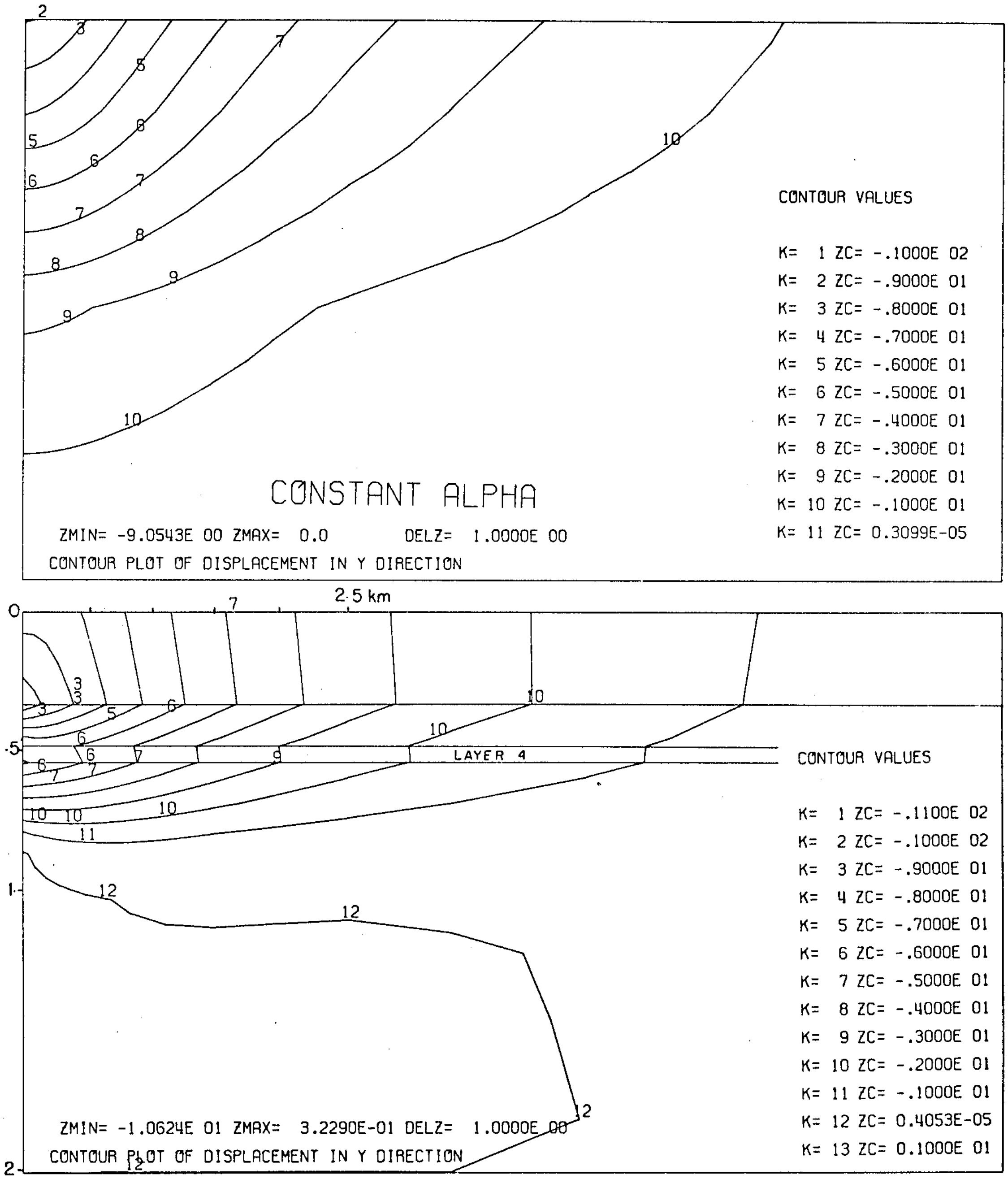

Figure 56. Vertical subsidence throughout the oil field after 32 years of pumping. Model 2 is on the top; model 3, at the bottom. Contour values are in meters. Note the strong influence of variations with depth of the interaction coefficient α.

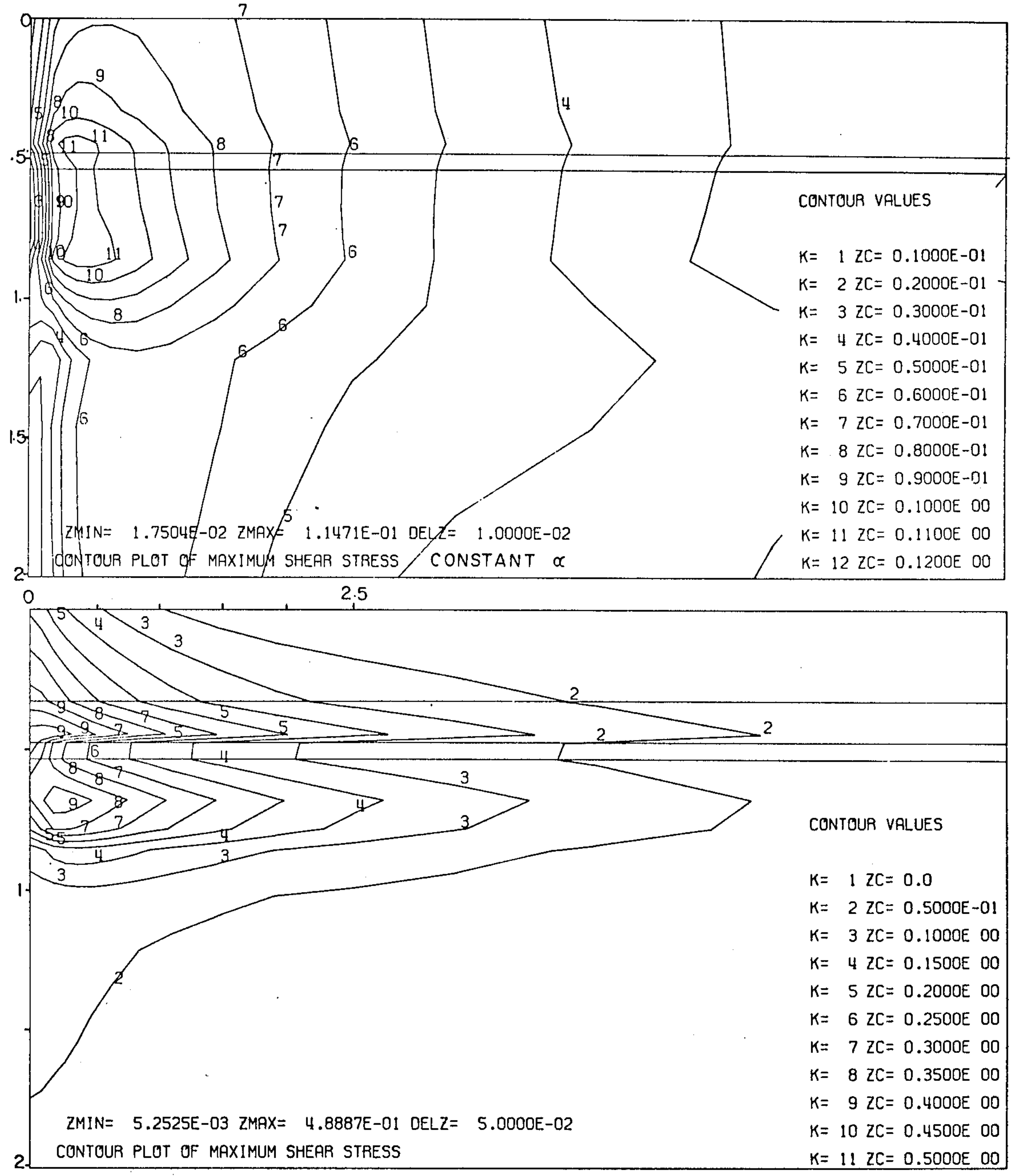

Figure 57. Maximum shear stress for model 2 and model 3. Contour values in kilobars. Note the influence of flow rates on model 2 and the combined influence of flow rates and variable α on model 3.

result is shown in Figure 58 and the comparison is not entirely satisfactory. One simple explanation could account for most of the discrepancy. In the real situation, because of technological and economical considerations, it is probable that the progress of drilling, thus of oil withdrawal, went downward from layer to layer on a time scale which could cover several decades (Gilluly and Grant (1948) report the development in 1947 of layers 10, 11 and 12 of our model). We can only speculate since at this time we do not have layer by layer oil production data, but if that was the situation, by adding several curves of subsidence with time, similar to the one we calculated (scaled to the layer thickness and time delayed), one could model more closely the real situation.

The same adding procedure could be followed for the shear stress, giving for 1947 values about 30% of those quoted above. The shear stress build up shown in Figure 58 indicates that, once pumping is turned on, the stress generated by consolidation climbs very steeply to reach values near its maximum in less than 5 years.

Conclusions

This chapter on consolidation phenomena has shown two important things.

(1) Rocks in geological environment do not behave like soils, in the sense that they exhibit a rather weak interaction with their fluid content. This was found to be true for a sedimentary unit considered as very soft and highly porous.

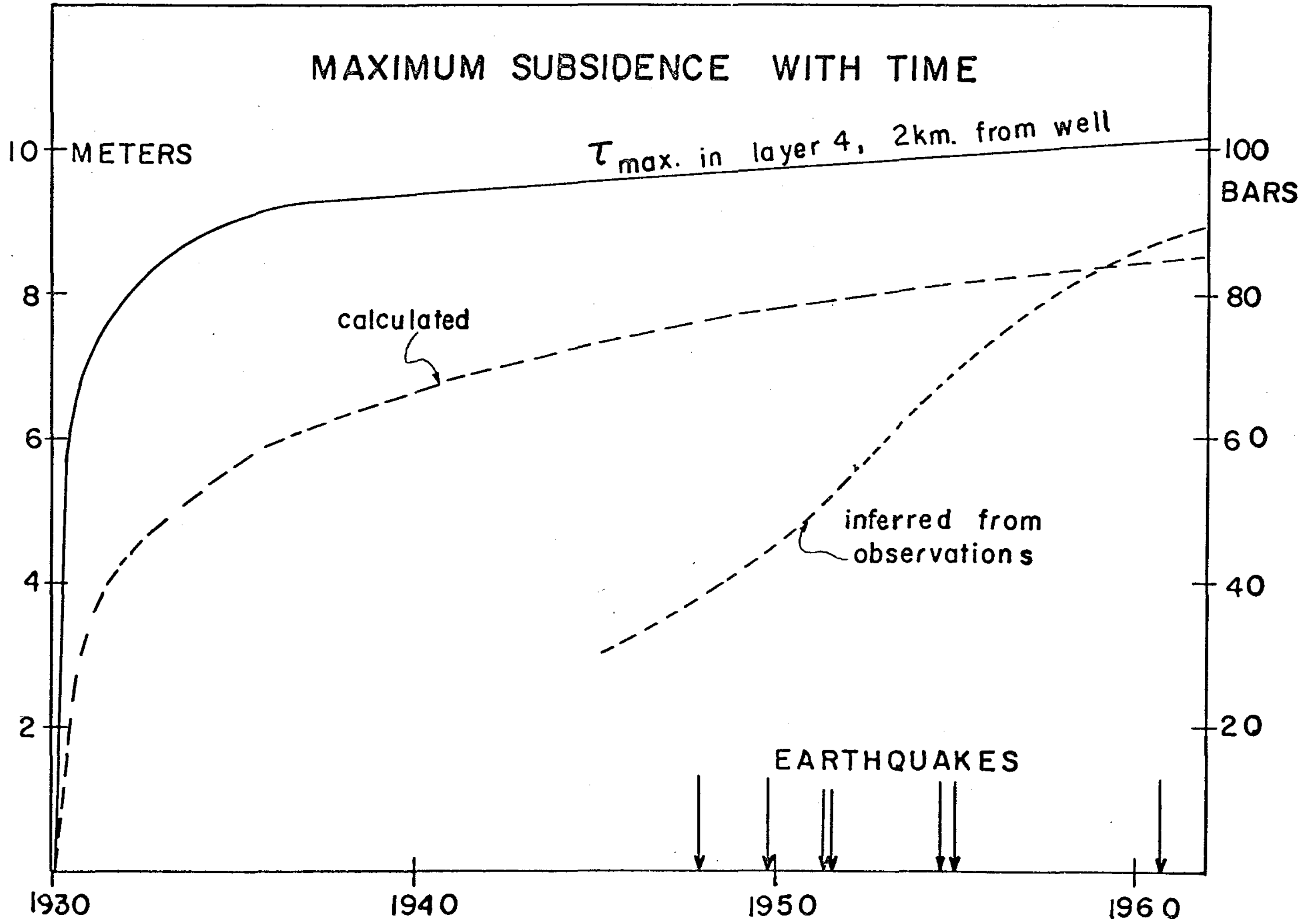

Figure 58. Subsidence at the well and maximum shear stress in the hypocentral region for model 2. The observed subsidence is obtained by backward integration on time of observed rates of subsidence. (Kovach et al., 1972).

(2) Relatively simple finite element modeling of fluid removal (or injection) can give a reasonable estimate of the stress field that results from this particular form of activity. This stress field could be compared to laboratory experiments as an attempt to predict failure. A large amount of work remains to be done before prediction becomes a possibility. Obviously, the models are only as good as the problem description. This depends on the information available regarding porosity, intrinsic permeability, fluid viscosity and their variation in space. Further, parameters appearing in the consolidation theory have no obvious physical expression which would permit us to assume reasonable values on purely intuitive grounds. We cannot use the empirical formulae developed by experiments in soil engineering because they are not valid for rock matrices found in oil reservoirs. However, note that we can, with the experience gained in this study, make some reasonable models to predict fluid-rock interaction in the Los Angeles basin.

Obvious future developments should attempt to express the interaction coefficients in terms of physical parameters measurable in situ (for instance, from well logs or seismic experiments).

GENERAL CONCLUSIONS

Numerical schemes that allow for irregular nonhomogeneous continua must be employed in order to examine the detailed near field deformations associated with an earthquake. The finite element method, which has proved to be quite versatile for computing stresses, strains and displacements in engineering applications, was extended to treat discontinuities in the displacement field. Judging from the high degree of accuracy with which vertical and sloping dislocations in a homogeneous half space are computed and the ease with which the numerical scheme can be applied to irregular geologic structures, the finite element method is ideally suited for near field earthquake calculations.

The analyses which were presented here are limited only by the accuracy of the problem description (and the computer time available). Clearly, in the case of the San Fernando earthquake and our two-dimensional treatment of it, the major difficulty resides in the problem description. The geodetic control, one of the most extensive ever reported, is still too sparse to allow unique solutions. However, it is interesting to note that Alewine (1972), using closed form analytical solutions based on dislocation theory to formulate a stochastic inversion scheme of the vertical displacement data, obtained a "best" solution which provides displacements along the fault which reach maximum values near the surface in a manner similar to our solutions. However, his fault offsets are smaller by 25% reflecting the influence of geology on our results. Thus, independent work employing a relatively unbiased inversion method yielded a result similar to ours.

This also indicates that for the upper 10 km of the fault, the strain balance of the earthquake is well determined by the available data, whether a one-fault or a multiple-fault model is used. For the lower portion of the fault, however, the problem becomes ill posed because of the uncertainty in the geology or prestress and variations in the fault dip. (Whitcomb's (1971) fault plane solution indicates a 52° dip of the failure plane at the focus while a recent hypocenter indicates an average dip of 33° for the entire fault plane.)

Despite the fact that we limited ourselves to two-dimensional modeling, thus ignoring the fault's end effects, this study brought out important new features.

The San Fernando failure process appears to have been quite complicated. After growing to an offset of from 2 to 5 m near the hypocentral region, the fault break reduces to a slip of no greater than 2 m at 10 km depth. Then, depending on the cross section considered, the fault offset grows exponentially up to approximately 8 m near the surface. In the last kilometer before break out, the offset reduces to the observed 2 m fault scarp offset probably as the result of plastic deformation in the near surface alluvium adjacent to the fault and/or multiple near surface fracturing.

The stress drops that result from our analysis, although certainly nonunique, point towards complex fault mechanism. Depending on the details of the hypocentral region and the "knee" of the fault, we get a peak stress drop of approximately 650 bars. Together with the values of the prestress field which is thought to give the best results, this indicates that the rock at 10 km depth exhibits strength properties of granite at 2 kbar confining pressure (Mogi, 1972).

The model treated here results in a large stress concentration at the knee of the fault which brings the final stress for that area within the range of material strength for 1 kbar confining pressure. Although this interpretation seems to be substantiated by the aftershock locations, it is clear from the alternative solutions we presented in Chapter II that this is not well resolved.

Also not well resolved because of the two-dimensional simplifications is the problem of joining the Tujunga with the Sylmar fault segment. Our solutions yield a large difference, up to a factor of two, in the fault displacements between the two sections AA' and BB'. Although their behavior at depth is similar and section BB' is 1.8 km wider, the difference between them is so large that it implies rapid variations in displacement through the region between them. It is possible that a more complete picture could be obtained in three dimensions. For instance, it is intuitively reasonable to believe that we could fit the observations with a main fault similar to AA', which upon approaching the free surface generates a large number of secondary faults. Then the only difference between the two fault segments would be in the number of secondary faults they generate, a function of the geology in the upper 2 km. Clearly, with the information available to us, this would be unresolvable and would not change the situation in the hypocentral region.

Strains computed in our models give only order of magnitude fits to the observed strains at the Isabella station (Jungels and Anderson, 1971). This is not surprising in view of the short fault length. However, our two-dimensional analysis shows clearly that in order to interpret strains and tilts at teleseismic distances models taking into account the geology and fault slip variations are necessary since these factors are just as important as fault end effects.

While all of the analysis that is presented in the first chapters is static, we note that the finite element method can also provide a dynamic simulation of an earthquake, with spontaneous rupture processes serving to generate the seismic disturbance in a prestressed environment. The numerical technique is not well suited for high frequency motion, nor dynamic behavior in the intermediate range beyond the near field. However, it could be used to model the Pacoima Dam record up to about 1 Hertz, for example, and is in any case valuable especially in combination with analytic methods. The end effects, however, will play a greater role in the dynamic calculations, thereby increasing the need for three-dimensional computations.

For the Alaskan earthquake, the situation is quite different. The geometry of the fault is such that the resolvability of plane strain models is quite satisfactory. Clearly, more complicated geology and prestress could be introduced, thereby improving the solution's uniqueness. However, we feel that micro-geology would have only a second order influence on the "best fit" solution for the fault offset.

By contrast, a lot of work remains to be done on the Hebgen Lake, Montana, event. Our treatment of it gives only a gross fit to the data, but it serves its purpose in showing a special case of gravitational potential energy being transferred locally into the seismic radiation field. This behavior seems to be a characteristic of normal faulting.

Meister et al. (1968) report that the Fairview Peak, Nevada, earthquakes of 1954 released a minimum strain energy of 1.3 x 10^{23} ergs, while resulting in a net subsidence of the free surface. They estimate the release of gravitational potential energy as 4.3 x 10^{23} ergs. It is interesting to note that for this event Brune and Allen estimate the average stress drop to be 180 bars or seven times more than their estimate for the Alaska earthquake.

Thus, we can conclude that the main difference between thrust faults such as those responsible for the Alaskan and San Fernando earthquakes are characterized by a large prestress level and raise the local gravitational potential energy, while normal faults such as Hebgen Lake and Fairview Peak have a prestress lower than the (apparent) stress drop while showing a net decrease of gravitational potential energy.

The effect of pore pressure on the stress field is shown, in Chapter V of this thesis, to be an extremely important part of the failure mechanism for the Wilmington oil field earthquakes. Clearly our models of the oil field and of the interaction between the withdrawn fluid and the rock matrix were simplified. For instance, we neglected lateral inhomogeneities in the strata and chemical softening or weakening of the rock was ignored. However, some major conclusions can be drawn from our study of the Wilmington subsidence. Without considering the influence of tectonic stresses (which could be added linearly to our results), we showed that the potential for triggering earthquakes by altering the underground fluid-rock condition should be investigated before any large scale waterflooding or withdrawal is allowed to proceed in tectonically unstable areas. We have also shown that further theoretical developments are needed in order to express Biot's interaction constants in terms of geophysical constants measurable in the field. This is necessary if we are to predict the behavior of the medium in response to fluid withdrawal or injection.

Clearly, then, research remains to be done, but we feel that the numerical modeling methods are a powerful and versatile technique, and it is conceivable that in the future this approach will provide the answers to some of the obvious problems that have to be solved in tectonophysics. We have shown that analyses of the local variations of stress drops result in values which compare with stress drops recorded in laboratory experiments. Three-dimensional dynamic models incorporating the most recent rheological studies of materials, plastic behavior, mechanical properties of fault gouge and geological variations with depth should be possible in the near future.

BIBLIOGRAPHY

Alewine, R. W. and T. H. Jordan, Generalized inversion of an earthquake static displacement field, submitted to J. Geophys. Res., 1972.

Allen, D. R., Physical changes in reservoir properties caused by subsidence and repressuring operations, J. Petrol. Tech., 20, 1968.

Allen, D. R., Horizontal movement and subsurface strain due to rebound, Rept. to Dept. Oil Prop., City of Long Beach, Ca., 1971.

Allen, C. R., T. C. Hanks, and J. Whitcomb, San Fernando earthquake: Seismological studies and their implications, Calif. Div. Mines Bull., 1971.

Anderson, D. L., Latest information from seismic observations, in The Earth's Mantle, ed. T. F. Gaskell, 355-420, Academic Press, New York, 1967.

Archambeau, C. B., General theory of elastodynamic source fields, Rev. Geophys., 16, 241-288, 1968.

Archambeau, C. B., The theory of stress waves from explosions in prestressed media, Geophys. J. Roy. Astr. Soc. 28, 1972.

Archambeau, C. B. and C. Sammis, Seismic radiations from explosions in prestressed media and the measurement of tectonic prestress in the earth, Rev. Geophys., 8, 473-499, 1970.

Argyris, J. H., Energy problems and structural analysis, in Aircraft Engineering, 26, 347-356, 383-387, 394, 1954.

Ben Menahem, A., S. J. Singh, and F. Solomon, Deformation of a spherical earth model by internal dislocations, Bull. Seism. Soc. Amer., 59, 813-853, 1969.

Ben Menahem, A. and S. J. Singh, Deformation of a spherical earth by finite dislocations, in Earthquake Displacement Fields and the Rotation of the Earth, ed. L. Mansinha et al., 39-42, 1970.

Ben Menahem, A. and M. Israel, Effects of major seismic events on the rotation of the earth, Geophys. J. Roy. Soc., 19, 367-393, 1970.

Biot, M. A., General theory of three-dimensional consolidation, J. Appl. Phys., 12, 155-164, 1941.

Biot, M. A., Mechanics of deformation and acoustic wave propagation in porous media, J. Appl. Phys., 33, 1482-1498, 1962.

Biot, M. A. and D. G. Willis, The elastic coefficients of the theory of consolidation, J. Appl. Mechanics, 24, 594-601, 1957.

Birch, F., Megageological considerations in rock mechanics, in The State of Stress in the Earth's Crust, ed. W. R. Judd, 1964.

Brune, J., Seismic moment, seismicity and rate of slip along major fault zones, J. Geophys. Res., 73, 777-784, 1968.

Brune, J., Tectonic stresses and the spectra of seismic shear waves from earthquakes, J. Geophys. Res., 75, 4997-5010, 1970.

Brune, J. and C. R. Allen, A low stress drop, low magnitude earthquake with surface faulting: The Imperial Valley, California, of March 4, 1966, Bull. Seism. Soc. Amer., 57, 501-514, 1967.

Brune, J., T. L. Henyey, and R. F. Roy, Heat flow, stress and rate of slip along the San Andreas fault, California, J. Geophys. Res., 74, 3821-3827, 1969.

Burford, R. O., R. Castle, J. Church, N. Kinoshita, S. Kirby, R. Ruthven, and J. Savage, Preliminary measurements of tectonic movements, U. S. Geol. Survey Prop. Paper 733, 1971.

Burridge, R. and L. Knopoff, The effect of initial stress or residual stress on elastic energy calculations, Bull. Seism. Soc. Amer., 56, 1966.

Byerlee, J. D., Frictional characteristics of granite under high confining pressure, J. Geophys. Res., 72, 3639-3648, 1967.

Canitez, N. and N. M. Toksöz, Static and dynamic study of earthquake source mechanism: San Fernando earthquake , J. Geophys. Res., 77, 2583-2594, 1972.

Chinnery, M. A., The deformation of the ground around surface faults, Bull. Seism. Soc. Amer., 51, 355-372, 1961.

Chinnery, M. A., The stress changes that accompany strike slip faulting, Bull. Seism. Soc. Amer., 53, 921-932, 1963.

Chinnery, M. A., Earthquake displacement fields, in Earthquake Displacement Fields and the Rotation of the Earth, ed. L. Mansinha, et al., 17-38, 1970.

Chinnery, M. A., The strength of the earth's crust under horizontal shear stress, J. Geophys. Res., 69, 2085-2089, 1964.

Clark, J. B., Hydraulic process for increasing the productivity of wells, Trans. AIME, 186, 1949.

Clark, G. and R. D. Candle, Failure of rocks under dynamic compressive loading, in The State of Stress in the Earth's Crust, ed. J. W. Judd, 1964.

Courant, R., Variational methods for the solutions of problems of equilibrium and vibrations, Bull. Amer. Math. Soc., 49, 1-23, 1943.

Fraser, G. D., I. Witkind, and N. Willis, A geological interpretation of the epicentral area: The dual basin concept, U. S. Geol. Survey Prof. Paper 435, 99-106, 1964.

Ghaboussi, J. and E. L. Wilson, Flow of compressible fluid in porous elastic media, Rept. UC SESM 71-72, Univ. Calif., Berkeley, 1971.

Gilluly, J. and U. S. Grant, Subsidence in the Long Beach harbor area, California, Bull. Geol. Soc. Amer., 60, 461-530, 1949.

Gurtin, M., Variational principles for linear elastodynamics, Arch. Rat. Mech. and Anal., 16, 34-50.

Gutenberg, B., Travel times of principal P and S phases over small distances in southern California, Bull. Seism. Soc. Amer., 34, 13-32, 1944.

Hales, A. L. and T. Asada, Crustal structures in coastal Alaska, in The Earth Beneath the Continents, Amer. Geophys. Union, Geophys. Mon. 10, 420-432, 1966.

Hamilton, D. H. and R. L. Meehan, Ground rupture in the Baldwin Hills area, Science, 172, 333-344, 1971.

Handin, J. W., in The State of Stress in the Earth's Crust, ed. J. W. Judd, 1964.

Hanks, T. and M. Wyss (1972) The use of body-wave spectra in the determination of seismic source parameters, in press.

Hanks, T., A contribution to the determination and interpretation of seismic source parameters, Ph.D. Thesis, California Institute of Technology, 1972.

Harrison, E., W. F. Kiesnick and W. J. McGuire, The mechanics of fracture induction and extension, Petrol. Trans., AIME, 201, 252-263, 1954.

Haskel, N., Elastic displacements in the near field of a propagating fault, Bull. Seism. Soc. Amer., 59, 865-908, 1969.

Healy, J. H., W. W. Rubey, D. T. Griggs, and C. B. Raleigh, The Denver earthquakes, Science, 161, 1301-1310, 1968.

Hubbert, K. and W. W. Rubey, Role of fluid pressure in mechanics of overthrust faulting, Bull. Geol. Soc. Amer., 10, 115-166, 1959.

Jumikis, A., Soil Mechanics, Van Nostrand, 1962.

Jordan, T. H. and J. N. Franklin, Optimal solutions to a linear inverse problem in geophysics, Proc. Nat. Acad. Sci., 68, 291, 1971.

Jordan, T. H., Ph.D. Thesis, California Institute of Technology, 1972.

Jordan, T. H. and J. B. Minster, Applications of a stochastic inverse to the geophysical inverse problem, in Mathematics of Profile Inversion, ed. L. Colin, Marcell Dekker Inc., New York (in press), 1972.

Judd, W. R., Rock stress, rock mechanics and research, in State of Stress in the Earth's Crust, ed. W. R. Judd, 1964.

Jungels, P. and G. Frazier, Finite element analysis of the residual displacements for an earthquake rupture: Source parameters for the San Fernando earthquake, submitted to J. Geophys. Res., 1972.

Jungels, P. and D. L. Anderson, Strains and tilts associated with the San Fernando earthquake, U. S. Geol. Survey Prof. Paper 733, 1971.

Kamb, B., L. T. Silver, M. Abrams, B. Carter, T. Jordan and B. Minster, Pattern of faulting and nature of fault movement in the San Fernando earthquake, U. S. Geol. Survey Prof. Paper 733, 1971.

Kanamori, H., The Alaska earthquake of 1964: Radiation of long-period surface waves and source mechanism, J. Geophys. Res., 75, 5029-5040, 1970.

Kovach R. L., Archambeau C. B. and Harkrider D. G., Source Mechanism for Wilmington Oil Field, California, Subsidence Earthquakes, in preparation, 1972.

Lee, I. K., Soil Mechanics, Selected Topics, Am-Elsevier, 1968.

Mansinha, L. and D. E. Smylie, The displacement field of inclined faults, Bull. Seism. Soc. Amer., 61, 1433-1440, 1971.

Manyuga, M. M., Geology and development of California's giant Wilmington oil field, in Geology of Giant Petroleum Fields, Am. Assoc. Pet. Geol., Mem. 14, 158-184, 1970.

Maruyama, T., On the force equivalents of dynamical elastic dislocations with reference to earthquake mechanisms, Bull. Earthq. Res. Inst., 41, 467-486, 1963.

Maruyama, T., Statical elastic dislocations in an infinite and semi-infinite medium, Bull. Earthq. Res. Inst., 42, 289-368, 1964.

McGinley, J. R., A comparison of observed permanent tilts and strains with those calculated from displacement dislocations in elastic earth models, Ph.D. Thesis, California Institute of Technology, 1969.

Meister, L. J., R. O. Burford, G. A. Thompson, and R. L. Kovach, Surface strain changes and strain energy released in the Dixie Valley-Fairview Peak, Nevada area, J. Geophys. Res., 73, 5981-5994, 1968.

Mogi, K., Fracture and flow of rocks, in Tectonophysics, 13, 541-568, 1972.

Mogi, K., Study of elastic shocks caused by the fracture of heterogeneous materials and its relation to earthquake phenomena, Bull. Earthq. Res. Inst., 40, 125-173, 1962.

Palmer, D. F., and T. L. Henyey, San Fernando earthquake of 9 February 1971: Pattern of faulting, Science, 172, 712-715, 1971.

Plafker, G., Tectonic deformation associated with the 1964 Alaska earthquake, Science, 148, 1675-1687, 1965.

Plafker, G., The Alaska earthquake of March 27, 1964: Regional effects,

U. S. Geol. Survey Prof. Paper 543-1, 1970.

Plafker, G., The Alaskan and Chilean earthquakes - Implications for Arc tectonics, J. Geophys. Res., 77, 1972.

Press, F. and C. Archambeau, Release of tectonic strain by underground nuclear explosions, J. Geophys. Res., 67, 337-343, 1962.

Press, F., Displacements, strains and tilts at teleseismic distances, J. Geophys. Res., 70, 2395-2412, 1965.

Press, F., Zero frequency seismology, in The Earth's Crust and Upper Mantle, ed. P. J. Hart, 171-173, Am. Geophys. Union, Geophys. Mon. 13, 1969.

Przemieniecki, J. S., Theory of Matrix Structural Analysis, McGraw-Hill, 1969.

Randall, M. J., Stress drop and ratio of seismic energy to moment, J. Geophys. Res., 77, 969-970, 1972.

Riecker, E. R., Report on the Penrose Conference on Fracture Mechanisms and Earthquake Source Mechanisms, in Geotimes, April 1972.

Savage, J. C. and L. M. Hastie, Surface deformation associated with dip slip faulting, J. Geophys. Res., 71, 1966.

Savage, J. C., R. O. Burford, and W. T. Kinoshita, Earth movements from geodetic measurements, in press, 1972.

Savage, J. C. and M. D. Wood, The relation between apparent stress and stress drop, Bull. Seism. Soc. Amer., 61, 1381-1388, 1971.

Schor, G., Seismic refraction studies off the coast of Alaska (1956-1957), Bull. Seism. Soc. Amer., 42, 37-57, 1962.

Scott, R., Principles of Soil Mechanics, Addison-Wesley, 1963.

Singh, S. J. and A. Ben Menahem, Displacements and strain fields due to faulting in a sphere, Phys. Earth Planet. Interiors, 2, 77-87, 1969.

Smith, S. W., and W. van de Lindt, Strain adjustments associated with earthquakes in southern California, Bull. Seism. Soc. Amer., 59 1569-1589, 1969.

Stacey, F. D., in Physics of the Earth, John Wiley and Sons, 1969.

Stauder, W. and G. A. Bollinger, The focal mechanism of the Alaska earthquake of March 28, 1964 and its aftershock sequence, J. Geophys. Res., 71, 5283-5296, 1966.

Steketee, J. A., On Volterra's dislocation in a semi-infinite elastic medium, Can. J. Phys., 36, 192-205, 1958a.

Steketee, J. A., Some geophysical applications of the elastic theory of dislocations, Can J. Phys., 36, 1168-1198, 1958b.

Trifunac, M. D., Stress estimates for the San Fernando, California earthquake of February 9, 1971 main event and thirteen aftershocks, Bull. Seism. Soc. Amer., in press, 1972.

Turner, M. J., R. W. Clough, H. C. Martin, and L. J. Topp, Stiffness and deflection analysis of complex structures, J. Aeronaut. Sci., 23, 805-823, 1956.

U. S. Geological Survey staff, Surface faulting, U. S. Geol. Survey Prof. Paper 733, 1971.

Wantland, D., Geophysical measurements of rock properties in situ, in The State of Stress in the Earth's Crust, W. Judd ed., 1964.

Wentworth, C. and R. Yerkes, Geological setting and larger aftershocks of the San Fernando area, California, U. S. Geol. Survey Prof. Paper 733, 1971.

Whitcomb, J., Fault plane solution of the February 9, 1971 San Fernando earthquake and some aftershocks, U. S. Geol. Survey Prof. Paper 733, 1971.

Whitcomb, J., C. R. Allen, J. D. Garmany and J. A. Hileman, The 1971 San Fernando earthquake series, focal mechanisms and tectonics, in preparation, 1972.

Wood, H. O. and C. Richter, A second study of blasting in southern California, Bull. Seism. Soc. Amer., 23, 1933.

Wyss, M. and T. C. Hanks, The source parameters of the San Fernando earthquake inferred from teleseismic body waves, in press, 1972.

Wyss, M. and P. Molnar, Efficiency, stress drop, apparent stress and frictional stress of Denver, Colorado earthquakes, J. Geophys. Res., 77, 1433-1439, 1972.

Wyss, M. and J. Brune, The Alaska earthquake of March 28, 1964 - A complex multiple rupture, Bull. Seism. Soc. Amer., 57, 1017-1023, 1967.

Yamakawa, N., Stress fields in focal regions, J. Phys. Earth, 19, 1971.

Zienkiewicz, O. C. and Y. K. Cheung, *The Finite Element Method in Structural and Continuum Mechanics,* McGraw-Hill, New York, 1967.

Zienkiewicz, O. C. and Y. K. Cheung, *The Finite Element Method in Structural and Continuum Mechanics,* McGraw-Hill, New York, 1972, 2nd ed.